Lukas Konrad, MSc

# A consistent path for phase determination based on transmission electron microscopy techniques and supporting simulations

**DOCTORAL THESIS**

to achieve the university degree of

Doktor der technischen Wissenschaften

submitted to

**Graz University of Technology**

**Supervisor**

Ao.Univ.-Prof. Dipl.-Ing. Dr.techn., Gerald Kothleitner

Institute of Electron Microscopy and Nanoanalysis (FELMI)
Graz Centre for Electron Microscopy (ZFE)

Graz, August 2020

# AFFIDAVIT

I declare that I have authored this thesis independently, that I have not used other than the declared sources/resources, and that I have explicitly indicated all material which has been quoted either literally or by content from the sources used. The text document uploaded to TUGRAZonline is identical to the present doctoral thesis.

Date, Signature

It is the invisible essence
that gleams the most
in the visible world.
*(Guido Brivio di Bestagno)*

# Abstract

This thesis is devoted to aspects of the analysis of industrially relevant materials via transmission electron microscopy (TEM).

There is a strong interest to determine the phases formed within the sintered bulk material or on the sintered bulk material in the manufacturing process of hard metals and ceramics used as tooling materials. Analysis of these, frequently sub-stoichiometric, phases requires several characterization techniques to be employed simultaneously to yield a complete and consistent picture.

Therefore, a continuous path, linking the structural characterization of hard metal industrial samples with multimodal analytical electron microscopy (AEM), including quantitative electron energy-loss (EEL) along with energy-loss fine-structure simulations and energy-dispersive X-ray (EDX) spectroscopy, is described.

In a first step, atomistic hydrogenic cross sections, which lack EELS fine-structure details (ELNES), were compared with cross sections obtained from ab initio multiple scattering calculations, as implemented in the FEFF9 code. With this tool EEL spectra (and energy differential cross sections) can be calculated based on Green's functions theory when fed with crystal structure data. Furthermore, hydrogenic calculations have been adjusted to better match the simulated data by tuning the inner-shell screening constant (s) for non-hydrogen-like atoms.

In a second step, the phases and their crystallographic structure were confirmed by carrying out cross section simulations, either performed with structural data files generated by nano electron diffraction tomography (NEDT) or taken from databases via the EELS-ELNES region. Further certainty on the phases' structure was gained by selected area electron diffraction (SAED) and HR-imaging and supported by computer simulations.

In a third step a well characterized $Ti_3SiC_2$ MAX phase has been used as a demonstrator to show consistent results of EELS and EDX zeta-factor measurements. Moreover, the stoichiometry of a Ti(C,N) phase has been addressed on the basis of accurate inner-shell ionization cross sections.

# Kurzfassung

Diese Arbeit befasst sich mit Aspekten der Analyse von industrie-relevanten Proben mittels Transmissionselektronenmikroskopie (TEM).

Bei der Herstellung von Hartmetallen und Keramiken in der Werkzeugindustrie besteht ein großes Interesse daran, die innerhalb des gesinterten Substrats oder dessen Beschichtung gebildeten Phasen zu bestimmen. Die Analyse dieser häufig unterstöchiometrischen Phasen erfordert die gleichzeitige Anwendung mehrerer Charakterisierungstechniken, um ein vollständiges und konsistentes Bild zu erhalten.

Daher wird ein kontinuierlicher Pfad beschrieben, der die strukturelle Charakterisierung von industriellen Hartmetallproben mit multimodaler analytischer Elektronenmikroskopie (AEM), d.h. quantitativer Elektronenenergieverlust (EEL) Spektroskopie gepaart mit Energieverlust-Feinstruktursimulationen und energiedispersiver Röntgenspektroskopie (EDXS) verbindet.

In einem ersten Schritt wurden atomistische EELS-Wasserstoff-Streuquerschnitte mit Streuquerschnitten verglichen, die aus ab-initio-Mehrfachstreuungsberechnungen mittels FEFF9-Code simuliert wurden. Mit diesem Programm können EEL-Spektren (und energiedifferentielle Streuquerschnitte) basierend auf der Greenschen Funktionstheorie ausgehend von Kristallstrukturdaten berechnet werden. Weiters wurden die Wasserstoff-Streuquerschnitte mit den simulierten Daten über die Abschirmkonstante (s) für nicht wasserstoffähnliche Atome angepasst.

In einem zweiten Schritt wurden die Phasen und ihre kristallographische Struktur durch Streuquerschnittssimulationen bestätigt. Die kristallografischen Daten zur EELS-Feinstruktur Simulation kamen entweder aus Nano-Elektronenbeugungs-Tomographie (NEDT) Strukturdatendaten oder aus Datenbanken. Weitere Gewissheit über die Phasenstruktur wurde durch Feinbereichsbeugung (SAED) und HR-imaging gewonnen und durch Computersimulationen unterstützt.

In einem dritten Schritt wurde eine gut charakterisierte $Ti_3SiC_2$ MAX-Phase ausgewählt, um konsistente Ergebnisse von EELS- und EDX-Zeta-Faktor-Messungen zu zeigen. Darüber hinaus wurde die Stöchiometrie einer Ti(C,N)-Phase auf der Grundlage genauer Innenschalen-Ionisationsquerschnitte untersucht.

# Acknowledgements

The present work would not have been possible without the help of many people for which I want to express my deepest gratitude at this point.

First of all, I want to thank my supervisor Gerald Kothleitner for his guidance and, most importantly, the patience to supervise my studies, as well as Ferdinand Hofer, the head of the institute, and all other FELMI-ZFE members for providing a pleasant working environment.

Moreover, I would like to thank Martina Dienstleder, Sebastian Rauch and Manuel Paller for TEM sample preparation, Christian Gspan for helping me with electron diffraction experiments and Stefan Mitsche for performing XRD measurements. Johanna Kraxner and Judith Lammer, I thank for their help and fruitful discussions concerning ζ–factor measurements.

I want to express my special gratitude to Martina Lattemann and Ernesto Colonel from AB Sandvik Coromant, Sweden, not only for sample provision, guidance and fruitful discussions, but also for their warm welcome to Stockholm.

I want to thank Ute Kolb and Haishuang Zhao from the Johannes Gutenberg University in Mainz for introducing me to the world of nano electron diffraction tomography.

Paul Thomas from Gatan Inc. is gratefully acknowledged for his help with DigitalMicrograph EELS quantification routines.

John Rehr, Micah Prange and Kevin Jorisson from the University of Washington are thanked for their support with the FEFF9 code.

Last, but not least, I want to thank my mother and aunt for their ever-lasting love and patience, my father for inspiring me to explore the great field of natural sciences and all of my friends, who have always been a huge support for me.

Finally, I want to acknowledge the financial support by AB Sandvik Coromant, Sweden.

# Contents

Abstract ..... i

Kurzfassung ..... ii

Acknowledgements ..... iii

Contents ..... iv

1 Introduction ..... 1

1.1 Motivation ..... 1

1.2 Historical Background ..... 3

1.3 Tungsten: Occurrence – Discovery – Invention of Hard Metals ..... 4

2 Materials ..... 8

2.1 Carbides – with Focus on Tungsten Carbide ..... 8

2.1.1 Structure of nonstoichiometric carbides ..... 9

2.1.2 The W-C phase diagram ..... 10

2.2 Binary and ternary metallic hard materials ..... 11

2.2.1 Structure of titanium carbonitride – Ti(C,N) ..... 12

2.3 MAX Phases ..... 13

2.3.1 Crystal structure ..... 13

3 Experimental techniques ..... 15

3.1 Utilized Instrumentation ..... 15

3.1.1 Sample preparation ..... 16

3.2 Transmission Electron Microscopy ..... 17

3.2.1 General Setup ..... 17

3.2.2 Electron beam monochromation ..... 20

3.2.3 EELS imaging and spectroscopy ..... 21

3.2.4 Multi-slice image simulations ..... 22

3.3 Electron Diffraction ..... 23

3.3.1 Selected area electron diffraction (SAED) ..... 24

3.3.2 Convergent beam electron diffraction (CBED) ..... 25

3.3.3 Nano Electron Diffraction Tomography (NEDT) ..... 27

3.3.4 Diffraction pattern treatment ..... 31

3.3.4.1 Creating a *.cif file from ADT data ................................................ 33
3.4 Electron Energy-loss Spectroscopy (EELS) ................................................ 36
3.4.1 The EEL spectrum ................................................ 37
3.4.2 EELS Quantification ................................................ 38
3.4.2.1 Conventional approach ................................................ 39
3.4.2.2 “Model based” approaches ................................................ 44
3.4.2.3 EELS Intensity extraction model based approach ................................................ 45
3.4.2.4 Comparison of intensity extraction using 2 different approaches ..... 47
3.4.3 Theory behind EELS cross sections ................................................ 48
3.4.3.1 Atomistic calculations ................................................ 49
The Hydrogenic Approximation ................................................ 49
The Hartree-Slater model ................................................ 50
3.4.3.2 Experimental EELS cross sections ................................................ 51
3.4.3.3 Cross section simulations by multiple scattering theory ................................................ 52
3.4.3.3.1 Performing ELNES simulations based on a *.cif file ................................................ 54
3.4.3.4 Summary ................................................ 57
3.5 Energy Dispersive X-ray Spectroscopy (EDXS) ................................................ 57
3.5.1 Quantitative EDX analysis ................................................ 58
3.5.1.1 The k-factor method ................................................ 59
3.5.1.2 The zeta factor method ................................................ 60
3.5.1.3 Acquisition and analysis of ζ-factors step by step. ................................................ 61
3.5.1.3.1 Thickness measurements – sample preparation ................................................ 61
3.5.1.3.2 ζ-factor acquisition ................................................ 62
3.5.1.3.3 Intensity determination ................................................ 63
3.5.1.3.4 Kramers’ model background subtraction ................................................ 63
3.5.1.3.5 Top-hat filter background subtraction ................................................ 64
3.5.1.3.6 Which method to choose? ................................................ 64
4 Results on simulations and analysis ................................................ 67
4.1 Comparison of FEFF cross sections with the hydrogenic approximation ...... 67
4.1.1 Appropriate screening factors for the hydrogenic approximation ................................................ 72
4.2 Data analysis ................................................ 75
4.2.1 ADT experiments on tungsten carbide ................................................ 76
4.2.2 FEFF simulation on WC ................................................ 78

4.2.3 Titanium silicon carbide ........ 80
4.2.3.1 SAED investigation ........ 80
4.2.3.2 HR-imaging ........ 81
4.2.3.3 Quantification ........ 82
4.2.4 Titanium carbonitride ........ 87
4.2.4.1 XRD on Ti(C,N) ........ 87
4.2.4.2 TEM imaging on Ti(C,N) ........ 88
4.2.4.3 SAED and CBED investigations on Ti(C,N) ........ 90
4.2.4.4 ADT experiment on Ti(C,N) ........ 92
4.2.4.5 ELNES measurements on Ti(C,N) ........ 93
4.2.4.6 EELS quantification on Ti(C,N) ........ 96
4.3 Reference Spectra ........ 98
5 Conclusions ........ 99
Bibliography ........ 101

# 1 Introduction

## 1.1 Motivation

The aim of this thesis is to employ several characterization techniques simultaneously to properly identify and quantify important phases used in the hard metal industry. It is essential for the industry to know which reaction mechanisms are going on in order to improve their products. This goal is very challenging, as precipitates are often in the nanometer range. Thus, the instrument of choice is the transmission electron microscope (TEM), which offers possibilities for structural as well as compositional analysis. Not only the small size, but also the often nonstoichiometric nature of these compounds (e.g. nonstoichiometric carbides (Gusev et al., 2001) or crystals with sites of partial occupancy, e.g. Ti(C,N) (Angseryd et al., 2011)) combined with a lack of commercially available reference materials necessitates an approach that describes a continuous path that successfully characterizes these materials (Fig. 46) with different available TEM techniques that, yield a complete and consistent picture.

The combination of different TEM techniques is highly recommended, as single techniques often do not achieve the desired results. For example: EELS quantification without proper reference spectra relies on calculated cross sections, which can be seen as a rough estimate to reality, lacking fine-structure details. Reference spectra, however, rely on well-characterized samples whose crystal structure can be determined by electron diffraction techniques, which lack elemental composition.

The second chapter focuses on the choice of materials to be characterized within this thesis and is based on the relevance for the hard metal industry. It provides a glimpse of the stoichiometric variety of those phases. Starting out with the leading material in the industry, tungsten carbide, the complexity of an unambiguous characterization becomes obvious as different structural phases are stable only within certain temperature and concentration ranges. Further, binary and ternary carbides and nitrides of the transition metals, that have been used as coatings in cutting applications for a long time, will be explained. Interest has shifted over the past decades toward titanium carbonitrides $TiC_xN_{1-x}$, for their increased abrasive wear (Peng et al., 2013). The introduction of extra nitrogen between $x = 0$ and 1 broadened the spectrum of tunable properties even more, thus creating an increased need in the characterization of light element material systems. Another class are layered refractory ternary carbides and nitrides, consisting of a

transition metal, an A group element as well as carbon and/or nitrogen termed MAX phases (Barsoum, 2000), is also discussed. This material class will be used as a demonstrator because its structure is well known, although not used as coating in the tooling industry.

The experimental techniques used are described in chapter 3. Starting with a brief introduction on the physical principles, close attention is drawn to structural and elemental analysis.

Structural wise, an unknown material can be characterized by HR-imaging or employing electron diffraction (ED) techniques. A very accurate technique is to perform nano electron diffraction tomography experiments (NED) - more precisely automated nano electron diffraction tomography (ADT) combined with electron precession (PED), (Kolb et al., 2008, 2007). The analysis of this dataset leads to a set of hkl-values that can be further processed to create a crystallographic information (*.cif) file, which can be further used for simulations.

The section on elemental analysis is devoted to EELS and EDX. Concerning EELS, signal extraction techniques, in connection with a proper background subtraction, as well as the achievement of appropriate cross sections, that are needed to turn intensities into concentrations, are described. While cross sections calculated from analytical models derived from hydrogenic approximations (SIGMAK, SIGMAL) or from Hartree Slater oscillator strengths (Egerton, 2011) turn out to be questionable and experimental cross sections rely on well-defined samples of known thickness and composition, an alternative by the means of simulation was used. This new approach shows how to get these scaling factors out from ab initio multiple scattering EELS simulations, as implemented in the FEFF 9 code (Moreno et al., 2007; Rehr et al., 2010). With this tool electron energy-loss near edge structure (ELNES) and EEL spectra (and energy differential cross sections $\sigma$) can be calculated based on Green's functions theory, when fed with a crystallographic structure (*.cif) file that is either generated from ADT experiments or searched in databases. The end of the chapter deals with EDX analysis. The conventional k-factor approach (Cliff and Lorimer, 1975) for relative quantification of elements in contrast to the $\zeta$-factor approach (Watanabe & Williams, 2006) for gaining concentrations of single elements will be explained, topped off with the question of appropriate signal extraction.

In chapter 4 the results are presented. The first part is devoted to the one hand on cross section simulation via the FEFF code, on the other hand to improvements of the hydrogenic approach for cross section calculation. The second part presents the analyzed

materials showing the synergy between the outcome of structural determination along with quantitative results on the accurate treatment of references. Therefore, the tungsten carbide system acts as a demonstrator to link crystallographic data obtained from electron diffraction (tomography) to electron energy-loss fine-structures. Subsequently, we carry on to study a $Ti_3SiC_2$ MAX phase. This phase, properly characterized structurally, acts as a reference to discuss the effect of EELS cross sections as well as the role of essential parameters such as screening factors. Further, a comparison of the EELS compositional analysis results on the basis of better adapted cross sections with EDX measurements will be made. The composition of an unknown titanium carbonitride coating on a WC substrate, hardly accessible via electron diffraction techniques, can finally be addressed, considering adequate inner-shell ionization cross sections.
A consistent set of cross sections can lead to more reliable data and serve as a reference in databases for subsequent analysis. Therefore, the database Spectra Viewer is portrayed at the end of the chapter.

## 1.2 Historical Background

In the 1890s Henry Moissan's primary intention was to synthetize diamond in an electric arc furnace. Instead of the desired diamond some of the components found were tungsten carbide (WC) (Lassner and Schubert, 1999) – the basis for hard materials.
The real era of hard metals started nearly hundred years ago. The Schröter patent (1923) can be seen as the cornerstone of this development. By using WC based hard metals as nozzle tips of extruders for drawing tungsten filaments for incandescent light bulbs, the costly diamond, that has a high melting point, high hardness and wear resistance, could finally be replaced (Kieffer et al., 1953; Lassner and Schubert, 1999).
In the past, superalloys and hardened steels were only shaped by grinding. The newly developed hard metal tools, however, can be used for the turning of these materials, which by far is more time and cost efficient.
Nowadays hard materials (minimum hardness of HV=1000; Berg et al., 2000; Schedler, 1988), either WC based hard metals, or cermets (combining the properties of ceramics with those of metals) with and without coating, represent the backbones of the tooling industry, combining toughness, hardness, mechanical strength and a high melting point.

They- among other usages- are used for mining applications, drawing dies, metal and stone cutting, rolls for hot rolling and cold forming tools.

Fig. 1 illustrates the variety of cutting tool material classes considering their wear resistance with respect to toughness. The hardest of them is poly crystalline diamond (PCD) followed by cubic boron nitride (CBN), ceramics and hard metals (HM). As hard metals cover a wide hardness/toughness range it is the most important hard material for the industry.

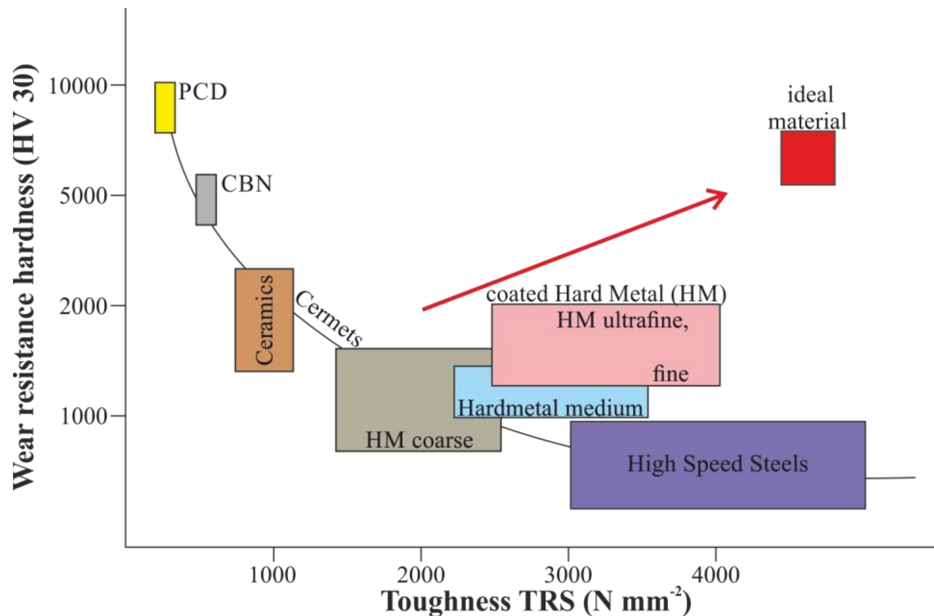


**Fig. 1** Schematic wear resistance-toughness relationship for cutting tool material classes. Redrawn from Prakash (2014).

Considering the growing demand on tailored solutions for individual applications, there is also a need for comprehensive and unambiguous characterization of these newly developed products, which gives a broader insight into reactions of the sintered bulk material or the hard coating.

## 1.3 Tungsten: Occurrence – Discovery – Invention of Hard Metals

The most important element for the production of hard metals is tungsten. Tungsten is found in pegmatitic or hydrothermally formed ores, in the form of wolframite ($(Fe,Mn)WO_4$) – indicating low Ca-concentrations of the host rock – and scheelite ($CaWO_4$) indicating a Ca- rich host rock, e.g. limestone (Skarn formation) (Best, 2003).

Already during the Middle Ages, tungsten minerals were known in the tin mines of the Saxonian Erzgebirge (SE part of East-Germany), the Bohemian Krušné hory (Northern Czech Republic) and the Cornubian orefield (SW of England), all associated with late Variscian magmatic events (Pitfield et al., 2011; Seifert, 2008). However,

tungsten's negative influence during the tin production (Lassner and Schubert, 1999), miners recognized it as waste material often occurring in paragenesis with the desired cassiterite ($SnO_2$), which is why solid tungsten was discovered much later.

In the 16$^{th}$ century, Agricola mentioned tungsten, in his *De Natura Fossilium*, as "spuma lupi", which translated from Latin means "wolf's foam" in English and "Wolfsschaum" in German. The reason for this name is that the presence of tungstate minerals during tin melting causes a foam, which retards a certain amount of tin, thus decreasing the yield (Gmelins Handbuch der Anorganischen Chemie, 1933).

The mineral scheelite was first mentioned 1757 by the Swedish mineralogist Alex Fredric Cronstedt. Due to its high density (6 g cm$^{-3}$), he named it tungsten, derived from the Swedish "tung sten", meaning "heavy stone", and defined it as a calcium-containing iron mineral. In 1781, Carl Wilhelm Scheele analyzed tungsten (scheelite ore) and concluded, that it was a calcium salt of an unknownn acid. In 1783 Don Juan Jose de Elhuyar together with his brother produced metallic tungsten by the reduction of tungstic acid with powdered charcoal and named it Wolfram. The German word Wolfram, which is the translation of the English word tungsten is deduced from the German words "Wolf" (engl.: wolf) and "Rahm" = Geifer (engl.: spittle) derived from on the 18$^{th}$ century idea that the wolf eats the tin. To this day Wolfram is the name for tungsten in German and Swedish. In honour of Carl Wilhelm Scheele, Karl Cäsar von Leonhard suggested in 1821 the name Scheelite for the mineral $CaWO_4$.

Robert Oxland patented a method for producing sodium tungstate, tungsten oxide, and metallic tungsten setting the stage for modern tungsten chemistry in 1874. He was also the first proposing a method for the production of ferrotungsten, yet not to be used as an alloying element to increase the hardness of steel, due to its high price. (Lassner and Schubert, 1999).

In 1900, the Bethlehem Steel Company presented the first high-speed and temperature steel cutting tools at the Paris Exhibition.

William David Coolidge (1913) described the production of ductile tungsten wire by powder metallurgy in his patent. This caused the first industrial application of powder metallurgy. Researchers of Franz Skaupy's working group at "Osram study group for electrical lighting" in Germany combined WC with a ductile matrix to make cemented carbides in the early 1920s. This lead to the famous patent of Karl Schröter, DRP (Deutsches Reichspatent) 420,689 (WC+10 % Fe, Ni, or Co) followed by DRP 434,527 (WC up to 20% Co). Unaware of the significance of the invention, the patent has only

been applied in England and the USA and sold to the Krupp Company in 1925. Krupp introduced the first hard metal cutting tool at the Leipzig fair in 1927 under the trademark WIDIA derived from the German words “wie” and “Diamant” meaning “like a diamond” that still is used (Ettmayer et al., 2014; Fang et al., 2014; Kieffer et al., 1953; Lassner and Schubert, 1999).

Nowadays, the range of products from WC based hard metals, synonymously called cemented carbides (mainly found in English literature), is quite broad. There is also a strong strategical and economical interest that WC gets at least partially replaced by other refractory nitrides, carbides or carbonitrides of transition metals. This class of products is often called cermets, which combine the properties of ceramics (such as hardness and wear resistence) with those of metals (Prakash, 2014) starting with patents (1929-1937) from the working group of Paul Schwatzkopf, Founder of Metallwerke Plansee (Kieffer et al., 1953).

In 1931 within ÖP (Österreichisches Patent) 160172 Paul Schwartzkopf and Isidor Hirschl proposed a WC-free hardmetal consisting of $Mo_2C$-TiC-Ni (42.5% $Mo_2C$, 42.5% ZiC, 14/ Ni, 1% Cr) leading to the first cermet sold under the Name “Titanit” by the Deutsche Edelstahlwerke A.G. Krefeld in Germany and “Cutanit” in the USA and England (Kieffer et al., 1953).

Hard coatings were introduced for maximizing surface hardness, in order to optimize wear resistance, without sacrificing the toughness of the bulk component and risking brittle fracture. This leads to good adhesion to the bulk while minimizing residual stress in the coating (Chatterjee and Chandrashekhar, 1996; Sherman and Brandon, 2000). These hard coatings have been produced via condensation from the vapor phase (Schleinkofer et al., 2014) since the 1960s and represent the most significant development. Today, more than 80% of all turning inserts and about 70% of milling inserts are coated (Lassner and Schubert, 1999). Two main coating procedures are employed: chemical vapor deposition (CVD) and physical vapor deposition (PVD). The CVD’s vapor precursor is gaseous, while it is produced from a solid source in PVD. As the CVD process works at elevated temperatures, these coatings are restricted to cemented carbides, whereas PVD coatings are performed at lower temperatures. Thus, also metallic substrates can be used. A relatively thick coating can be applied on complex substrate geometries by applying the CVD method, e.g. TiCN and recently AlTiN, while PVD permits the deposition of metastable coatings, due to ionizing of the reactants as well as the low deposition temperatures (Schleinkofer et al., 2014).

Commercial applications of cemented carbides are manifold and are summed up by Williams (2012) concerning global turnover and global consumption:

**Table 1** Market share of hardmetal products by application. (Williams, 2012)

| Worldwide application area | Worldwide turnover (%) | Worldwide consumption by weight (%) |
|---|---|---|
| Metal cutting | 65 | 22 |
| Wood and plastics | 10 | 26 |
| Wear applications[1] | 10 | 17 |
| Stone working | 10 | 26 |
| Chipless forming | 5 | 9 |

[1)] The definitions of application areas for wear parts are not well defined; sometimes products in chipless forming, stone working as well as in wood and plastics are partially clubbed together as wear parts.

A promising relatively new range of materials for the industry are the so called “cermets” that combine properties of metals with those of ceramics. Although already discovered in the 1960s, these materials only gained a broader interest in the late 1990s where (Barsoum, 2000) introduced the term MAX phases for these layered ternary compounds. Above all, the $Ti_3SiC_2$ MAX-phase is the most studied of all phases. Recently pressureless sintering and PVD coatings as well as MAX based composites have been developed (Sun, 2011), ranging from heating elements, gas burner nozzles to concrete dry drills waiting for future applications.

# 2 Materials

## 2.1 Carbides – with Focus on Tungsten Carbide

Tungsten carbides (WC) are known for their thermal stability at temperatures of 700 to 900 °C, which predestines them for producing wear resistant hard metals, as the decrease in the stability of the WC's hardness goes along slightly with a temperature increase from ~ 27 to 1000 °C (Kurlov and Gusev, 2013). Further, Kurlov and Gusev (2013) outline that using WCs directly is impossible due to the brittleness, but and can be overcome by using cobalt as a binder material.

WC's melting point at about 2800 C° and its hardness is low when compared with other carbides of transition metals (Fig. 2), further the Young's modulus of WC is nearly twice as large while the thermal expansion coefficient is lower in the C-direction of hexagonal WC (Fig. 2) (Kurlov and Gusev, 2013, Exner, 1979)

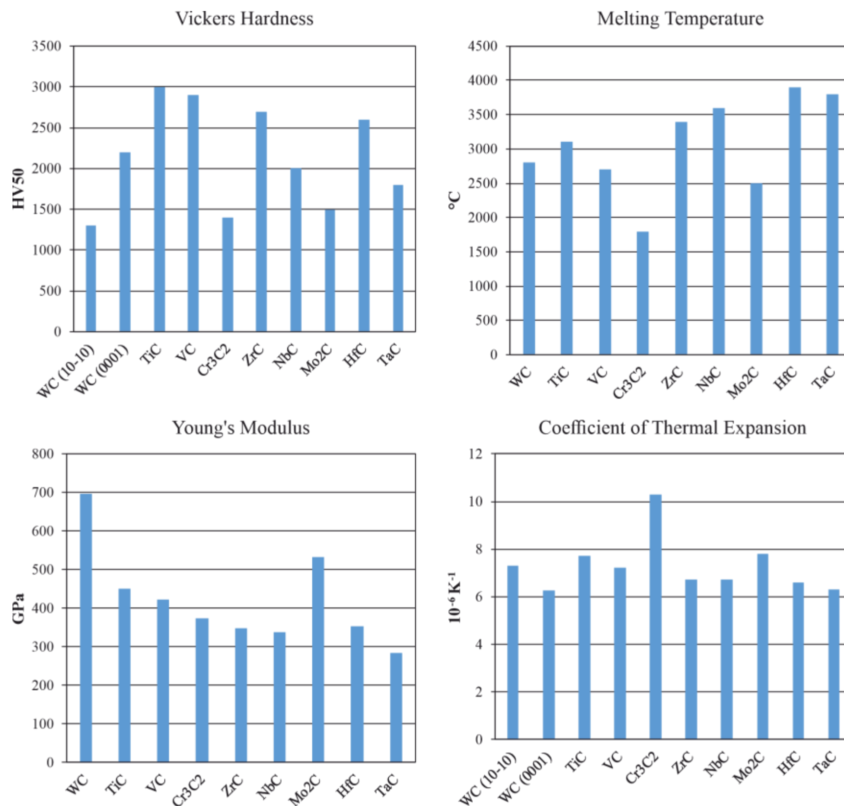


**Fig. 2** Properties of WC compared to other carbides according to Exner (1979)

### 2.1.1 Structure of nonstoichiometric carbides

Carbides of period 4 to 5 transition metals can be seen as interstitially nonstoichiometric crystals (Gusev, Rempel, Magerl, 2001). The term nonstoichiometric refers to compounds with homogeneity regions having at least a minimal vacancy concentrations capable of securing the vacancy - vacancy interaction (Rempel, 1996).
The carbon atoms are located at the central position of trigonal-prismatic interstices in the tungsten sublattice and form a nonmetallic sublattice (Kurlov and Gusev, 2006).
The structural vacancies concentration in the nonmetal sublattice determines the non-stoichiometry of the carbide (i.e., the deviation from the stoichiometry $MC_{1.00}$ or $M_2C_{1.00}$) and may be as high as 30 to 60 at. % at the lower homogeneity bound (Rempel, 1996).
The crystal structure is characterized by the presence of the face-centered cubic (fcc) (Fig. 3(a)) or hexagonal (simple or closely-packed (hcp)) (Fig. 3(b)) metallic lattice.

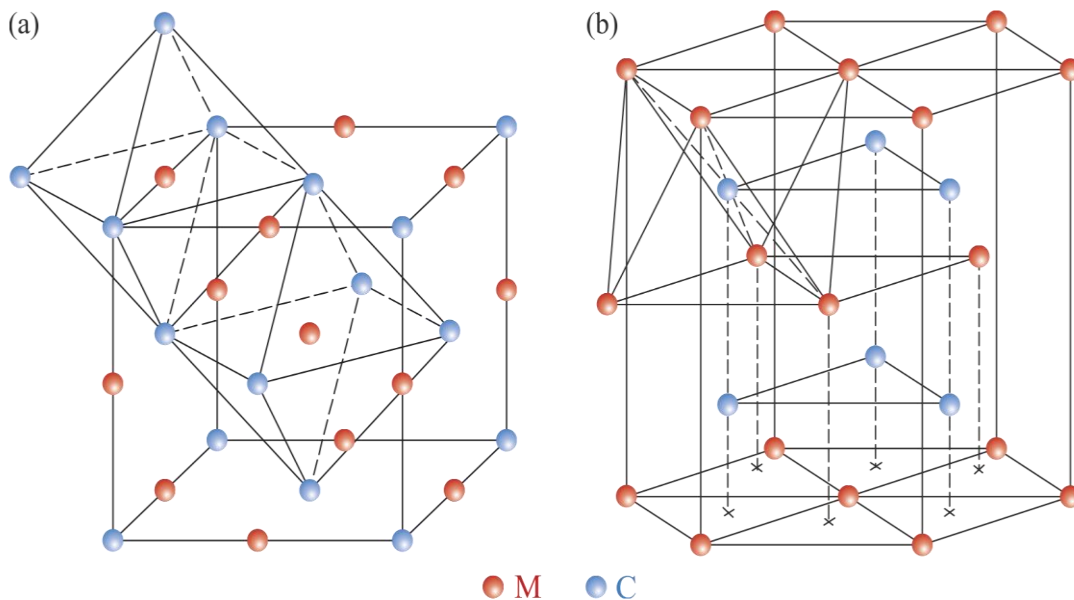


**Fig. 3** (a) $MC_y$ unit cell with NaCl cubic structure. red: metal atoms, blue: nonmetallic sublattice sites occupied statistically (with y probability) by e.g. carbon. Neighboring octahedra built of the nonmetallic sublattice surrounding the metal atom are drawn. Redrawn from Kurlov and Gusev (2013).
(b) General view of the crystal lattice of a L'3 hexagonal (space group P63/mmc) compound $M_2C$. red: metal atoms, blue: nonmetallic sublattice sites. A hcp metallic sublattice is formed while the octahedral interstitials are filled with C atoms randomly. Redrawn from Kurlov and Gusev (2006).

As carbides are formed, the metals' crystal structure is changed, therefore, on the one hand, strong metal-carbon interactions are suggested as the transition metallic lattice symmetry differs from the metallic sublattice symmetry, on the other hand, direct carbon-carbon interactions are small (Kurlov and Gusev, 2013). While the transition metals Ti, Zr, Hf show a hcp structure, and V, Nb, Ta show a body centered cubic (bcc) structure, their carbides have a fcc structure ($MC_y$) with carbon in the B1-type (NaCl) structure (Fig.

3(a)). Transition metals with the bcc structure, Cr, Mo, W, form either carbides with cubic (Fig. 3(a)) or hexagonal ($M_2C_y$) structure (Fig. 3(b)) with the L'3 ($W_2C$) metallic sublattices (Gusev et al., 2001; Kurlov and Gusev, 2013; Lengauer, 2000; Rempel, 1996).

### 2.1.2 The W-C phase diagram

Besides elemental tungsten and carbon, the W-C system comprises two phases, $W_2C$ and WC, with several structural modifications that are stable within certain temperature and concentration ranges (Kurlov and Gusev, 2006) (Fig. 4).
The nomenclature however throughout literature comprises the Greek alphabet from α to δ and is used without consistency. Therefore the nomenclature of Kurlov and Gusev (2006) is used:

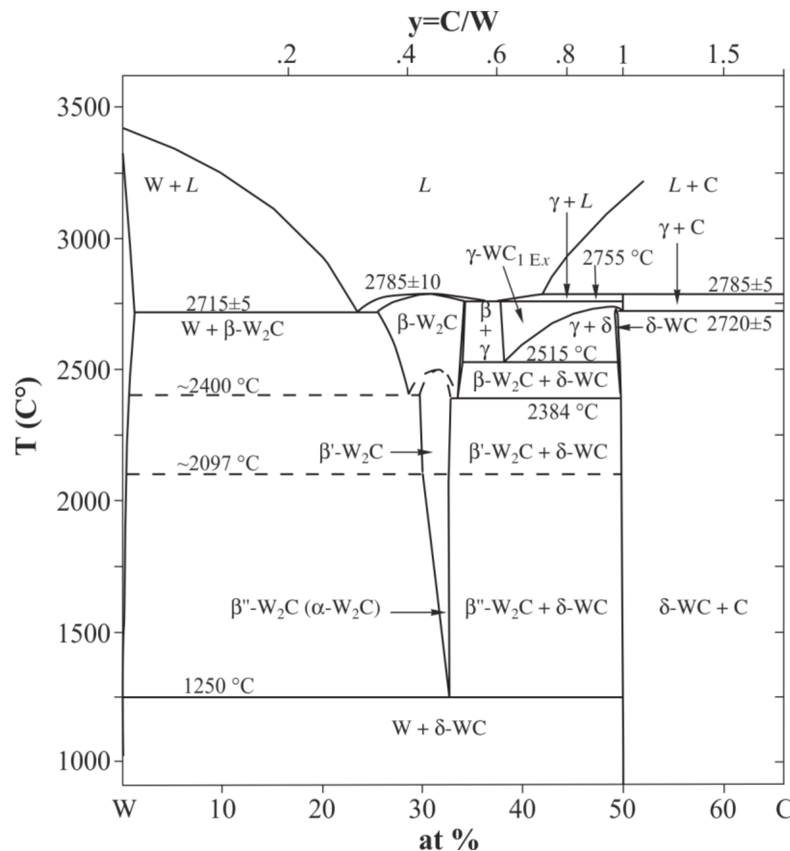


**Fig. 4** Phase diagram of the W-C system. Redrawn from Kurlov and Gusev (2006).

Tungsten carbide, WC, the major phase in the W-C system, with the hexagonal structure is designated as δ-WC. The cubic phase $WC_{1-x}$ designated as γ-$WC_{1-x}$ and is, according to Goldschmidt and Brand (1963), advised to be a structural modification of the hexagonal WC.
$W_2C$ exhibits 3 well characterized modifications among all those, a metallic hcp (hexagonal closest packed) sublattice is formed by W-atoms, while 0.5 of the octahedral

interstitials are filled with C-atoms (Fig. 5), thus showing ordering and disordering at low and high temperatures respectively depending on the C-atom distribution.

The distribution type of C-atoms is the cause that several structural modifications of $W_2C$, deduced β, β' and β''-$W_2C$ for the high and low temperature modification respectively, are formed (Kurlov and Gusev, 2006) (Fig. 4).

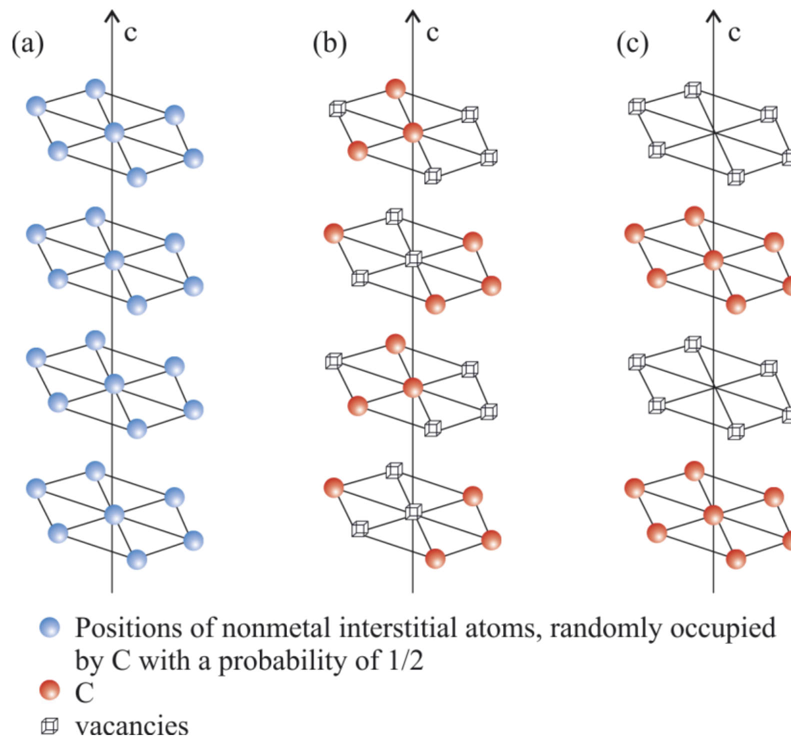


**Fig. 5** Distribution of C-atoms in $W_2C$. Planes of the nonmetallic sublattice sites are orthogonally arranged with respect to the c axis; W-atoms are not displayed: (a) β-$W_2C$ of the L'3 structure type where C atoms and vacancies are randomly distributed. (b) β'-$W_2C$ of the ζ-$Fe_2N$ structure type where C-atoms and vacancies are evenly distributed along the c-axis in each plane of the nonmetallic sublattice. (c) β''-$W_2C$ of the C6-type structure where of C-atom layers alternate regularly with vacancy layers. Redrawn from Kurlov and Gusev (2006).

## 2.2 Binary and ternary metallic hard materials

Binary carbides and nitrides of the transition metals form solid solutions. They exhibit, in most cases, extreme properties for ternary compositions (Holleck, 1986). While carbides (e.g. WC, TiC, TaC…) were used since the 1930s as components in cemented carbides with a cobalt binder, the time has not yet come for transition metal nitrides as the sintering process is more complex than for the carbides. The breakthrough of vacuum coating technology in the 1960s has set the stage for the nitrides as thin coatings on hard metals (Lassner and Schubert, 1999). In the early days, the only commercially used wear resistant coating was TiN, however, during the past decades a large interest has turned to

$TiC_xN_{1-x}$ (Karlsson et al., 2000). The ternary $TiC_xN_{1-x}$ has the advantage over the binary TiN with respect to higher flank wear resistance (abrasive wear) resulting in an increased coating hardness (Randhawa, 1987).

### 2.2.1 Structure of titanium carbonitride – Ti(C,N)

According to Levi et al. (1998) Ti(C,N) can form two different structure types: face centered cubic (FCC) belonging to the Fm-3m space group or tetragonal, belonging equally to the P4/m, P422, P-42m or P4/mmm space groups.

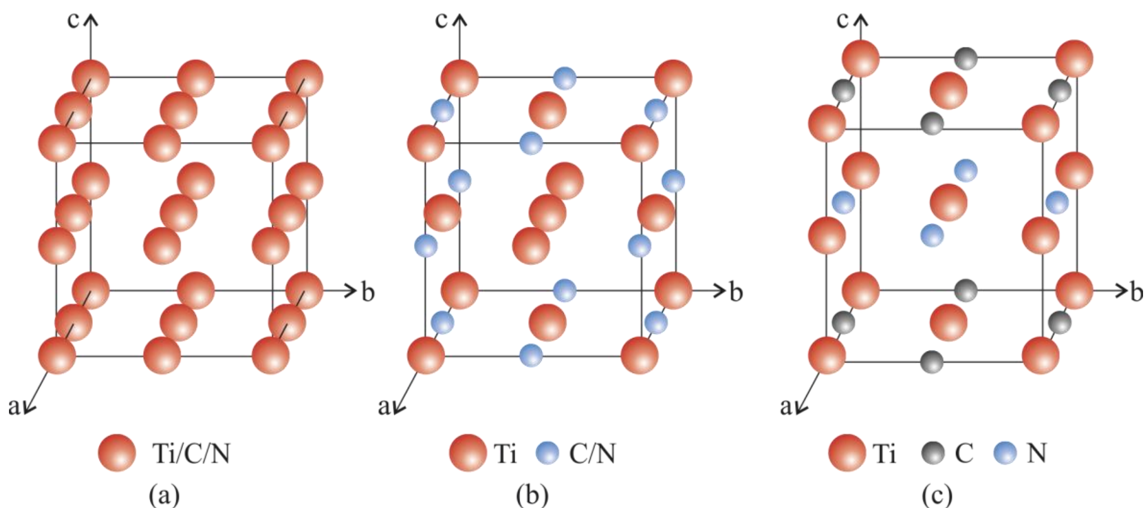


**Fig. 6** Possible structure models of Ti(C,N): (a) Model I, (b) Model II, (c) Model (III). Redrawn from Levi et al. (1998).

As mentioned above, $TiC_xN_{1-x}$ can be seen as a solid solution of TiC and TiN where the C atoms in the Ti lattice could be substituted by N atoms in any proportion (Zhang, 1993), thus showing Model I (Fig. 6(a)) to be unrealistic. After Levi et al. (1998) Model II (Fig. 6(b)) represent the FCC (NaCl) structure type where C atoms substitute for N atoms leading to ordered Ti and disordered C/N sublattices further suggesting to include random vacancies within the nonmetallic sublattice to conserve stoichiometry. Model III, however, assumes full ordering for a $TiC_{0.5}N_{0.5}$ crystal described by a tetragonal unit cell (Fig. 6(c)). Karlsson et al. (2000), describes the mechanical properties of $TiC_xN_{1-x}$ ($0 \leq x \leq 1$) films thus demonstrating that the continuous solid solution series shows different properties concerning stress, strain, hardness and modulus.

## 2.3 MAX Phases

Nowotny (1971) and his coworkers in Vienna discovered more than 100 new carbides and nitrides, amongst which, the "H-phases" (hexagonal complex carbides) and their relatives $Ti_3SiC_2$ and $Ti_3GeC_2$ were described. Barsoum & El-Raghy (1996) synthesized relatively phase-pure samples of $Ti_3SiC_2$ and created a material combining metallic and ceramic properties being, on the one hand electrical and thermal conductive and machinable, on the other hand resistant to oxidation. Barsoum et al. (1999) discovered $Ti_4AlN_3$, realizing that these phases shared a basic structure giving them similar properties. Barsoum (2000) launched the term "MAX phases" for a class of ternary carbides and nitrides more precisely called "$M_{n+1}AX_n$ phases" (n=1, 2, or 3), where M is an early transition metal (Sc, Ti, V, Cr, Zr, Nb, Mo, Hf, Ta), A is an A-group element (Al, Si, P, S, Ga, Ge, As, In, Sn, TI, Pb, and as an exception Cd) , and X is C and/or N.

### 2.3.1 Crystal structure

According to the above mentioned MAX's phase general structure Fig. 7 shows the 211, 312, and 413 phases of $Ti_{n+1}SiC_n$.

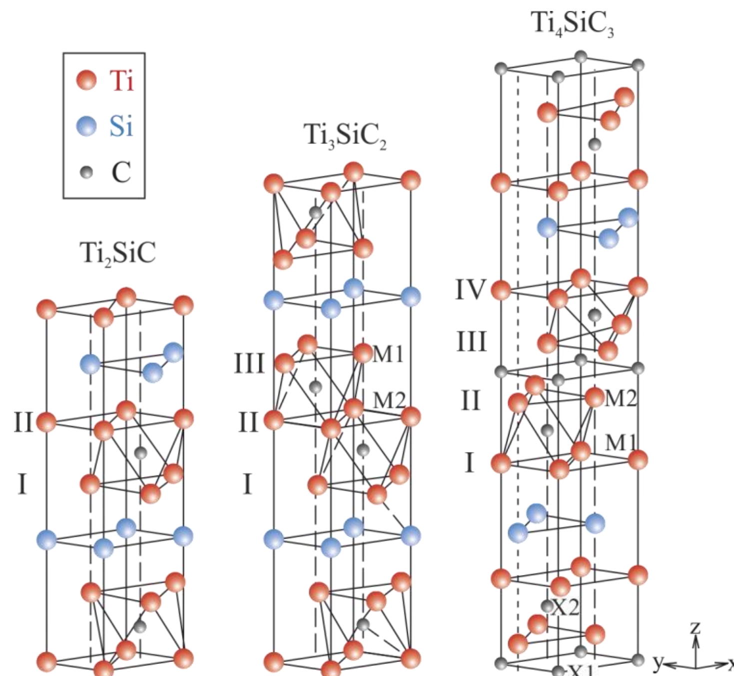


**Fig. 7** The hexagonal crystal structure for the $Ti_{(n+1)}SiC_n$ phases showing the different stacking sequences in z direction. Adapted from Barsoum and El-Raghy (1996).

The unit cells consist of $Ti_6C$ octahedral interleaved with layers of Si. The three structures differ in the number of Ti layers separating the A layers. There are two, three and four separating Ti layers in the 211, 312 and 413 phases respectively (Eklund et al., 2010). The TiC layers are twinned with respect to each other, separated by a Si mirror plane. In the 312 and 413 structures, there are two different Ti sites, those neighboring Si, and those not, designated as M1 and M2, respectively. In the 413 structure, there exist also two nonequivalent C sites referred to as X1 and X2 (Fig. 7) (Eklund et al., 2010).

Since the 1960's the Ti-Si-C system is one of the best described MAX phase systems (Jeitschko and Nowotny, 1967) as in particular, $Ti_3SiC_2$, might become important for many applications including wear-protective coatings and electrical contacts (Emmerlich et al., 2004).

# 3 Experimental techniques

The main tool used within this thesis is the (scanning) transmission electron microscope (STEM). Nonetheless X-Ray diffraction experiments have also be performed on one sample type. The following chapter briefly explains the applied methods along with sample preparation techniques.

## 3.1 Utilized Instrumentation

In this work three types of electron microscopes have been applied all manufactured by the FEI Company, a Tecnai F30 operated at the Johannes Gutenberg University in Mainz, a Tecnai F20 and a Titan$^3$ both located at the FELMI-ZFE in Graz. The two latter ones are displayed in (Fig. 8), important characteristics are listed in Table 2.

**Table 2** Electron microscope specifications

| Type | Tecnai<br>FELMI-ZFE (Graz) | Tecnai<br>JGU (Mainz) | TITAN³<br>FELMI-ZFE (Graz) |
|---|---|---|---|
| **Acceleration voltage** | 200 keV | 300 keV | 300 keV |
| **Electron source** | Schottky FEG | Schottky FEG | X-FEG |
| **Monochromator** | yes | no | yes |
| **$C_S$ probe-corrector** | no | no | Hexapole (Ceos GmbH) |
| **EDXS-detector** | Si(Li) with Moxtex window (EDAX Inc.) | | 4 quadrant SDD detectors (Bruker) |
| **HAADF/ADF/BF** | YES | YES | YES |
| **EELS-detector** | Quantum energy filter (Gatan Inc., USA) | Tridiem 863 energy filter (Gatan Inc., USA) | Quantum ERS (Gatan Inc., USA) |
| **CCD** | 2x2 k Ultrascan | US4000, 4kx4k | 2x2 k Ultrascan |
| **Add-ons** | | Digistar: electron beam precession (Nanomegas SPRL, Belgium) | |

X-ray diffraction spectra were recorded on a Siemens D5005 powder diffraction system with the Bragg-Brentano $\theta/\theta$ geometry. The Cu Kα X-ray source was operated at a generator voltage of 40 kV and a current of 40 mA during all measurements.

**Fig. 8** Electron microscopes mainly used within this work at the FELMI-ZFE in Graz: (a) FEI TITAN³, (b) FEI Tecnai 200.

### 3.1.1 Sample preparation

TEM lamellae for Ti(C,N) and TiSiC samples were prepared on an Omniprobe™ support grid using a dual beam focused ion beam FIB/SEM (FEI NOVA 200 Nanolab) microscope. A standard lift out technique was used, finished with a 5 keV polishing step to reduce the preparation induced amorphous layer.

WC bulk sample preparation has been carried out by mechanical preparation and a following ion milling step to electron transparency with a precision ion polishing system (Gatan PIPS). For this purpose, some material was cut out of the bulk sample using a diamond wire saw (Well) and was formatted to a disk of ~3 mm with an ultrasonic disc cutter (Gatan), furthermore, has been ground and polished by using SiC abrasive paper and diamond paste. Using a dimple grinder (Gatan), a sphere-shaped deepening is ground into the polished disk. The ion milling process to electron transparency was performed in the PIPS. In this thinning tool, two $Ar^+$ ion beams are focused on the middle of the dimple-ground sample under typical low angle ion milling conditions (6°/4°) from both sides at 4 kV, until a hole is formed at the center position where the sample is only a few tens nm thick.

## 3.2 Transmission Electron Microscopy

The following pages are devoted to the principles of transmission electron microscopy giving an insight into the general setup itself as well as the imaging, diffraction and spectroscopic capabilities the instrument offers.

### 3.2.1 General Setup

Since the development of the TEM (conventional TEM or CTEM) (Knoll and Ruska, 1932) and the first STEM (scanning transmission electron microscope) (von Ardenne, 1938) lots of effort has been put into refining this technique not only by the means of aberration correction but also by the increased computational power. Since the early days of electron microscopy the limiting factor regarding resolution is given by lens aberrations and Scherzer (1949) already proposed a multipole corrector, compensating for the spherical aberration of the objective lens consisting of non-rotationally symmetric elements. However, the project in building such a corrector failed due to mechanical and electromagnetic instabilities (Rose, 2009). It took until the second half of the 1990s that working correctors have been built, using two different multipole lens configurations: The quatrupole-octopole configuration as proposed by Krivanek et al. (1997) in Cambridge and the hexapole configuration proposed by Haider et al. (1995) in Germany. Probe correction within this thesis took advantage of the hexapole-type corrector (Haider et al., 2000). So today (S)TEM permits imaging and chemical analysis at single-atom scale (Crewe et al., 1970; Krivanek et al., 1999; Pennycook, 2017).

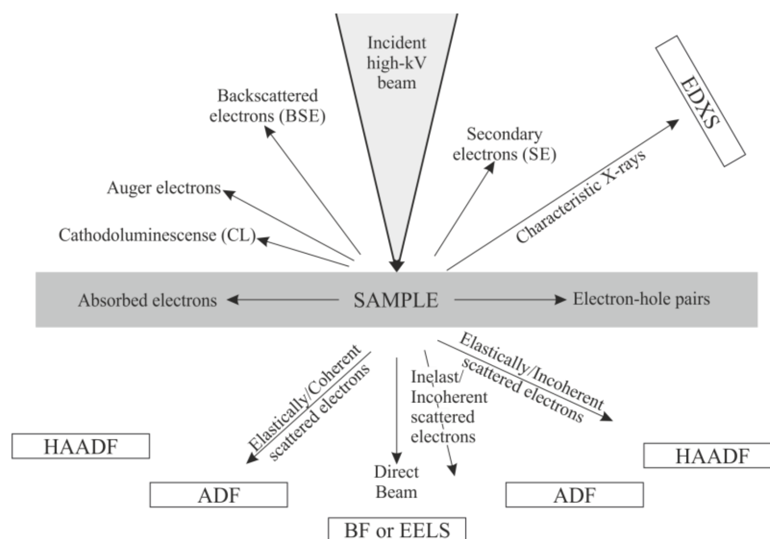


**Fig. 9** Signals generated when high energetic electrons interact with matter. The ones used in our (S)TEM instrument are those pointing towards a detector.

The basic principle of transmission electron microscopy (TEM) and difference over scanning electron microscopy (SEM) is that a highly energetic convergent (in STEM) electron beam passes through a thin sample (usually <100 nm) interacting with the matter. These primary electrons as well as secondary electrons and X-rays created along with this interaction yield valuable information on the structure, composition and morphology of the sample (Fig. 9). As stated above, two modes of TEM operation can be discriminated: CTEM and STEM:

In CTEM, the illumination of the sample is done by a parallel electron beam. After an electron emitting source the condenser lens is found above the specimen, being responsible for illuminating the sample and determining the size of the convergence angle, measurable via the convergent beam electron diffraction (CBED) pattern. Following the sample are the objective lens and the projective lenses. After the objective lens a first intermediate image is generated and after the projective lens is the image plane (viewing screen) which shows either a diffraction pattern (DP) or the final image. Due to the strength of the intermediate lens the operator can switch between imaging and diffraction mode selecting either the image plane (intermediate image 1) or the back focal plane (BFP) of the objective lens as its object like depicted in Fig. 10(a, b). In image mode one can use objective apertures with different diameters to enhance the contrast, as a raise in contrast is achieved by blanking out electrons scattered to higher angles. This method is called bright field (BF) imaging if the objective aperture is centered on the undiffracted beam and used for forming the image. On the opposite, dark field (DF) imaging only uses a certain selected diffracted beam, selected by the objective aperture, for image formation.

In STEM mode, a highly focused electron beam forms an electron probe, as small as 50 pm in aberration corrected microscopes (Krivanek et al., 2003). This convergent probe is scanned over the sample pixel by pixel using two pairs of scan coils between the $C_2$ lens and the upper-objective polepiece (Fig. 10(c)). This double-deflection process provides the probe to remain parallel to the optic axis as it scans across the sample surface (Williams and Carter, 2009). Thereby the lateral position of the beam can be controlled precisely, thus information on the sample can be obtained very localized. A big advantage is, that different signals can be collected simultaneously. Electrons scattered to different angels can be collected with different detectors collecting electrons at different angles as elucidated in Fig. 9 dependent on the annular range of the detector, varied by the camera length, high-angle annular dark field (HAADF), annular dark field (ADF), annular bright

field (ABF) and bright field detectors can be distinguished. Contrast in images recorded on an ADF detector, depending on material and scattering angle, can be influenced by coherently scattered Bragg beams, thus the contrast cannot purely be related to the atomic number of the investigated material (Donald and Craven, 1979). The contrast in HAADF is mostly formed by incoherently Rutherford scattered electrons, by the nuclei of the atoms, thus being proportional to the atomic number Z of the material, therefore called Z contrast. HR-ADF and HAADF imaging can be reached by selecting an appropriate sample using a fine focused electron probe using aberration correction.

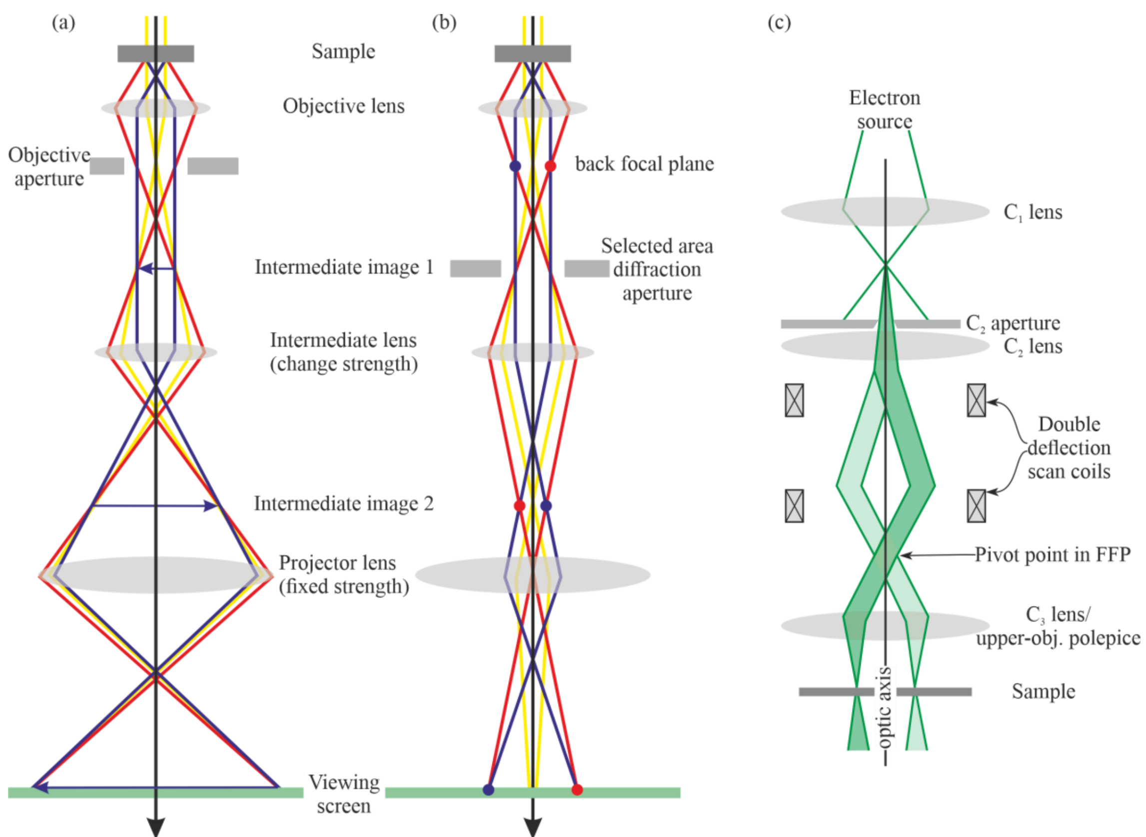


**Fig. 10** Simplified diagram of the two basic TEM operation modes: (a) diffraction and (b) image mode. (c) Schematic of STEM image formation as described in the text. Redrawn from Williams and Carter (2009).

Simultaneously characteristic X-rays generated by ionization events can be detected by energy dispersive X-ray spectroscopy (EDXS) and the energy-loss of primary electrons due to inelastic scattering can be analyzed with an electron energy-loss spectrometer (EELS). In the STEM spectrum imaging (SI) mode, a complete spectrum at each pixel position is acquired to build up the SI on a spectrum-by-spectrum basis. Thus, a data cube is created where two of the cube axes correspond to spatial information, while the third dimension represents the EEL and/or EDX spectrum.

### 3.2.2 Electron beam monochromation

In a TEM the electron beam has an energy spread $\Delta E$ in the range 0.3 eV to 1 eV, which depends on the type of electron source used (Lopatin et al., 2018). This spread leads to a broadening of the peaks in the EEL spectrum, which reduces the amount of fine structure that can be resolved. To reduce the energy spread of the field emission gun (FEG) a monochromator can be installed after the electron source. Fig. 11 shows one type of gun monochromator, working after the Wien filter principle within a TECNAI or TITAN microscope.

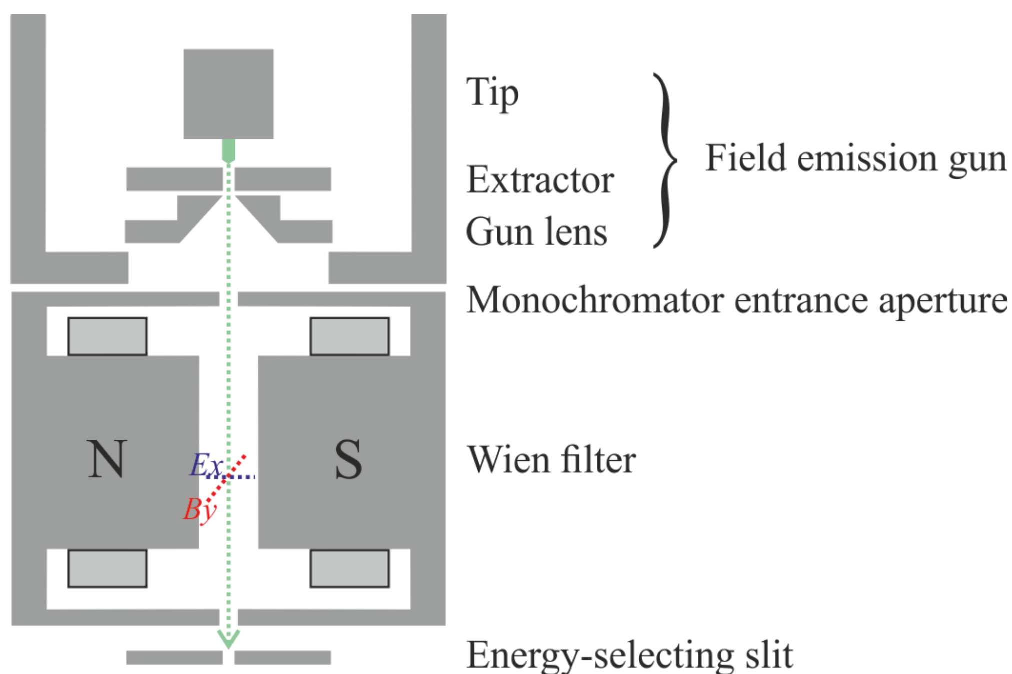


**Fig. 11** Sketch of a FEG and a monochromator working after the Wien filter principle. Redrawn from Tiemeijer (1999).

Two crossed fields, an electric field $Ex$ and a magnetic field $By$, which are normal to each other, are applied perpendicular to the beam. Thus equal and opposite forces are applied to the electron beam (Tiemeijer, 1999). The strength of the electric and magnetic field is constant along the length of the monochromator. The net force is zero when $(-e)vBy + (-e)Ex = 0$ is satisfied only for a single electron velocity $v$. Faster or slower electrons are dispersed according to their energy and removed by the energy-selecting slit (Egerton, 2005).

### 3.2.3 EELS imaging and spectroscopy

The most common system is the post column (mounted underneath the viewing screen) image filter manufactured by Gatan Inc., USA, called Gatan image filter (GIF), which has been used throughout this work. The advantage over simple EEL spectrometers is, that they act both as a filtering imaging device and an EEL spectrometer. The main parts of an energy filter shall be described in Fig. 12:

(1) Spectrometer entrance aperture (SEA): It defines (along with the camera length) the collection angle of an EELS experiment. In spectrometry smaller apertures improve the energy resolution, whereas for imaging larger apertures are of advantage.

(2) Magnetic prism: it bends the electrons and disperses them according to their kinetic energy - lower energy electrons get bent stronger. Furthermore, the magnetic prism demagnifies and focuses the spectrum on the energy selecting slit.

(3) Drift tube: is an electrically isolated tube within the magnetic prism. It allows the offset of an EEL spectrum through the application of a voltage.

(4) Energy selecting slit: This slit allows to select electrons with a certain energy to pass through and is the centerpiece for energy filtered TEM (EFTEM) imaging.

(5) Multipole lenses: are operated either in imaging or spectroscopy mode so that either an image or a spectrum gets recorded on the CCD camera. Their function is to suppress unwanted spatial, angular or spectral information and minimize aberrations.

(6) CCD camera

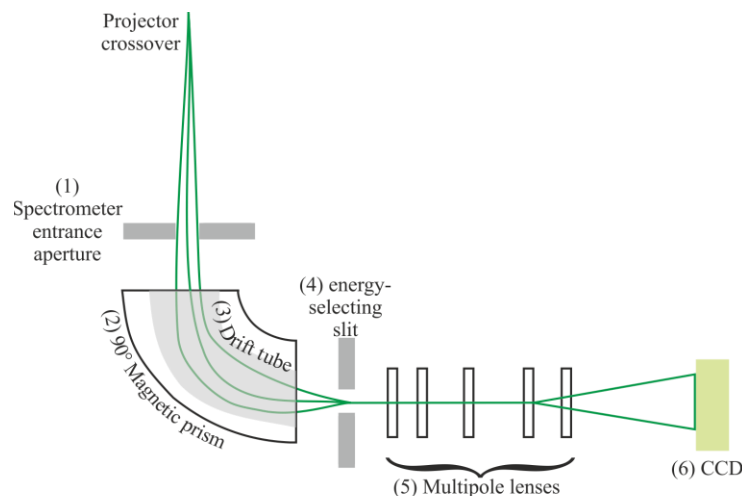


**Fig. 12** Schematic sketch of a post column image filter, numbers as indicated in the text.

### 3.2.4 Multi-slice image simulations

Simulating high resolution images is widely used for comparison and interpretation of experimental data. For simulating finite thickness materials, the multislice approach (Kirkland, 2010) is often used. It was first introduced by Cowley and Moodie (1957).

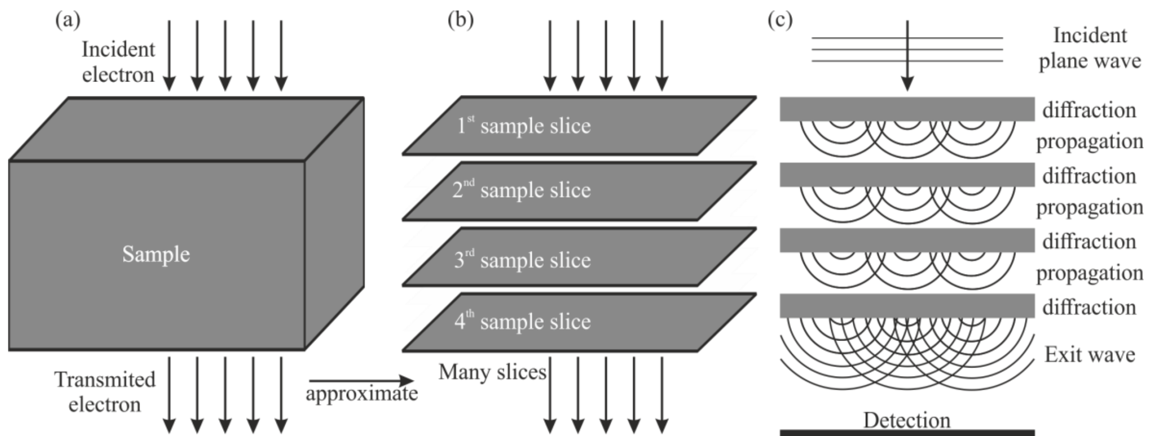


**Fig. 13** (a) Using the multislice approximation the sample gets converted into (b) many thin slices. (c) An incident electron plane wave (shown for CTEM, not shown for STEM) is propagated trough a crystalline sample and exits on the bottom. Each thin slice gets approximated as a simple phase shift of the electron wave which is propagated between slices as a free space wave. Redrawn from Kirkland (2006).

In most cases, electrons, when passing though the sample, will undergo multiple (or dynamical) scattering (Kirkland, 2006). For understanding the image formation, it is necessary to calculate the propagation of an electron from scattering event to scattering event until the detector is reached. To describe the interaction of an electron with a crystal one has to solve the Schrödinger equation (Williams and Carter, 2009). It describes the behavior of the electron by its quantum mechanical wave nature within the potential field of a crystal. For HR-CTEM images the plane wave approach is used, whereas a small focused probe at each position of the sample (Fig. 13(a)) is used for HR-STEM images (Kirkland, 2006). For simulation the sample is approximated by dividing it into slices perpendicular to the electron beam (Fig. 13(b)). Within each slice the potential field is approximated to be constant and the Schrödinger equation is solved slice by slice (Kirkland, 2010). The slices should ideally correspondent to the existing atomic layers in the sample (Fig. 13(c)). Further aberrations and angular conditions should be included in the calculations as known from the experiment. Within this work QSTEM (v.2.4) was used (Koch, 2002). Crystallographic data files of the desired structure can be easily imported when converted into ".qcs" files for further image simulation.

## 3.3 Electron Diffraction

Diffraction in a crystalline medium occurs because of the wave nature of the incident electrons and interference between the scattered electron waves with the crystal. Thus, the continuous distribution of scattered intensity changes into one that has a sharp peak at angles characteristic for the atomic spacing. This elastic scattering event is then called diffraction (Williams and Carter, 2009). It can be applied to single crystals as well as polycrystalline materials for phase and lattice parameter determination.
The Bragg equation for X-rays (Bragg and Bragg, 1913) is also valid for electrons (Davisson and Germer, 1927):

$$n\lambda = 2d_{hkl}\, sin\theta_{hkl} \quad (1)$$

It links the lattice planar spacing of the hkl crystallographic planes (d) to the wavelength ($\lambda$) of the incident electrons (or X-rays) and the scattering angle (θ).
Diffraction only occurs for reciprocal lattice points which are located on the surface of the Ewald sphere. This sphere has a radius of $1/\lambda$ around the diffraction center, thus linking real and reciprocal space (Fig. 14).

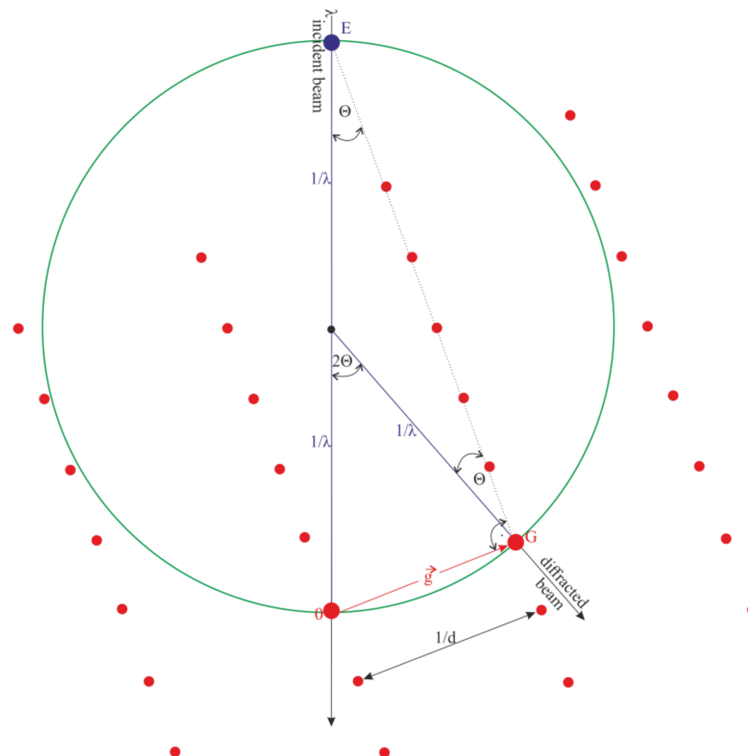


**Fig. 14** Ewald sphere construction scheme

Within the field of electron diffraction the sample illuminating probe can be formed either parallel, nearly parallel or convergent dedicated to selected area electron diffraction

SAED, nano electron diffraction (NED), or convergent beam electron diffraction (CBED) respectively, which will be discussed in the following.

### 3.3.1 Selected area electron diffraction (SAED)

Developed by LePoole (1947) a large sample area gets illuminated under parallel illumination conditions. Therefore one can define the position on the sample for investigation by using a SAED diaphragm of the desired size, thus the resolution is aperture limited. The resulting diffraction pattern is given in the form of dot-like reflexes as depicted in Fig. 15(a). The insertion of a SAED aperture in the image plane creates a virtual aperture (VA) at the entrance surface of the sample, thus only electrons falling inside this VA are allowed trough the imaging system (Fig. 15(a)). It should be also noted that using a parallel probe, only scattering vectors of the zero order Laue zone get excited, i.e. only these that do not have components parallel to the incident beam (Fig. 14).

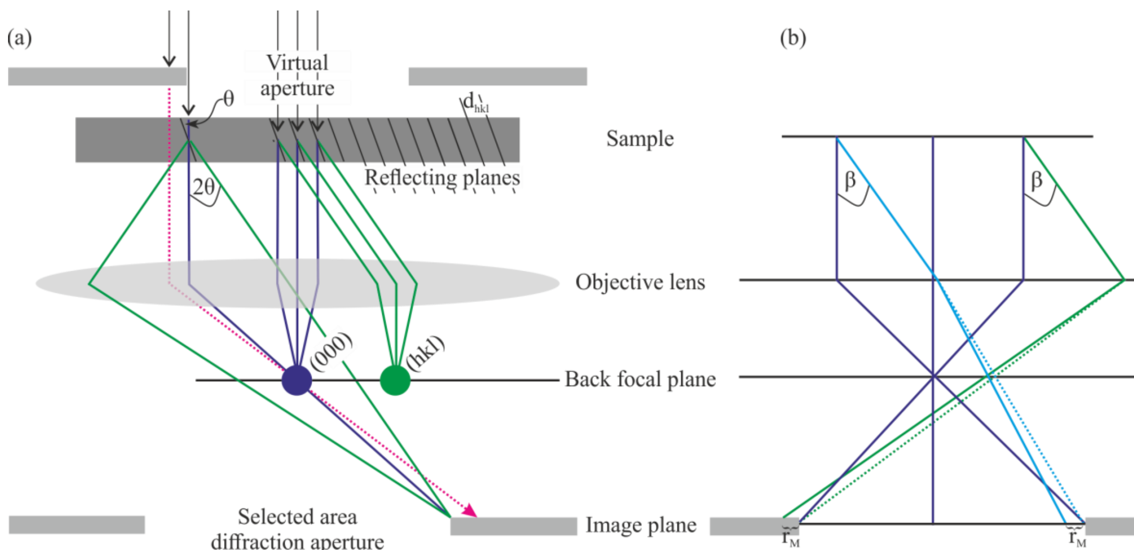


**Fig. 15** (a) Ray diagram showing SAD pattern formation (b) Spherical aberration of the OL causes an error in selecting the area if the beam does not pass at the same angle to the optical axis. Redrawn from Williams and Carter (2009).

However, as a result of the spherical aberration of the objective lens, the minimum size of the diffracted area is about 500 nm (Morniroli, 2002). One cannot precisely select a smaller area because beams which are positioned farther away from the optic axis will be bent stronger when passing through the objective lens. The image formed at magnification M is translated by $r_M$:

$$r_M = MC_s\beta^2 \quad (2)$$

with $C_s$ being spherical aberration constant, and $\beta$ is the angle under which diffracted beams enter the objective lens (Williams and Carter, 2009). Therefore, the selected area is only correct for the undiffracted beam (Fig. 15(b)). The diffracted area is relatively large, thus it can contain thickness changes and orientation variations of the lattice planes, which results in an inaccurate, "averaged" diffraction pattern (Morniroli, 2002).

### 3.3.2 Convergent beam electron diffraction (CBED)

By choosing small probe size, like in STEM, the electron beam can be converged, such that only the area of interests is illuminated by the probe. Diffraction disks (e.g. Kossel-Möllenstedt pattern, visible as discs on the BFP) are resolved individually for a convergence angle smaller than the Bragg diffraction angle (Fig. 16) (Wang, 2016).

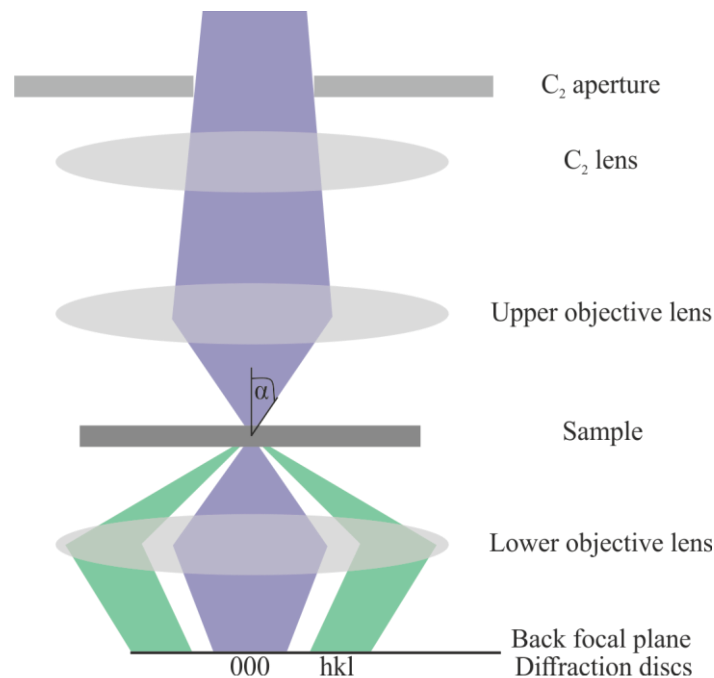


**Fig. 16** Ray diagram showing CBED pattern formation. Redrawn from Williams and Carter (2009).

By exciting higher order Laue zones (HOLZ), the reconstruction of the three dimensional crystal lattices is possible, where the HOLZ line symmetry (Fig. 17) provides a fundamental principle for the determination of point and space groups (Braue, 1990). The sharp lines within the discs arise from three-dimensional diffraction. They are the result of scattering by the planes in higher order Laue (HOLZ) zones. These HOLZ lines are sensitive to small changes in lattice parameters, e.g. due to stoichiometric changes. The HOLZ lines occur, like Kikuchi lines that arise from zero order Laue zone (ZOLZ) planes,

in pairs with a bright (excess) line associated with the HOLZ disc responsible for it and a parallel, dark deficiency line present in the direct (000) disc (Fig. 17(c)). The sharp lines outside the discs are the result of inelastic scattering from the HOLZ planes.

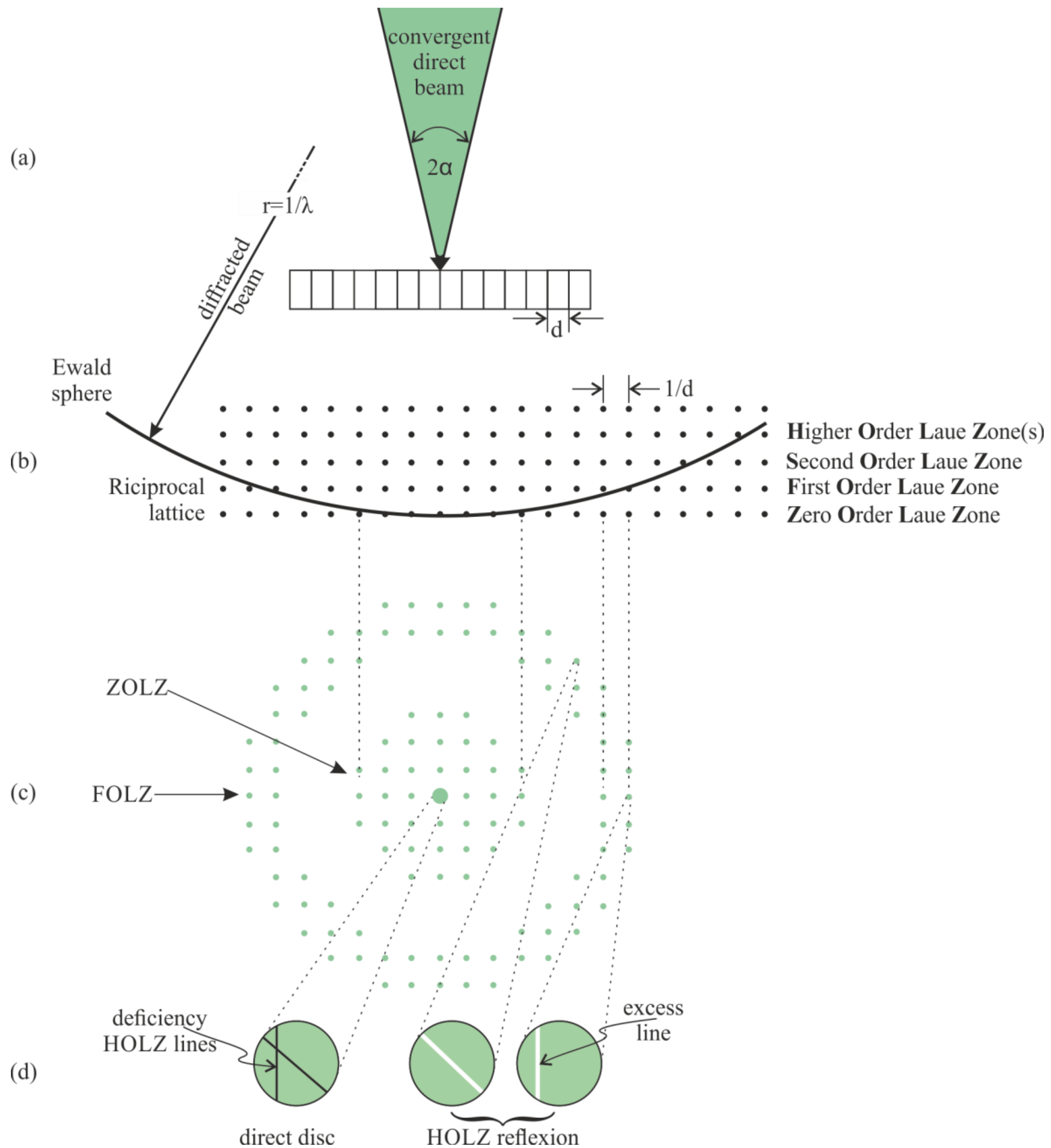


**Fig. 17** Geometrical relation between (a) a convergent formed probe on an oriented crystal, (b) the curvature of the Edwald sphere intercepting with (c) ZOL- and HOL zones and (d) CBED pattern showing excess and deficiency lines. Adapted from Braue (1990).

### 3.3.3 Nano Electron Diffraction Tomography (NEDT)

The electron-beam geometry used for NED is essentially the same as for CBED (Cowley, 1999). As discussed above, the $C_2$ aperture is the main probe forming element thus confining the resolution. Therefore, quasi parallel illumination is also sought for in CBED that could be gained by using a small $C_2$ aperture to decrease the beam diameter down to a few nanometers and reduce the size of the diffraction disks. This approach is referred here to nano electron diffraction (NED) with reference to the beam size. This approach is well known for "classical" electron diffraction studies of nanomaterials (Kolb and Matveeva, 2003). Nano electron diffraction tomography (NEDT) (derived from the Greek tomo (τομw) = cut or slice; and grapho (γραφω) = record) allows to sample the reciprocal space in small by tilting the sample crystal around an arbitrary axis (Fig. 18(a)). For each tilting step, a diffraction pattern gets collected to obtain a 3D image stack in the end.

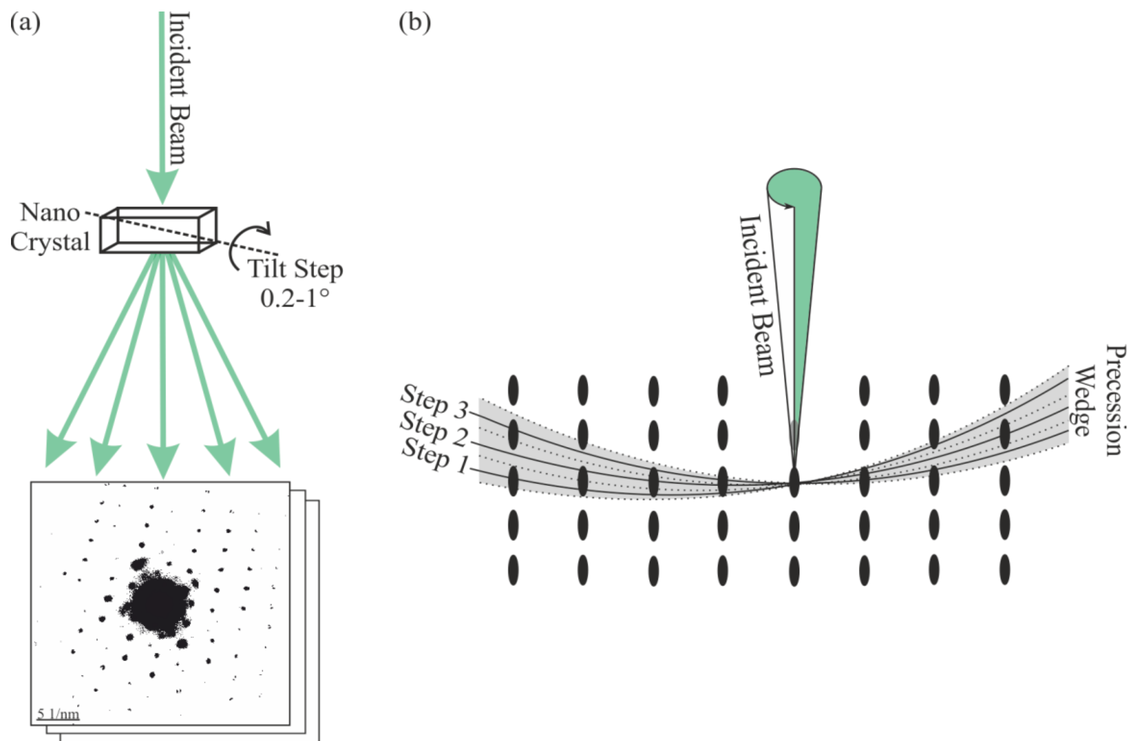


**Fig. 18** (a) Schematic of how a stack of diffraction patterns is created by tilting a crystal sequentially. (b) Sketch of how precessing the beam influences the experiment: the black lines indicate the Ewald sphere position for each tilting step without precession while the shaded area shows the integration range while precessing the beam (for simplicity the reciprocal space is drawn stationary while the Ewald sphere is moved for each tilting step). Redrawn from Kolb et al. (2009).

Because of the thin nature of the sample and the convergence of the electron beam, the reciprocal lattice consists of rods rather than points, the diameters of which are proportional to 2 times the half convergence angle and the lengths of which are inversely proportional to the sample thickness (Champness, 1987). Electrons interact with matter

stronger than e.g. X-rays, therefore multiple diffraction events occur, denoted as dynamical effects, whose probability is a function of specimen thickness, leading to a loss of information about the actual scattering strength, depicted in (Fig. 19) for two beams.
To overcome this unwanted phenomenon an approach, called precessed electron diffraction (PED), was developed to reduce dynamical effects in electron diffraction patterns (e.g. Own et al., 2004; Vincent and Midgley, 1994). PED means that the primary electron beam gets inclined away, using a certain tilt angle, from the TEM's optical axis by using the scan and de-scan coils (Fig. 20) upon sample tilting at an optimal precession angle, thus the data in between the tilting steps gets integrated as highlighted in gray Fig. 18(b). A diffraction pattern acquired in this mode is the sum of patterns sequentially produced by the precessed beam.

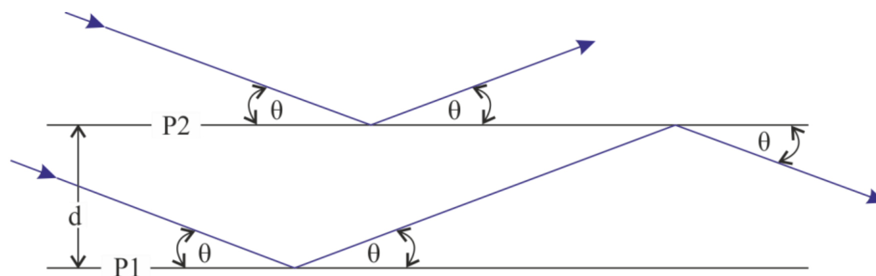


**Fig. 19** The origin of dynamical diffraction is that diffracted beams that meet the Bragg condition are necessarily in the same condition to be re-diffracted back into the incident beam. Redrawn from Williams and Carter (2009).

For determining the structure, the 3D reciprocal volume can be reconstructed, as the information about the angular relationship between the diffraction patterns is accessible. Although the TEM offers the possibility for determining structural information of nano materials in reciprocal space, diffraction instrumentation is underdeveloped, thus lacking processing routines, which are available for X-ray diffraction techniques, which makes ED techniques inferior to them (Kolb et al., 2009).

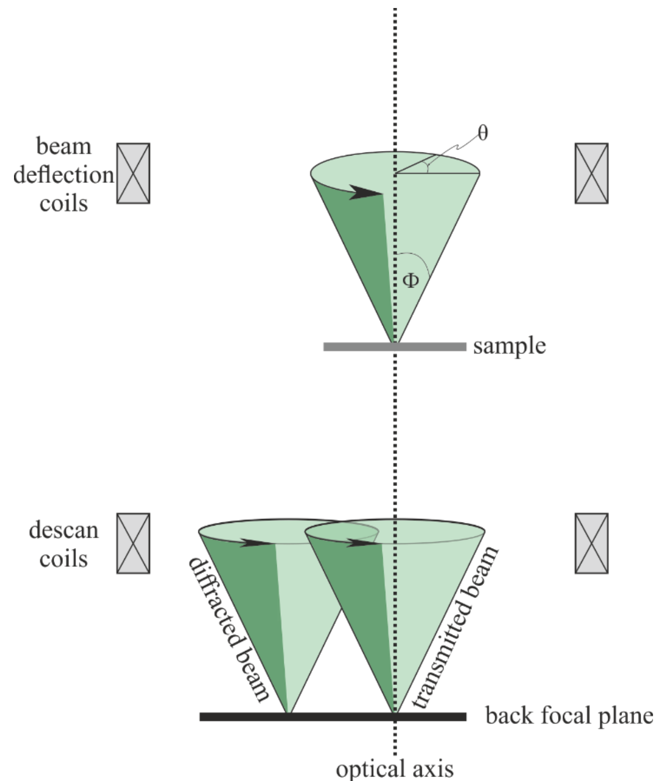


**Fig. 20** Schematic showing how a precessed beam (through the angle θ = 2Π) is tilted off zone-axis by ϕ using the beam deflection coils, while below the sample descan coils operate to restore the zone axis pattern. Redrawn from Own et al. (2004).

Working with such a small beam in TEM image mode makes it nearly impossible to accurately position the beam on a crystal. Besides the inconvenience from switching back and forth from imaging to diffraction mode, prone to beam shifts, working in STEM mode with HAADF reference imaging is preferred (Kolb et al., 2007).

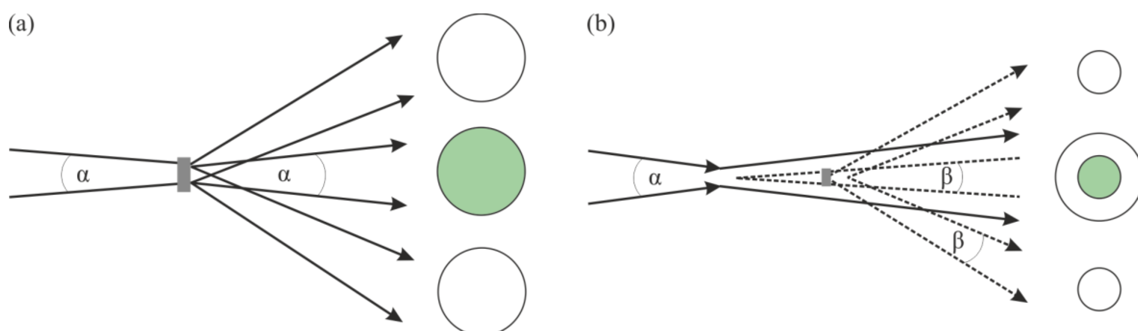


**Fig. 21** Defocus effect on diffraction spots size in NED patterns. (a) shows that the beam is focused on a thin sample showing the angular spread of the diffraction spots equals α (convergence angle). (b) shows the case for a defocused objective lens so at the sample the beam diameter is greater than the crystallite diameter. The size of the diffraction spot depends on the collection angle β (smaller than α) subtended by the crystallite at the beam cross-over. Redrawn from Cowley et al. (2000).

Kolb et al. (2007) suggests to use a sufficiently small aperture (10 µm) and an accurately defocused (Fig. 21) incident beam to archieve an almost parallel beam for coherent

electron diffraction, resulting in illumination conditions equal to NED, combined with the advantages of the STEM mode.

Because the collection of electron diffraction tomography datasets is a time-consuming task and therefore difficult to adapt to in polymorphic systems (Kolb and Gorelik, 2006), Kolb's working group (Kolb et al., 2007) developed the first automated electron diffraction tomography (ADT) routine, combining precessed nanodiffraction and HAADF imaging:

By using the "Automated Experiments Module" in the FEI's user interface one has to select a suitable crystal in STEM mode at the starting tilt position. The crystal is then tilted automatically in small, fixed tilt steps around an arbitrary axis while sequentially recording diffraction patterns, thus sampling a large reciprocal volume. The crystal can be tracked during the tilt by cross-correlation of HAADF images taken at consecutive tilt steps and takes account for the shift of the crystal. The collected diffraction patterns are arbitrary slices through the reciprocal space, usually not showing any high symmetry. They can be saved in various formats (e.g. MRC) and can be seen as a 3D data stack to be processed further using the ADT3D program, distributed via NanoMEGAS SPRL, Belgium, for reciprocal space reconstruction, unit cell parameters determination, reflections indexation followed by symmetry determination structure solution and refinement.

### 3.3.4 Diffraction pattern treatment

Simulations are an inevitable tool when it comes to analysis of SAED and CBED patterns. With the help of a crystallographic data file one can perform simulations on electron diffraction patterns. Within this work the Java Electron Microscopy Simulation (JEMS) software (V.3, 2017) was used (Stadelmann, 2004).

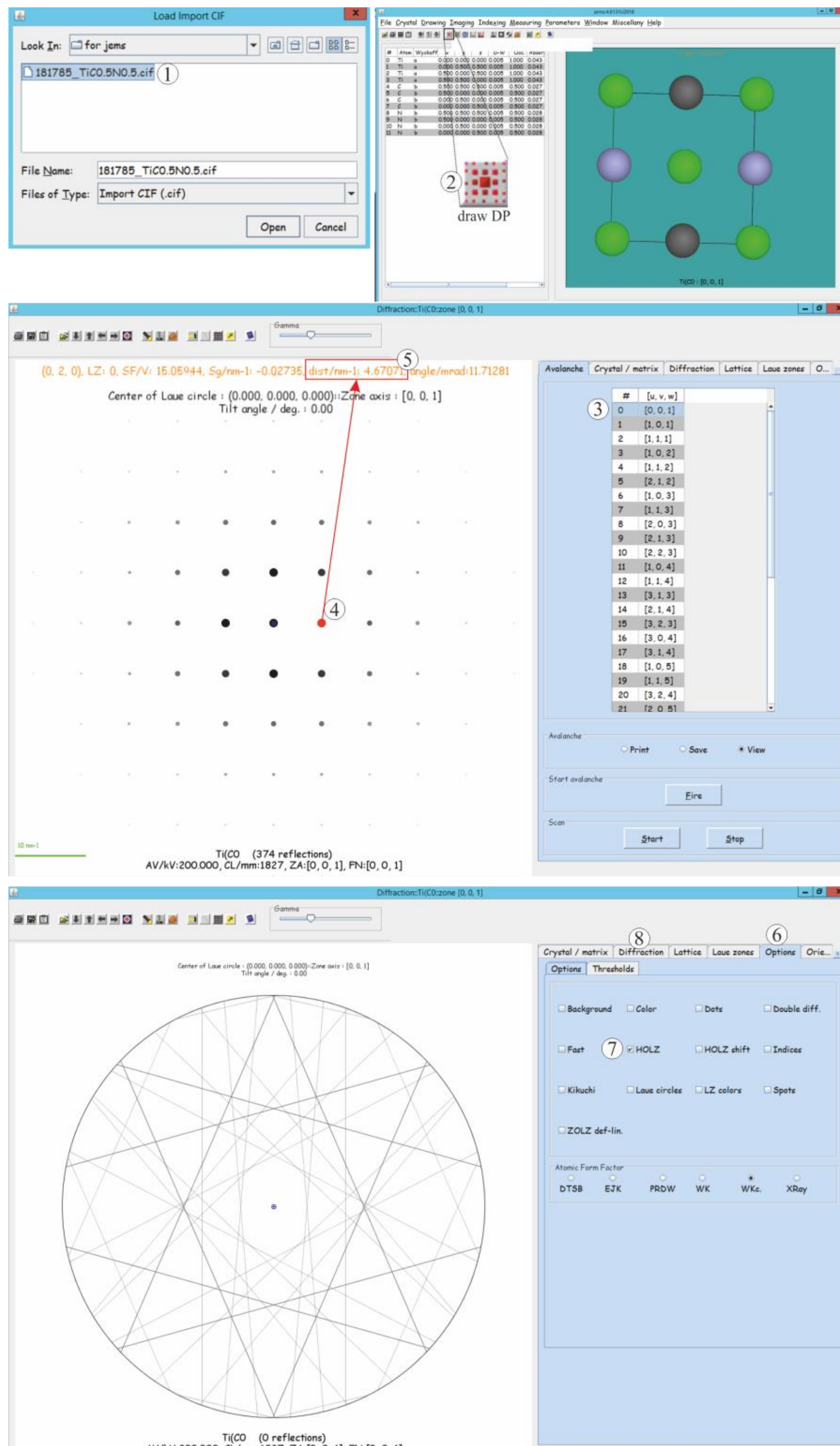


**Fig. 22** SAED and HOLZ-Line simulations with JEMS

On the one hand SAED patterns can be simulated and compared to experimental patterns to prove the structural model, on the other hand HOLZ lines can be simulated for different sample stoichiometries to verify the experimental results. As shown in Fig. 22 one can load a CIF file (1) in our case $TiC_{0.5}N_{0.5}$ and use the “draw diffraction pattern Icon” (2). The desired crystallographic direction [u,v,w] can be selected using the “Avalance” tab (3). The diffraction pattern is plotted in the plot area (4). By choosing a single spot, the distance to the central spot is given in reciprocal space (5), thus can be compared with the experimental pattern. HOLZ lines for a given orientation can be simulated by addressing the “Options” tab (6) and changing the tick mark from Spots to HOLZ (7). Within the “Diffraction” tab (8) the High Voltage (HV) can be adjusted according to the microscope’s settings as HOLZ lines can also be used to verify the HV.

When it comes to the analysis of NED pattern recorded with the ADT routine, the procedure follows a well-defined path described by (Gorelik et al., 2010; Kolb et al., 2008). The ADT experiment produces a 2D stack of diffraction patterns. This stack has to be transferred into a 3D set of diffraction data using the ADT3D software (Kolb et al., 2008; Gorelik et al., 2012). Further centering the diffraction patterns, background subtraction, tilt axis determination, 3D diffraction volume creation, 3D peak calculation, cell search and refinement to identify basis unit cell vectors, indexing of the reflections and extract corresponding intensities leads to hkl values. In a consecutive step, these intensities can be used for structure solution in the open source program SIR2014 (http://www.ba.ic.cnr.it/softwareic/sir/sir2014-download-2/) (Burla et al., 2015), which can be exported into a crystallographic information file (*.cif). The *.cif file can be used for various simulations.

#### 3.3.4.1 Creating a *.cif file from ADT data

The structural data acquisition can be performed in any standard TEM instrument. To create a cif file first and foremost a *.hkl file should be created. ADT experiments are performed by following the steps within the software as explained in detail by Kolb et al. (2008) and as depicted in the flow diagram in Fig. 23.

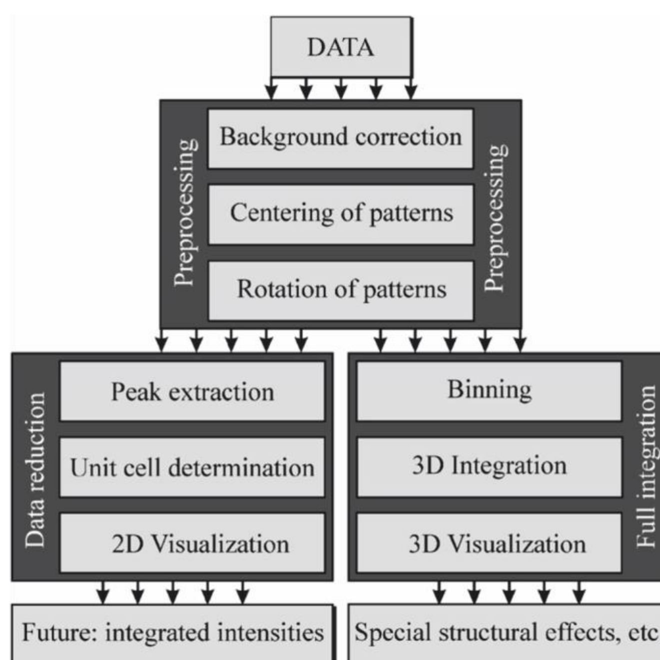


**Fig. 23** Flow diagram of steps used for the data processing. Taken from Kolb et al. (2008).

According to Fig. 23 the original experimental data should be preprocessed by the means of correcting the background on the patterns, before centering and rotating them to the tilt axis. Centering the diffraction pattern on the CCD while conducting the experiment helps on this point. Further procedures split up in the “full integration path” and the “data reduction” path. Once the unit cell basis vectors are defined, the set of found reflections can be indexed and intensities assigned to reflections can be extracted (Mugnaioli and Gorelik, 2012). This means a standard *.hkl file is generated and data is written in a

```
WC.hkl
1    5   0   0  802.31    28.33
2    5   0  -1 3625.13    60.21
3    5  -1   2 7727.60    87.91
4    5  -1   1 3237.66    56.90
5    5  -1   011103.21   105.37
6    5  -1  -1 6652.43    81.56
7    5  -1  -2 3220.72    56.75
8    5  -2   2 3145.82    56.09
9    5  -2   1 7759.17    88.09
length : 13 860   Ln : 1   Col : 1   Sel : 0 | 0   Windows (CR LF)   UTF-8   INS
```

**Fig. 24** Typical *hkl file of tungsten carbide.

standard crystallographic 3i4, 2f8.2 format. Fig. 24 shows a standard .*hkl file that can be used as input for crystallographic structure solution programs like SIR2014.
The structure of a *.hkl file is given in
(http://shelx.uni-ac.gwdg.de/tutorial/english/xprep.htm): It consists of reflections related to the reflection planes (hkl) of the crystal lattice. Each line corresponds to a measured reflection. The Bragg indices h, k, l, are found in the first three columns and define the lattice plane of the corresponding reflection. The following columns contain the intensities I of the reflections and the corresponding estimated standard deviation (e.s.d), defined as square root of the intensity.
With the help of SIR2014 a *.hkl file can be converted into a crystallographic information file (*.cif) by generating a new project.
Therefore, SIR2014 wants the user to generate a new project. The single steps are shown in Fig. 25 (a-f). Consecutively new windows show up that should be filled in by the user. By checking the data within the output box each window has to be accepted so that the procedure can continue: (a) The working directory has to be selected, a name on the structure has to be assigned and a job title has to be supplied. (b) The space group symbol has to be selected and the cell parameters (in Å) have to be entered according to the ADT results. (c) The size of the molecule and the data source as well as the elements contained in the unit cell have to be entered. (d) The *.hkl file has to be loaded. (e) Different structure solution models can be chosen. (f) A SIR2014 input file (*.sir) can be created.
Loading the SIR input file not only allows to visualize the structure and the adjustment of electron potential, it can also be saved as a *.cif file.
Many simulation programs are capable of reading this format including FEFF, JEMS QSTEM and many more. The file format was proposed by the International Union of Crystallography as a file structure for the distribution of crystallographic information (Hall et al., 1991). The newest conventions on the structure of this data file were published by (Brown and McMahon, 2002).

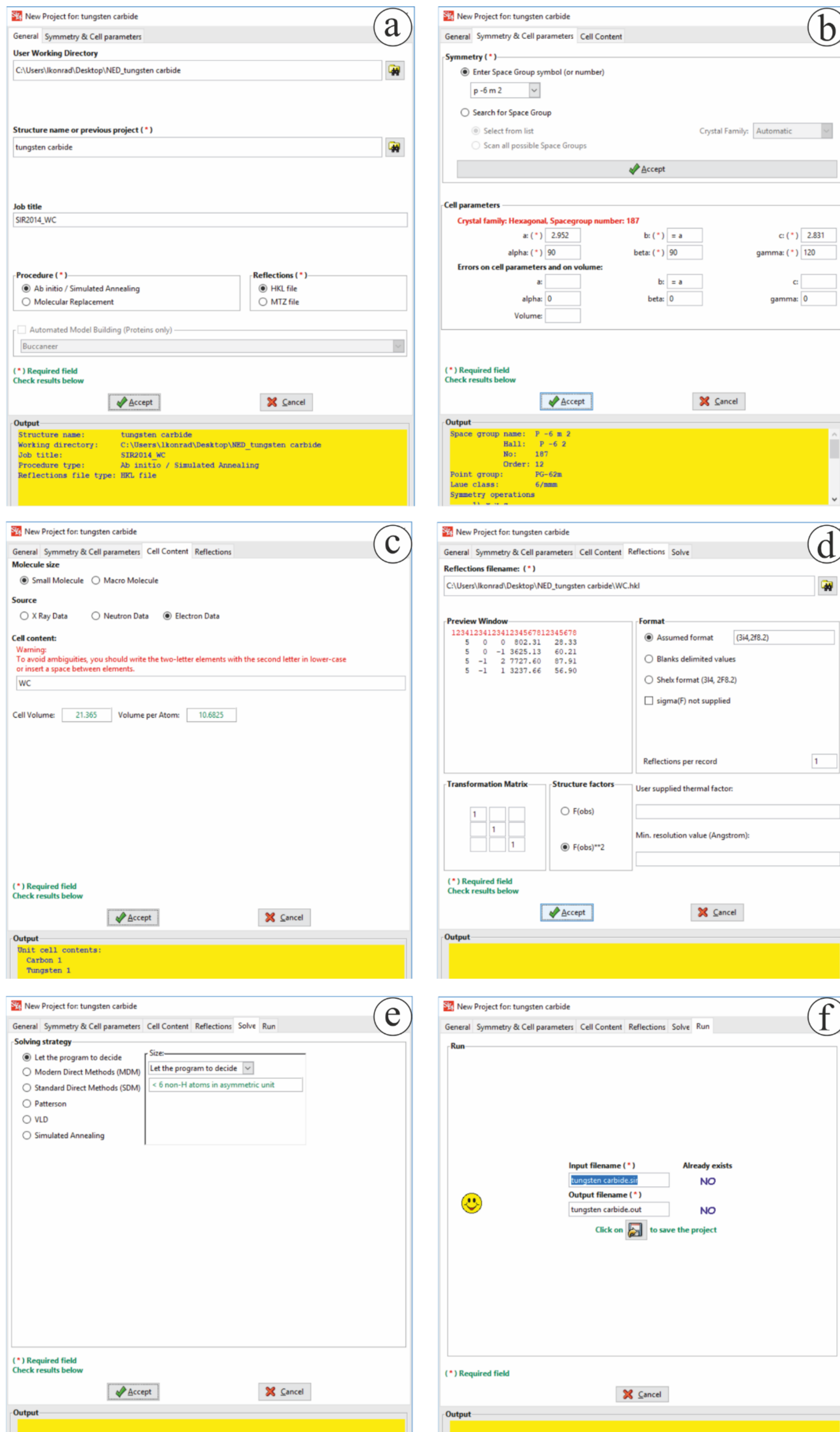


**Fig. 25** Creating a new project with SIR2014 in 6 steps (a-f).

## 3.4 Electron Energy-loss Spectroscopy (EELS)

Transmission EELS comprises analyzing the energy distribution of primarily almost monoenergetic electrons after they have interacted with a solid's constituent atoms. These electrons can be scattered either (a) elastically or (b) inelastically as their momentum is altered and in many cases, they transfer a substantial amount of energy to the sample:

(a) Elastic scattering can be coherent or incoherent. Most incident electrons scatter coherently through small angles (10-100 mrad) as they pass through the atom further away from the nucleus where the electrostatic field is weaker due to the screening effect of the atom's electrons (Egerton, 2011). Incoherent elastic scattering is represented by large angle (>100 mrad) Rutherford scattering resulting from direct Coulombic interaction between the primary electron and the nucleus. Therefore the cross section depends strongly on the effective size of the nucleus and varies with $Z^2$ (Brydson, 2001), thus heavy atoms can be distinguished from light atoms as exploited by the HAADF-STEM method.

(b) Inelastic scattering events happen as a result of Coulomb interaction between a fast incident electron and the atomic electrons and is mostly incoherent. The fast electrons lose an equal amount of energy, as the total energy is conserved at each collision (Egerton, 2011). It is the analysis of this energy-loss which is the basis for EELS. The total cross section for inelastic scattering varies approximately linearly with Z (Brydson, 2001). Inelastic scattering events lead to four phenomena that occur when high energetic electrons interact with the specimen: (i) phonon excitation, (ii) plasmon excitation, (iii) single electron excitation or (iv) direct radiation loss (Brydson, 2001).

(i) Phonons, atomic vibrations in the solid, are excited by the primary beam the amount of energy-loss is less than 1 eV. Recent monochromators in combination with aberration corrected STEM instruments allow the local probing of phonon states. (e.g. Egoavil et al., 2014, Krivanek et al., 2013, 2014).

(ii) Plasmons are collective resonant oscillations of the valence electron density. The incident electron typically loses 5 to 30 eV by exciting a plasmon and the mean free path is in the order of 100 nm. This is the most frequent scattering process and therefore dominates the low-loss EEL spectra.

(iii) Single electron excitation signifies that the incident electron transfers some of its energy to a single electron in the specimen leading to ionization, leaving the atom in an excited state. If an incident electron ionizes an inner shell electron, the energy-loss is large

and characteristic for the specific atom (e.g. it takes 284 eV to ionize carbon K). The mean free path is quite large (μm) so it occurs less frequently than plasmon scattering, however this process is the basis for core-loss EELS.

(iv) Direct radiation losses, also referred to as bremsstrahlung, happen if incident electrons lose energy in solids due to the deceleration process in which energy is emitted directly in the form of phonons.

### 3.4.1 The EEL spectrum

The topography of an EEL spectrum (Fig. 26) is dominated by the zero-loss peak that originates from unscattered and elastically (i.e. vibrational- or phonon-) scattered electrons that hardly lose any energy traversing the sample. A measure of spectral resolution is the full width half-maximum (FHWM) of the zero-loss peak which usually is limited by the energy spread of the electron source.

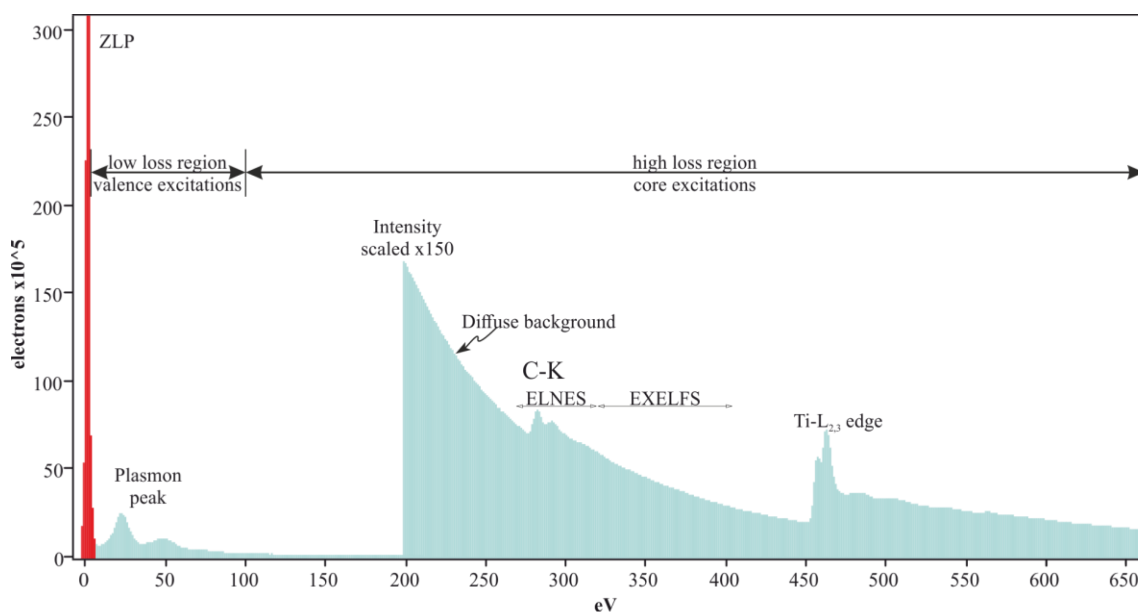


**Fig. 26** Most prominent features of an EEL spectrum.

The low-loss regime of the EEL spectrum extends from the zero-loss peak to about 50 eV. Features dominating the low-loss spectrum originate from plasmon oscillations of the valence electrons and valence - conduction band transitions. Multiple plasmon peaks are indicative for thick samples as the probability for multiple inelastic scattering especially for plasmon excitation rises. The high loss region is dominated by an exponentially decreasing background superposed by element specific edges. The edges can be split up into the energy-loss near edge structure (ELNES) and the extended energy-loss fine structure (EXELFS). The ELNES is displayed as small oscillations extending several tens

of eV beyond the ionization edge onset. It occurs when an ejected inner shell electron is excited into an unoccupied energy level above the Fermi level (unoccupied density of states) (Fig. 27). As the DOS pictures the electronic structure of an atom the ELNES can give information about the bonding and valence states (Egerton, 2011). Further, multiple scattering simulations can help to interpret experimental data (Moreno et al., 2007).
EXELFS can be observed more than 50 eV after the edge, continuing for several 100 eV. They can be seen in the spectrum by small intensity oscillations due to the interference of outgoing and reflected wave allowing to derive bonding length (Angelini et al., 1987; Sarikaya et al., 1996)

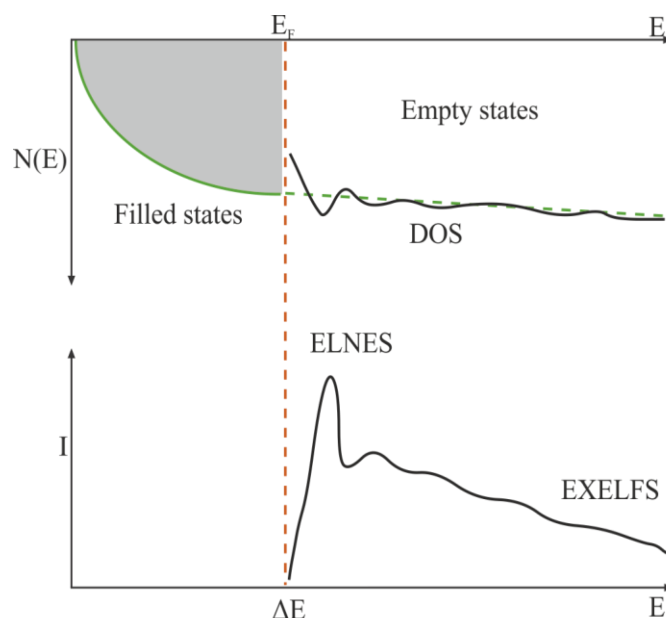


**Fig. 27** Relationship between the unoccupied DOS and the ELNES intensity in the ionization edge fine structure. Redrawn from Williams and Carter (2009).

### 3.4.2 EELS Quantification

Since the first measurement of the energy spectrum of transmitted electrons was reported by Ruthemann (1941) and Hillier & Baker (1944) constructed a first electron microanalyzer, lots of effort has been put into compositional quantitative results from EELS. First the conventional approach will be discussed by the means of a classical intensity extraction and gives a description of the quantification formulae.
Secondly the "Model based" approach (Thomas and Twesten, 2012) following the work of Verbeeck and Van Aert (2004) is described that paves the way for a better signal extraction. The last part of this section gives an overview of the different approaches to EELS cross sections that are used to turn spectral intensities into concentrations.

#### 3.4.2.1 Conventional approach

Accurate quantification requires a thin specimen less than 100 nm because thick specimen cause a redistribution of the EELS intensities. A common method for measuring the thickness is the log ratio method that gives a relative thickness by relating the zero-loss intensity to the total transmitted intensities by using Equation (3) (e.g. Joy et al., 1979). This equation represents the mean number of scattering events per incident electron following Poisson statistics.

$$t/\lambda = ln\left(I_t/I_0\right) \tag{3}$$

With $t$ being the specimen thickness, $\lambda$ being the total inelastic mean free path and $I_t$ and $I_0$ being the total area under the whole spectrum and the area under the zero-loss peak, respectively.

The total inelastic mean free path, $\lambda$, can be estimated by using Equation (4) proposed by Malis et al. (1988).

$$\lambda = \frac{106\left(1+\frac{E_0}{1022\,keV}\right)(E_0/E_m)}{\left(1+\frac{E_0}{511}keV\right)^2 ln(2\beta E_0 E_m)} \tag{4}$$

Where $E_m$=7.6$Z_{eff}^{0.36}$ and the effective atomic number ($Z_{eff}$) is given by Malis et al. (1988):

$$Z_{eff} \approx \frac{\Sigma_i f_i Z_i^{1.3}}{\Sigma_i f_i Z_i^{0.3}} \tag{5}$$

where $f_i$ is the atomic fraction of each element of atomic number $Z_i$.

For a thicker sample the probability for multiple scattering increases which can be removed by Fourier transform techniques like the Fourier ratio method (Egerton et al., 1985) after a previous background subtraction.

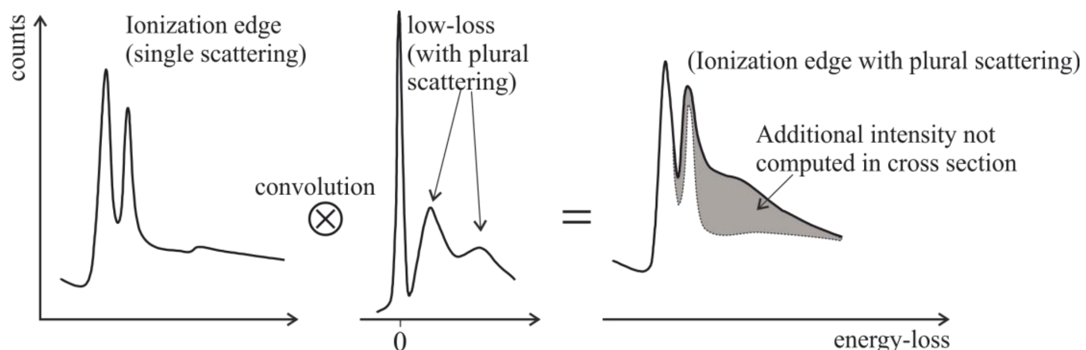


**Fig. 28** The effect of plural scattering is shown as a convolution of the edge shape and the low-loss spectrum. Redrawn from "Gatan Electron Microscopy School-EELS imaging and Analysis" (2013).

This plural scattering manifests in the spectrum by a convolution of the edge shape and the low-loss spectrum (Fig. 28).

Due to the large background contribution that arises from tails of plasmon excitations and preceding core-loss edges to the edge intensity, it is crucial to remove the background to obtain the pure edge signal intensity. The background integral can be estimated as shown in (Fig. 29) by fitting a pre-edge intensity over an energy range $\Gamma$ prior to the edge to a particular function of energy-loss E. Further a power law function $AE^{-r}$, with $A$ being a scaling constant and $r$ the slope exponent, is mostly used for extrapolating this function into the integration region (Egerton, 1982).

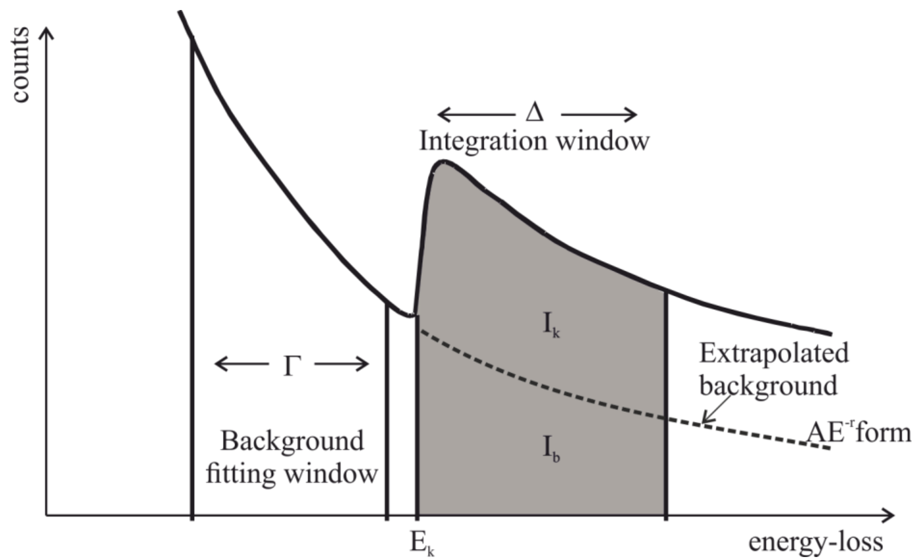


**Fig. 29** Schematic drawing of the background fit procedure along with a power law background extrapolation. Redrawn from Egerton (1982).

After a background subtraction and accounting for plural scattering with Fourier deconvolution techniques, one can integrate the spectrum over an integration window of a certain width to get the edge intensity most commonly starting at the edge threshold energy, i.e. steepest intensity increase (Kothleitner and Hofer, 1998).

Turning intensities into concentrations needs the knowledge of the scattering cross section $\sigma_k$, which is related to the probability ($P_k$) that a given incident beam electron will be detected as a count in a core-edge $k$ of a specific element. $P_k$ is directly proportional to the projected (areal) density of atoms of that element ($N$) (Egerton, 1978):

$$\boldsymbol{P_k = N\sigma_k} \quad (6)$$

Where $P_k$ is given by the intensity values of the EELS spectrum:

$$\boldsymbol{P_k = {}^{I_k}/_{I_t}} \quad (7)$$

Where $I_k$ and $I_t$ represent the edge count integral and the total number of counts in the spectrum, respectively. From these equations it becomes clear that the areal density can be written as:

$$N = {I_k}/{I_t \sigma_k} \tag{8}$$

The use of $I_t$ would only apply to true single scattering which is not the case most of the times further due to the SEA not the whole angular range of energy-loss electrons is recorded as well as we integrate over $\Delta$, giving us the partial ionization cross section, so we have to rewrite Equation (8)

$$N_k = \frac{I_k(\beta, \Delta)}{I_0(\beta)\sigma_k(\beta, \Delta)} \left[{at}/{nm^2}\right] \tag{9}$$

For an elemental ratio of two elements $A$ and $B$ the low-loss intensity ($I_0$) drops out giving:

$$\frac{N_A}{N_B} = \frac{I_A(\beta, \Delta)\sigma_B(\beta, \Delta)}{I_B(\beta, \Delta)\sigma_A(\beta, \Delta)} \tag{10}$$

As we have extracted the intensities of the ionization edges of interest, we now have to determine the cross sections for these elements which can be either done experimentally using thin film standards or making certain approximations and employing computer programs.

The use of thin film standards requires the knowledge of the thickness, density and composition of the sample which are hard to access, further, systematic errors may be introduced by oxidation layers (e.g. Hofer, 1991; Joy et al., 1979).

The widest used methods calculate inner shell ionization cross sections by atomic models (hydrogenic or Hartree-Slater) that are also integrated into e.g. GATAN's Digital Micrograph (DM) software. Furthermore cross sections and ELNES can also be simulated using multiple scattering (MS) (e.g. Ankudinov and Ravel, 1998; Moreno et al., 2007; Rehr et al., 2010)or density functional theory (DFT) (Blaha et al., 1990; Hébert, 2007; Kohn and Sham, 1965) calculations.

When considering quantification, one has to be aware of the experimental conditions.

Especially the knowledge of the convergence and collection angle are important. The convergence semi-angle ($\alpha$) is determined by the $C_2$ aperture, while the collection semi-angle ($\beta$) is determined by the objective aperture in TEM mode and by the size of the spectrometer entrance aperture (SEA) and the camera length (CL) in STEM mode.

Quantification formulae (Equations 9 and 10), making use of edge intensities and cross sections, are written as a function of the primary energy ($E_0$), $\alpha$, $\beta$ and the integration

window ($\Delta$) assuming that all the intensity is collected by the spectrometer which is not the case.

That means that if $\alpha$ is small some electrons that are scattered by more than $\beta$ are excluded from entering the SEA (Fig. 30 (a)); if $\alpha$ gets bigger some electrons that are scattered by more than $\beta$ still enter the SEA (Fig. 30 (b)) contributing to the spectrum's intensity.

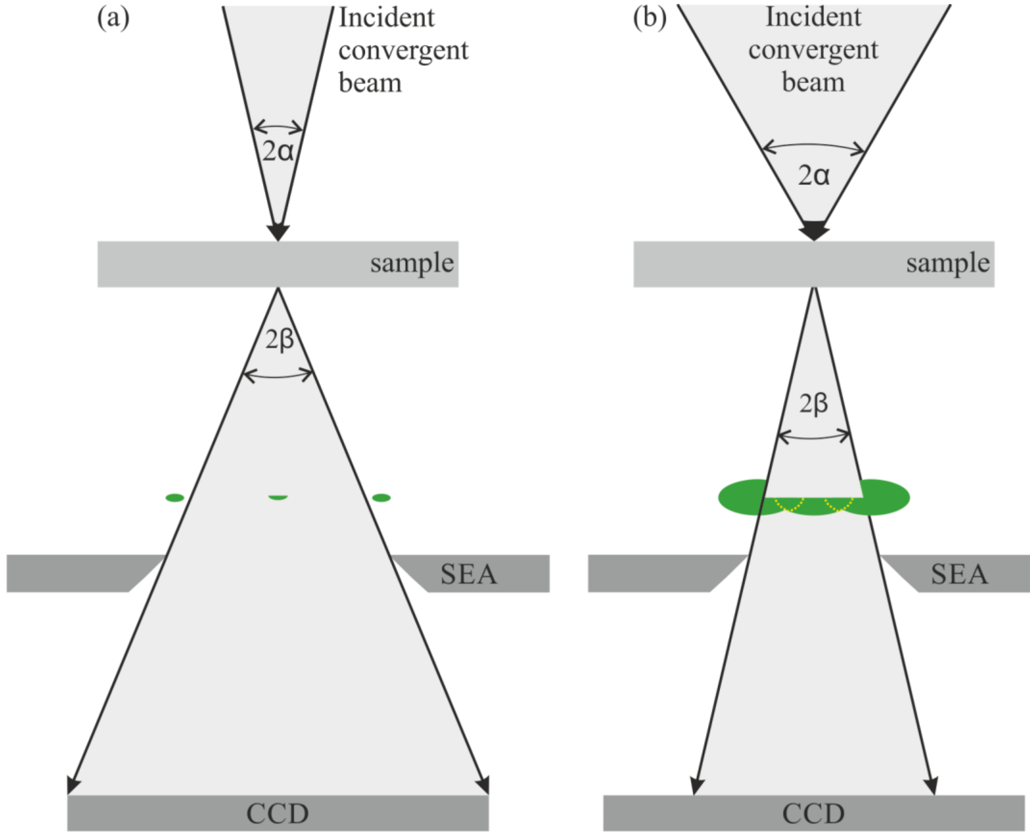


**Fig. 30** Consequence of beam convergence on the core-loss intensity.

Therefore it is suggested (Scheinfein and Isaacson, 1984) to account for incident beam convergence correction calculating a correction factor $F_1$ for $\alpha \leq \beta$:

$$F_1 = \frac{I_k(\alpha, \beta, \Delta)}{I_k(0, \beta, \Delta)} = \frac{2/a^2}{ln\,[1 + (\beta/\theta_E)^2]} \int_0^\beta ln \left[ \frac{\psi^2 + (\psi^4 + 4\theta^2\theta_E^2)^{1/2}}{2\theta_E^2} \right] \theta d\theta \qquad (11)$$

Where $\theta_E \approx E/(2E_0)$ is the characteristic angle of inelastic scattering, $\theta$ is the angle of scattering and $\psi$ is the angle between planes (normal to the surface) that contain the incident and scattered electron wave vectors. As $F1$ depends on $\theta_E$, the convergence correction is different for all core-loss edges.

Therefore the elemental quantification ratio from equation 10 can be corrected as shown in equation 12.

$$\frac{N_A}{N_B} = \frac{I_A(\beta,\Delta)\sigma_B(\beta,\Delta)F_{1,B}}{I_B(\beta,\Delta)\sigma_A(\beta,\Delta)F_{1,A}} \tag{12}$$

In the case of absolute quantification in equation 9, the convergence correction for low- and high-losses are different. Thererfore another correction factor, $F_2$, is introduced:

$$F_2 \approx \begin{cases} F_1 & for\ \alpha \leq \beta \\ (\alpha/\beta)^2 F_1 & for\ \alpha \geq \beta \end{cases} \tag{13}$$

Equation 9 can, therefore, be expressed as:

$$N_k = \frac{I_k(\beta,\Delta)}{I_0(\beta)\sigma_k(\beta,\Delta)F_2}\left[{}^{at}/_{nm^2}\right] \tag{14}$$

*F1* and *F2* can be evaluated with Egerton's (2011) CONCOR2 program that uses the analytical expression of the integral in Equation (11). All MATLAB programs published in Egerton (2011) are public-domain software and can be downloaded from: https://sites.google.com/site/temsemeels/home/matlab-programs-from-eels-in-the-electron-microscope-3rd-edition.

Alternatively, the CONCOR2 program accounts for incident beam convergence by calculating an effective collection angle (β*) that differs from the collection angle (β) by an amount dependent on the convergence angle (α) as well as the edge energy.

As shown in Fig. 31 for small convergence angles the slope is roughly 1, where β deviates from β* with a mean below 3%. When using typical STEM convergence angles β* is much higher for a small β until the collection angle is similar to the convergence angle. For high collection angles the convergence becomes smaller again.

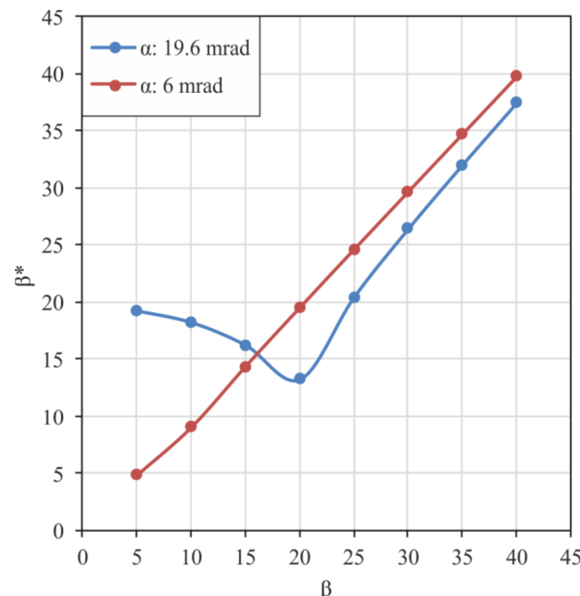


**Fig. 31** β plotted against β* for Carbon-K at 300 kV

### 3.4.2.2 “Model based” approaches

The conventional approach can be described as a three-step process which involves background removal, multiple scattering removal and finally the concentration determination. The choice of the fitting region and the energy integration region is strongly user dependent. Therefore, a strong interest exists to overcome these “uncertainty factors” and to fit a numerical model to experimental spectra. For more than 30 years these parameters are part of debate. Pun et al., (1985) tried to introduce a weighted least squares estimation procedure for estimating the parameters of the background law. Manoubi et al., (1990), presented a new approach in quantitative elemental analysis by EELS using a curve-fitting method, which produces better results to those obtained by conventional analysis, when analyzing overlapping edges. Verbeeck (2002), describes in his PhD thesis the idea behind the “EELSMODEL” software making use of statistical methods, like the maximum likelihood (ML) method (also read: Verbeeck et al., 2006; Verbeeck and Van Aert, 2004).
Within this thesis the quantification routine described by Thomas & Twesten (2012) was applied as is incorporated into modern analysis programs (GATAN’s DigitalMicrograph 3.23). The big advantage of this method is, that it does not use a conventional background extrapolation described above that relies on a pre-edge fitting window. Instead the whole spectrum gets split up in subgroups each consisting of the edge of interest and any successive overlapping edges. These subgroups are modeled separately on the basis of a decomposition combining the experimental ELNES and theoretical models of cross section, superposed over a multiple linear least squares (MLLS) fitting of a single computed background of a certain energy range. The MLLS method fits the total spectral intensity *J(E)* to an expression in the form of:

$$\boldsymbol{F}(\boldsymbol{E}) = \boldsymbol{A}\boldsymbol{E}^{-r} + \boldsymbol{\Sigma}_{\boldsymbol{n}}\boldsymbol{B}_{\boldsymbol{n}}\boldsymbol{S}_{\boldsymbol{n}}(\boldsymbol{E}) \tag{15}$$

Where the first term represents a background prior to the edge of the lowest energy-loss, and the $S_n(E)$ terms represent the core-loss modelled spectra of the elements of interest (Egerton, 2011). The fitting coefficients $B_n$ can be found by minimizing the $(J_i - F_i)^2$ term in Equation 16.
$\chi^2$ describes how well the model fits the observations and summarizes the discrepancy between observed and the expected values given by

$$\chi^2 = \sum_i [\frac{\boldsymbol{J}_i - \boldsymbol{F}_i}{\boldsymbol{\sigma}_i}]^2 \tag{16}$$

with $i$ being the index of a channel within the fitting region and $\sigma_i$ being the standard deviation of the intensity in that channel (Egerton, 2011).

Via simultaneous acquisition of both low-loss (LL) and core-loss (CL) spectra, referred to as DualEELS mode (Gubbens et al., 2010), multiple scattering can be additionally removed from the EEL spectrum as it is treated not by deconvolution of the extracted signal but by forward convolution of the model cross section before the model is fitted to the data.

These features allow to account for overlapping edges, therefore, edge intensities can be extracted with a higher accuracy than using conventional approaches.

#### 3.4.2.3 EELS Intensity extraction model based approach

Using GATAN's DM 3.23 the user can open the desired core-loss spectrum and define the edges of interest using the Elemental Quantification tab. The button EELS Edge Setup (Fig. 32, red circle) opens up a window to enter the key parameters for quantification for each of the selected edges (Fig. 33, left column). Fig. 32 (green circle) shows the signal setup as it is adjusted (Fig. 33, right column).

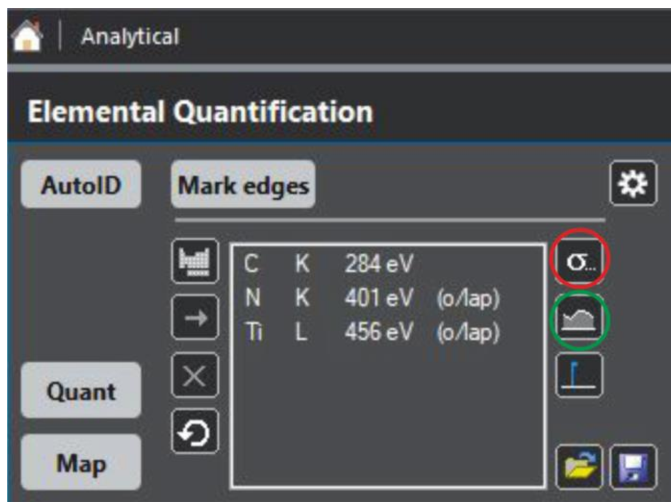


**Fig. 32** Analytical toolbox in DM 3.23

Edge setup parameters are modified as shown in Fig. 33 (left column):

At first the background model has to be specified, normally a power law- background fits well. The fit range defines the array for which the background should be drawn (1).

The signal sum width is the width of the signal integration region. If Model ELNES is enabled, this will be from the end of the exclude ELNES region to the fit region end. This signal region is shown on the active spectrum as a solid colored region (2).

By ticking the Model ELNES Section the user allows the model to start after a predetermined ELNES region as the ELNES is not well computed by the cross section models. Also, the iterations for this process can be defined to get accurate results (3).

The theoretical cross section model along with the chemical shift of the edge can also be defined (4).

Last but not least plural scattering can be included in the model by selecting the corresponding low-loss spectrum (5).

The advantage of this method is, that the user can immediately see how well the parameters fit the model to the original spectrum, as it dynamically updates while simultaneously adjusting the fit region on the spectrum.

The final step for Intensity extraction is to subtract the background model from, in this case, the C-edge, the C-model from the N-K edge and the N-model from the Ti-L edge.

This leads to the net intensities even when edges overlap as in the case of N-K.

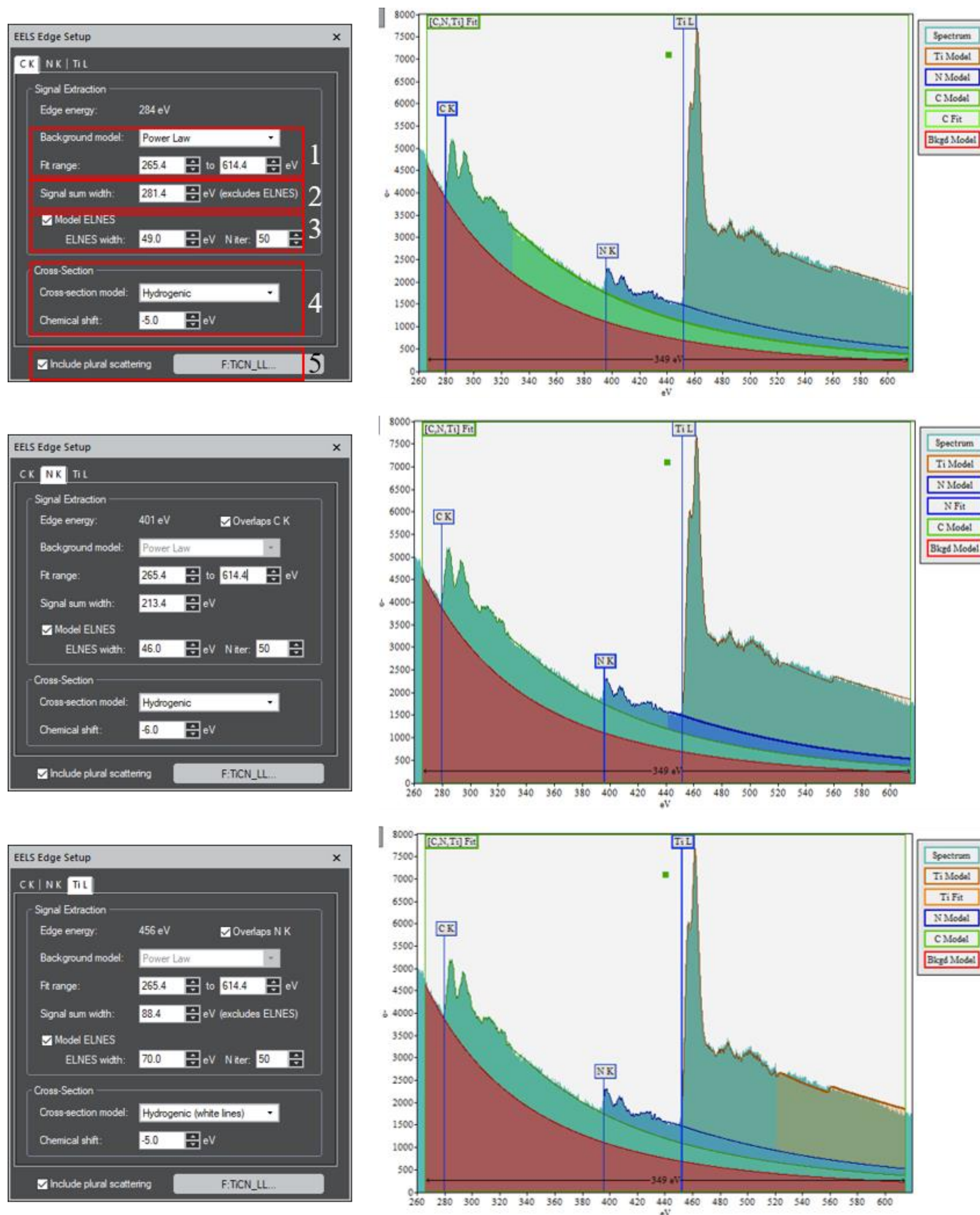


**Fig. 33** EELS Edge Setup in DM 3.23. Numbers are described in the text.

### 3.4.2.4 Comparison of intensity extraction using 2 different approaches

The conventional approach relies on a pre-edge background window fitting only. This means that overlapping edges cannot be taken into account.

One must be aware that small changes in the background window position or width imply significant effects on the background model. This problem can be overcome by increasing the size of the window. To account for plural scattering the spectrum can be deconvolved with the Low-loss Spectrum to get out the net Intensities shown in Fig. 34.

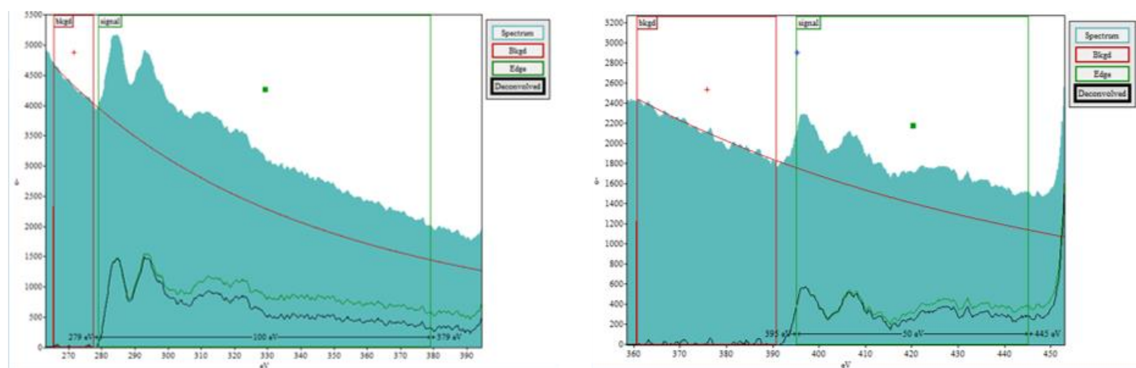


**Fig. 34** Conventional EELS intensity extraction for C-K (left) and N-K (right).

For comparison the background subtracted and deconvolved spectra are compared to the modelled intensities in Fig. 35.

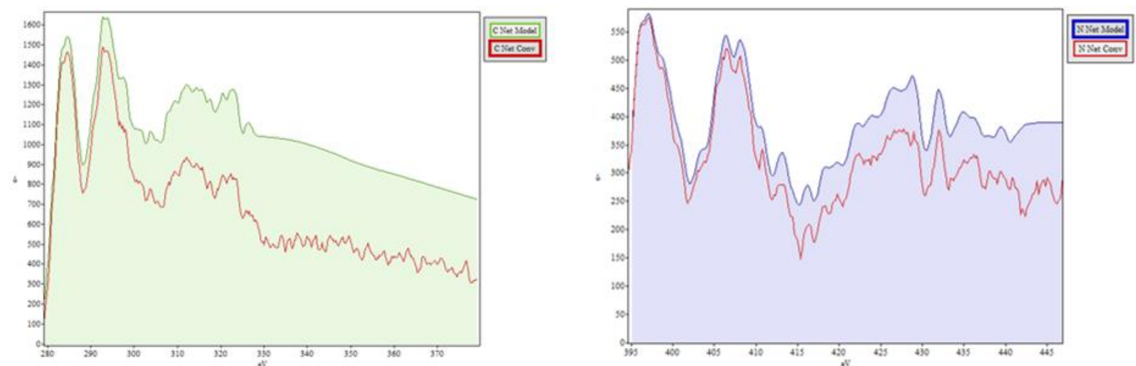

**Fig. 35** Model based vs. conventional EELS intensities extraction for C-K (left) and N-K (right).

By taking the integrated intensities over a signal window width of 50 eV beginning at the threshold energy, the difference between the approaches is 24% and 15% for the C-K and N-K edge, respectively. Taking a signal window with a width of 100 eV for the C-K edge, the difference is 35%.

### 3.4.3 Theory behind EELS cross sections

The fundamental principles of the EELS cross sections are based on the physics of inelastic scattering. After scattering the wavevector of the incident electron wave, $k_0$ will have changed to $k_f$ (Fig. 36).

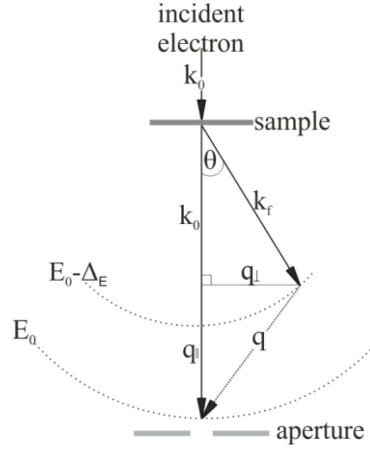


**Fig. 36** Wavevector diagram for inelastic scattering. The decomposition of the momentum transfer into components parallel and perpendicular to the incident electron are also shown. Redrawn from Brydson, 2001.

Experimental-wise the range of incident wave vectors is termed the convergence semi-angle α, while the range of wavevectors collected in the EELS signal will depend on the collection semi-angle, $\beta$ (Fig. 30). This represents a change in both direction and magnitude, while the momentum, $q$ is transferred to the sample (Brydson, 2001). The conservation of momentum and energy results in

$$\boldsymbol{q^2 = k_0^2(\theta^2 + \theta_E^2)} \tag{17}$$

where $\theta$ being the scattering semi-angle and $\theta_E$ being the characteristic scattering angle corresponding to the mean energy defined as

$$\boldsymbol{\theta_E = \frac{E}{\gamma m_0 v^2} = \frac{E}{(E_0 + m_0 c^2)(v/c)^2}} \tag{18}$$

where $v$ is the speed of the incident electron. $\gamma = 1+E_0/(m_0c^2)$ is the relativistic factor and $m_0$ represents the electron mass (Egerton, 2011).

An experimental EEL spectrum is related to the total inelastic cross section for scattering, $\sigma$, or more precisely, how it is dependent on the energy-loss, $E$, as well as solid scattering angle, $\Omega$, known as the double differential cross section, $d^2\,\sigma(dEd\Omega)$. This quantity represents the fraction of incident electrons ($E_0$) which are scattered into a solid angle $d\Omega$ $(\approx 2\pi \sin\theta\, d\theta)$ with an energy between $E_0$ and $E_0$-$\Delta_E$ (Brydson, 2001).

The double differential cross section can be written in the form of

$$\frac{d^2\sigma}{dEd\Omega} = \frac{4\gamma^2 R}{Eq^2}\frac{k_f}{k_0}\frac{df}{dE} \tag{19}$$

where $R = 13.6\ eV$, the Rydberg energy, and $df/dE$ is the generalized oscillator strength describing the response of an atom when a certain momentum and energy are imposed through collision of a fast electron. When the energy-loss $E$ is much smaller than the incident energy $E_0$, $k_f/k_0$ becomes close to 1.

Using Equation (17), Equation (19) can be expressed in terms of the solid angle $\Omega$.

$$\frac{d^2\sigma}{dEd\Omega} = \frac{4\gamma^2 R}{Ek_0^2}\left(\frac{1}{\theta^2 + \theta_E^2}\right)\frac{df}{dE} \tag{20}$$

For low scattering angles, the main angular dependence in Equation (20) derives from the Lorentzian factor $(\theta^2 + \theta_E^2)^{-1}$. The characteristic angle, $\theta_E$, is important as it represents the half-width at half maximum (HWHM) of this Lorentzian function (Egerton, 2011).

#### 3.4.3.1 Atomistic calculations

The two types of atomistic calculations, the hydrogenic approximation and the Hartree-Slater model are described in the following section.

##### The Hydrogenic Approximation

Egerton (1979) first proposed to calculate the generalized oscillator strengths for K-shell ionization with a hydrogenic model modified with a Zener (1930) screening constant (s) of 0.3.

The cross sections are modeled with no outer-shell electrons by approximating the atom of interest to an isolated hydrogen atom. The atom of interest has a charge on the nucleus equal to the atomic number Z of the atom. This simple approach can be made due to the availability of analytical expressions for the wavefunctions of the hydrogen atom, which were obtained by solving the Schrödinger equation, see Equation (21).

$$\left(\frac{-\hbar^2}{2m_0}\right)\nabla^2\psi - \left(\frac{e^2}{4\pi\varepsilon_0 r}\right)\psi = E_t\psi \tag{21}$$

Where $E_t$ stands for the kinetic and electrostatic energy of the electron i.e. the net energy. The electrostatic term must be modified to take into account the screening of the outer shell electrons. According to Slater (1930) an effective nuclear charge ($Z_s$=Z-s) should modify the elementary charge in Equation (22) and the observed threshold energy for inner-shell ionization is:

$$E_k = Z_s^2 R - E_s \tag{22}$$

This is due to the assumption that outer-shell electrons (with principal quantum number higher than that of the initial-state wavefunction) form a spherical shell reducing the inner-shell binding energy by an amount $E_s$, (Egerton, 2011, 1979). This leads to the modified Schrödinger Equation:

$$\left(\frac{-\hbar^2}{2m_0}\right)\nabla^2\psi - \left(\frac{Z_s e^2}{4\pi\varepsilon_0 r}\right)\psi + E_s\psi = E_t\psi \tag{23}$$

By substituting Equations (22) and (23) into Equation (24)

$$E_t = E - E_k \tag{24}$$

where the net energy ($E_t$) of the excited electron is related to the binding energy ($E_k$) and the energy ($E$) lost by the transmitted electron one obtains the Schrödinger Equation (25) for a "hydrogenic equivalent" atom with nuclear charge $Z_s$e and no outer shells:

$$\left(\frac{-\hbar^2}{2m_0}\right)\nabla^2\psi - \left(\frac{Z_s e^2}{4\pi\varepsilon_0 r}\right)\psi = (E - Z_s^2 R)\psi \tag{25}$$

The nucleus is screened by the second 1 s electron, in the case of K-shell excitation, thus reducing the effective charge to $Z_s = Z - 0.3$ (Egerton, 1979; Zener, 1930).
K-shell ionization cross sections can be calculated using Egerton's (2011) SIGMAK program which in its newest version SIGMAK3 uses a default value of s=0.5. Egerton (2011) also made allowance for calculating L-shell ionization cross sections with the program SIGMAL3 which uses an effective nuclear charge of $Z_s = Z - (2 \times 0.85) - (7 \times 0.35)$, allowing for the screening effect of the two K-shells and seven remaining L-shell electrons.

### The Hartree-Slater model

A more complex method which calculates the cross section in a more realistic way than the SIGMAK or SIGMAL hydrogenic models is the Hartree-Slater model (e.g. Ahn and Rez, 1985; Leapman et al., 1980; Rez, 1982) which is available in the DM software, GATAN Inc.
For most atoms accurate wavefunctions have been computed by iterative solution of the Schrödinger equation using a self-consistent atomic potential. A simplification of the Hartree–Fock (HF) procedure is the Hartree–Slater (HS or HFS) method which assumes a central (spherically symmetric) field within the atom. The Hartree–Slater model properly accounts for the screening, providing a good prediction of the edge shape in

many elements with restrictions to $L_{2,3}$-edges of transition metals because calculations usually deal only with ionizing transitions to the continuum and do not account for excitation to unoccupied bound states (Hofer, 1991; Egerton 2011).

#### 3.4.3.2 Experimental EELS cross sections

Experimental EELS cross sections can be obtained using single element standards or using the k-factor method as described below.

The use of single element standards requires precise knowledge of the sample's mass-thickness, as inner-shell ionization cross section σ can be written as the core-loss-intensity $I^E$ normalized by the corresponding low-loss integral $I_0^E$ times the mass-thickness multiplied by the ratio of the atomic weight $AW$ and Avogadro's number $N_{AV}$:

$$\boldsymbol{\sigma} = \frac{\boldsymbol{I^E}}{\boldsymbol{I_0^E \rho t}} \frac{\boldsymbol{AW}}{\boldsymbol{N_{AV}}} \tag{26}$$

According to Joy et al. (1979) this method is generally applicable and can be used for a variety of elements. However absolute thickness determination is a very time consuming process and was proposed by using the Convergent-Beam Diffraction Pattern Technique (Kelly et al., 1975).

Crozier (1990) published absolute cross sections for 5 elements prepared as thin evaporated films accessing the thickness by weighting the substrate before and after evaporation. Optical densitometry verified that the film thickness varied by no more than 5% over the entire substrate area.

Kothleitner et al. (2014) follows a different approach as the inelastic mean free path (IMFP) gets accessed by a symmetric shaped rod of known thickness. As due to Equation 3 the absolute thickness of a FIB lamella of same composition, using the same microscope parameters can be determined. Using Equation 26 the cross section can be calculated. Possible deviations from the perfect symmetry of the rod can be controlledresin

by observing the resin embedded, cross sectioned rod after the measurement.

Craven et al. (2016) takes a similar approach, however the symmetricity of the rod is checked via two orthogonal tilted HAADF images. The inelastic mean free path of a TiC phase was determined experimentally while it was scaled for other Carbides and Nitrides using the parametrization by Iakoubovskii et al. (2008), giving meaningful results when compared to Hartree-Slater cross sections well above the edge threshold.

The k-factor method was introduced by (Ferdinand Hofer, 1987) in order to overcome the difficulties of thickness determination. In this method, a material, which must contain one light element (B) which gives a K-edge and the element (A) for the desired cross section is used.
In analogy to EDX k-factors, the cross section ratio can be determined using the following Equation:

$$\frac{\boldsymbol{\sigma_B}(\boldsymbol{\beta},\Delta)}{\boldsymbol{\sigma_A}(\boldsymbol{\beta},\Delta)}=\frac{\boldsymbol{I_B}(\boldsymbol{\beta},\Delta)}{\boldsymbol{I_A}(\boldsymbol{\beta},\Delta)}\frac{\boldsymbol{I_A}}{\boldsymbol{I_B}}=\boldsymbol{k_{AB}} \tag{27}$$

As K-edges of light elements can be accurately calculated, absolute cross section values can be determined by using a light element's calculated cross section value.

Experimental ratios of the inner-shell ionization cross section were published by a variety of authors over the past decades:

Experimental ratios for K, L, M and N shells have been determined for a significant number of elements (Crozier et al., 1987; Hofer, 1987; Hofer et al., 1988; Hofer and Golob, 1988; Hofer, 1989; Hofer, 1991; Hofer and Kothleitner, 1993; Hofer and Kothleitner, 1996; Harkins et al., 2008; Kuimalee et al., 2010).
Further, K, L and M shell ratios from transition-metal compounds have been measured (Grande and Ahn, 1983; Malis and Titchmarsh, 1985; Bach et al., 2009).

Manoubi et al. (1990) measured $M_{45}$ edges in rare earth oxides.

#### 3.4.3.3 Cross section simulations by multiple scattering theory

The FEFF code was initially written for simulating X-ray absorption spectra (XAS) by John Rehr's group at the department of physics at the University of Washington (Rehr et al., 2009). Now commercially available in version 9 (http://feff.phys.washington.edu/) FEFF also allows for the simulation of EEL spectra. XAS and EELS, apart from relativistic effects, are essentially identical, both exhibiting near-edge structure and extended fine structure (Jorissen and Rehr, 2010). Ab initio simulations are useful to interpret experimental data. The FEFF code is an ab initio and largely parameter-free implementation of real-space multiple scattering (RSMS) theory based on the real-space Green's function (RSGF), carried out with a finite cluster of atoms (Rehr et al., 2010). In the multiple scattering (MS) theory, the excited electron in its final state is considered as a wave scattering off the atoms in the sample (Fig. 37).

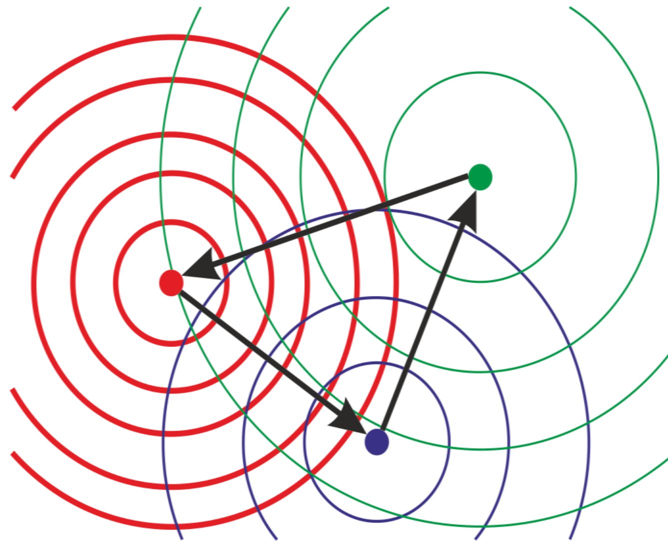

**Fig. 37** Sketch of the multiple scattering triangular path of an outgoing wave by neighboring atoms. The red atom is the original source of the wave, which diffracts first off the blue atom and finally off the green atom. Each successive outgoing spherical wave is weakened, which is reflected in the thickness of the spherical wave fronts. Redrawn from Rehr et al. (2000).

It can be described either in real space (RSMS), making the method applicable to arbitrary, non-periodic systems, or in reciprocal space by applying e.g. Kohn-Korringa-Rostoker (KKR) theory (Rehr, 2000).

The program reads a single input file termed "feff.inp" that tells FEFF how to proceed with the calculation. The input file can be conveniently created by the ATOMS program (Ravel, 2001). The ATOMS program however, requires a crystallographic information file (cif) displaying the crystal structure that can be either generated by structure solution programs or downloaded from databases (e.g. Inorganic Crystal Structure Database – ICSD: https://icsd.fiz-karlsruhe.de/search/basic.xhtml). Fractional occupancies of atomic positions cannot be directly handled by FEFF (Moreno et al., 2007).

Within the EELS options window, one can specify the incident beam energy as well as the collection and convergence angles.

By default, FEFF9 approximates spherically averaged muffin-tin (MT) potentials, centered on each atom, to the total electronic potential for the initial and final states. The potential, in this case, has a constant value in the interstitial region between the spheres.

The program allows to calculate the potential, Fermi level (EF) and charge transfer self consistently (Ankudinov and Ravel, 1998). Self-consistent field (SCF) potentials allow a more accurate calculation of the near-edge. The SCF procedure in FEFF9 typically iterates the Coulomb potentials, electron densities, and the Fermi energy 10-20 times

(Rehr et al., 2010). Additionally, experimental broadening, the presence of a core hole and the Debye temperature can be added to the calculations.
After calculating the spectrum FEFF creates an “eels.dat” file that contains the EEL spectrum: energy-loss in eV, total spectrum, contribution from each component of the cross section tensor.
The calculations permit a quantitative interpretation of EEL spectra and hence give energy differential cross sections as well as the ELNES that should match the crystal structure.

##### 3.4.3.3.1 Performing ELNES simulations based on a *.cif file

Although promised by the developers of the FEFF code, the newest version FEFF9 is not capable of directly reading *.cif files. So starting the simulations involves creating a feff.inp file. The program of choice is named ATOMS (Ravel, 2001). The free software package DEMETER can be downloaded from https://bruceravel.github.io/demeter/. This package includes three programs: ARTHENA, ARTEMIS and HEPHAESTUS. By using the ARTEMIS program, the user can choose the “Feff calculations” option and by pressing the “Add” button a *.cif file is created. This file will be opened in a separate program called ATOMS. By simply pressing the “Export” button the user can selcet to save it as a feff.inp file. One has to be aware that FEFF creates multiple files during calculation, therefore each feff.inp file should be stored in a separate folder.
Using the JFEFF GUI, the user can specify the feff.inp file created before then save the settings and run the simulation. The numbers within Fig. 38 explain the necessary steps to perform an ELNES simulation:
After the input file is loaded the user has to decide what kind of spectral data is to be obtained. In our case the “ELNES option” (1) was selected. The “other options” button (2) opens the “EELS Options” window (3). Here the experimental conditions like primary energy, collection and convergence angle can be specified. Further, a defined orientation can be selected (kx,ky,kz). By unhooking this option direction averaged spectra are calculated. The desired edge-type has to be chosen (4). Full multiple scattering (FMS) is done for a cluster of atoms around the ionized atom using the full multiple scattering radius input filed (rfms), with 6Å seems to be an appropriate value (5).
Specifying the potentials, the standard options are given by the SCF module (6). It is used for automated self-consistent potential calculations. 4 values can be assigned: (7)

specifies the radius of the cluster for full multiple scattering during the self-consistency loop, with 4.5Å seems to be an appropriate value. (8) The default value 0 is appropriate for solids. (9) This is the maximum number of iterations the potential will be recalculated. Usually self-consistency is reached in about 10 iterations. (10) The convergence accelerator factor has a typical value of 0.2. (11) It's suggested to use values between 1 and 30. A value outside of this range will be ignored and replaced with an acceptable value. The "corehole" option (12) allows to choose either a Final State Rule corehole, an "RPA corehole" or "No corehole". The "general" card (13) allows to choose an energy grid (14) e.g. starting at the threshold energy for 200 eV with a dispersion of 0.25 eV. Using the "cross sections" card (15), corrections for instrumental broadening (16) can be addressed by using the FWHM of the zero-loss peak e.g. 1.5 eV.
Finally, the spectrum can be simulated (17) and an eels.dat file is created containing the ELNES coordinates. Note: the ELNES coordinates are saved as $a_0^2/eV$ and have to be converted to barn/eV.

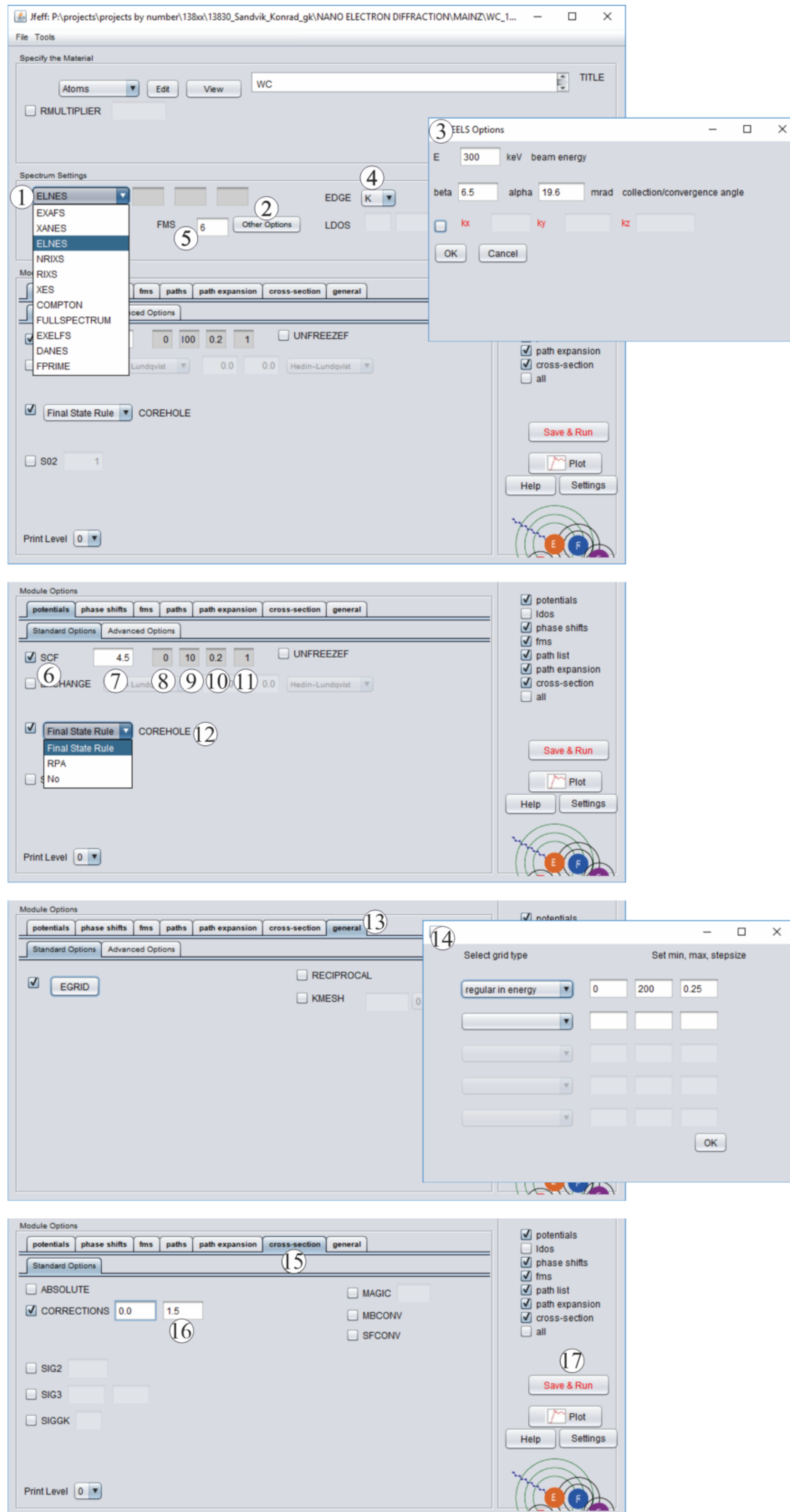

**Fig. 38** Parameters that have to be selected for FEFF ELNES simulations. Numbers are described in the text.

#### 3.4.3.4 Summary

The conventional approach deals with a spectrum in which the background for each element of interest is subtracted using a background window prior to the edge assuming a power law behavior for background fitting. When necessary one has to account for plural scattering by Fourier deconvolution methods. The edge intensity is integrated over an energy window of a certain width that normally starts at the edge's threshold energy. Turning intensities into concentrations, i.e. get the areal density, one has to know the partial cross section for the element of interest under the experimental conditions used. One can either employ atomistic approximations as the hydrogenic or the Hartree-Slater model or one can perform cross section simulations. As the approximations do not show any ELNES features cross sections often lead to erroneous results. FEFF simulated cross sections also simulate the ELNES giving more accurate results. The deficiency of the conventional approach however is, that in the case of overlapping edges the edge intensity is distorted as every subsequent edge lies not only on a background but also on the tails of any prior edge.

## 3.5 Energy Dispersive X-ray Spectroscopy (EDXS)

Additionally to EELS, EDXS is another technique used for elemental analysis or chemical characterization (Garrett-Reed and Bell, 2002). X-ray generation is related to the ionization of the target atom by fast electron bombardment, hence, an electron vacancy is produced in one of the inner shells, subsequently filled up by outer-shell electrons.

For light elements ($Z<10$) the probability of X-ray emission is weaker, dominated by Auger electron emission. As the latter are largely absorbed within the sample the signal leaving the sample surface would be weak and therefore is not regularly used in TEM experiments. The probability of X-ray photon emission is given by the fluorescent yield. The energy for X-ray photon emission depends on the corresponding electronic shells and is characteristic for each element.

Besides characteristic X-rays also Bremsstrahlung contributes to the X-ray spectrum originating from deceleration of fast electrons in the Coulomb field of the nucleus.

For detection, the generated X-ray quantum hits a semiconductor detector and generating electron-hole pairs that are proportional to the energy of the incident X-ray quantum. A

field effect transistor coupled to the detector generates an electrical output signal so the sum of all processes can be converted into an X-ray spectrum (Brydson, 2011).
The energy resolution is a detector property, described by the Fano Factor (Zulliger and Aitken, 1970). The energy resolution of a detector is often given at the Mn Kα line at 5.9 keV.
The main advantages of EDXS are, that even for thick samples, spectra can be acquired over a large energy range (up to 40 keV), thus making it also suitable for heavier elements, with a high signal-to-background ratio.
Spectra however, can be distorted by various effects like incomplete charge collection, escape-and sum peaks and energy dependent absorption effects within the sample and the holder (Gauvin, 2012; Kraxner et al., 2017), thus limiting the application on light elements. Additionally, in the low energy region a high background is observed originating from the Bremsstrahlung, that according to Kramers (1923) increases with decreasing energy.
One has also to bear in mind that channeling conditions have an effect on the X-ray intensity, thus off-axis conditions should be sought (Kothleitner et al., 2014).

### 3.5.1 Quantitative EDX analysis

Like EELS elemental quantification the characteristic line intensities have to be extracted to convert these into a chemical composition of the irradiated sample volume. Therefore, the background has to be extracted. There are mainly two approaches that are part of many currently available EDX software packages: on the one hand this is model fitting, on the other hand this is filtering. Modelling based on Kramers (1923) expressions deals with fitting an appropriate background model between the characteristic peaks. This model is then subtracted from the whole spectrum to gain intensities of the characteristic peaks. As this approach is difficult to apply to the low energy region below 1.5 keV, the filter approach would lead more consistent peak intensities as it is related to pure mathematics. It is based on the rapid variation of counts of the characteristic peaks as a function of energy (i.e. large $dI/dE$), while the $dI/dE$ of the BG is relatively small, which is also valid for spectral regions with strong absorption (e.g. <1 keV) (Williams and Carter, 2009). Digital filtering is implemented by convoluting a X-ray spectrum with a top-hat shaped, weighting function (Zaluzec, 1989). This corresponds to the second derivative of this spectrum, i.e. $d^2I/dE^2$ versus E. Presumably DM fits the second

derivative of Gaussian peaks to the filtered spectrum and uses the fitting parameters ($N$ and $\sigma$) to calculate the area of the corresponding Gaussian curves:

$$I = N\sigma\sqrt{2\pi} \tag{28}$$

It is suggested to use the top-hat approach for multi-element samples and in energy regions below ~1.5 keV, further the user induced influence on the gained characteristic intensity cancels out.
After background removal and extraction of the characteristic peak intensities there exist two dominant quantification methods such as the k-factor method and the ζ-factor method.

#### 3.5.1.1 The k-factor method

Castaing (1951) stated that the concentration of a present element is proportional to the intensity of the observed characteristic X-ray signal introducing $K$ as a sensitivity factor, $C$ denotes the concentration and $I^X$ the intensity of $i$ the specimen and $(i)$ a standard:

$$\frac{C_i}{C_{(i)}} = K\frac{I_i^X}{I_{(i)}^X} \tag{29}$$

The $k_{AB}$ factor method was introduced by Cliff and Lorimer (1975) demonstrating that a standard is not needed if intensities for two elements are gathered simultaneously and compared. The $k_{AB}$ factor or Cliff-Lorimer factor is a sensitivity factor that relates the weight percent of the studied elements ($C_A$, $C_B$) to the measured Intensities ($I_A^X$, $I_B^X$).

$$\frac{C_A}{C_B} = k_{AB}\frac{I_A^X}{I_B^X} \tag{30}$$

This only holds when the thin-film criterion is fulfilled, that means that $k_{AB}$ is only a function of Z and absorption and fluorescence in the specimen can be ignored.
$k_{AB}$- factors can be either determined from samples with known composition or from first principle calculations.

### 3.5.1.2 The zeta factor method

30 years after Cliff and Lorimer presented their method, Watanabe and Williams (2006) introduced the ζ- factor method that has the advantage of utilizing pure-element standards instead of multi-element standards as well as the built-in X-ray absorption correction with simultaneous mass thickness determination.

$$\boldsymbol{\rho t} = \zeta_A \frac{\boldsymbol{I_A^X A_A}}{\boldsymbol{C_A\, D_e}} \tag{31}$$

Equation (31) represents an element in a compound with concentration $C$ and X-ray absorption $A$. where $\rho t$ represents the mass thickness and $D_e$ the total electron dose measured during the experiment via the EEL spectrometer drift tube, a counts-to-electrons-conversion-calibrated CCD camera, a calibrated viewing screen, or a Faraday cup (Kothleitner et al., 2014).
Thickness determination should be as accurate as possible therefore the parameterization scheme for the inelastic mean free path $\lambda$ as suggested by Malis et al. (1988) is known to be erroneous and should be only used as a coarse approximation. The absolute thickness within this thesis was determined by relating $t/\lambda$ maps of the whole specimen to its cross sectional thickness prepared after the analytical measurements with a focused ion beam (FIB) instrument. The absorption-correction term for a single X-ray line is given by Philibert (1963):

$$\boldsymbol{A_A} = \frac{\left(\frac{\boldsymbol{\mu}}{\boldsymbol{\rho}}\right)_{sp}^{A} \boldsymbol{\rho t\ cosec\ \alpha}}{\boldsymbol{1 - exp}\left[-\left(\frac{\boldsymbol{\mu}}{\boldsymbol{\rho}}\right)_{sp}^{A} \boldsymbol{\rho t\ cosec\ \alpha}\right]} \tag{32}$$

Where $(\mu/\rho)_{sp}^{A}$ is the mass absorption coefficients of the characteristic X-ray line in the sample and α is the X-ray take-off angle.
The built-in absorption correction helps for light-element analysis and permits more satisfactory quantification results. As for the k-factors, a decent determination of sensitivity factors (ζ-factors) is essential for the fidelity of the quantification results (Fladischer and Grogger, 2014).

### 3.5.1.3 Acquisition and analysis of ζ-factors step by step.

ζ-factor determination is based on Equation 31 and 32. Values for the mass absorption coefficient of the characteristic X-ray line in the sample are available at the NIST website (http://physics.nist.gov/PhysRefData/FFast/html/form.html).

#### 3.5.1.3.1 Thickness measurements – sample preparation

Considering Equation 31 the mass thickness plays an integral part in ζ-factor quantification. The relative thickness is conveniently determined from EELS measurements by producing $t/\lambda$ maps. To get the absolute thickness the inelastic mean free path has to be known. An approximation was formulated by Malis et al. in 1988. These values, however, can be seen as coarse estimates of the true values. A better accuracy can be gained by experimentally determining the mean free path of the desired material. A basic approach deals with samples of known geometry as described by Kothleitner et al. (2014). According to this method, a rotationally symmetric cone acting as a thickness reference, and a plane, parallel-sided lamella for quantitative measurements, should be prepared out of a bulk sample. Thanks to the cone-shape symmetry of the calibration sample, the thickness can be measured and $\lambda$ can be determined via EELS. Here again: knowing $\lambda$ of the material is essential for absolute thickness determination.

Within this thesis, the measured FIB lamella was re-embedded and a FIB cross section was cut (Fig. 53). Hence the absolute thickness was measured directly on the re-embedded FIB lamella and related to $t/\lambda$ maps previously acquired on the initial lamella. Thereby $\lambda$ was determined for the desired material and absolute thickness was calculated.

As Kraxner (2018) suggests in her dissertation, solely copper Omniprobe grides should be used because their shape is better defined than molybdenum grids. Further plasma cleaning prior to FIB preparation is suggested. Grid and rod should be mounted on different grids each on the uppermost edge of the grid's "central-finger". This geometry ensures to be as close to the center of the holder as possible, to minimize X-ray absorption of the holder as well as from the grid.

#### 3.5.1.3.2 ζ-factor acquisition

On a four-spectrometer system ζ-factors should be acquired for each quadrant separately while tilting the holder towards the detector. The lamella, as well as the rod, should point in the direction of the holder axis when mounting the sample. To avoid shadowing of the holder and additionally lower the absorption within the sample the sample should be tilted towards Q4 with -15°and Q1 with +15°, then the sample should be rotated for 180° and then tilted towards Q3 with -15°and Q2 with +15°. Further correction files (peak position and precise peak form for the used detectors once determined and stored are used for correction to improve the analysis of the measured intensities) should be loaded.
The probe current and the live time directly influence the electron dose during acquisition, which is defined as

$$\boldsymbol{D_e = N_e I_p \tau} \tag{33}$$

where $N_e$ is the number of electrons in one unit of electric charge, $I_p$ is the beam current and $\tau$ the live time.
Therefore, knowing the live time and the current is essential. The live time is the time period the detector is actually measuring X-ray counts and is not busy processing and analyzing them. The time the detector is busy is called dead time. The real time is the combination of live- and dead time. One has to make sure that the correct time is used in the acquisition software. Due to issues with erroneous acquisition times using DM spectrum imaging, the EDX measurements within this thesis were obtained using a scanning window (~1,600 nm²) in which the electron beam was scanned while a single EDX spectrum was acquired. Further, electron beam damage is minimized thanks to the high scan speed (~20 µs/ pixel).
The current can be measured using the EEL spectrometer drift tube. Therefore, the sample must be removed such that the electron beam does not hit it. The software acquires 10 measurements in 10 seconds. To avoid errors due to current changes during the EDX acquisition, the mean value of current measurements before and after the acquisition should be used.
Unfortunately, current measurements using the drift tube are inappropriate for simultaneous EELS core-loss and EDX measurements for the conversion of ζ-factors into EELS cross sections. This is because one has to lower the primary energy to e.g. 60 keV in the GIF's settings so that electrons hit the drift tube, thus influencing EELS accuracy. Therefore, a calibrated CCD can be used to measure the count rate ($e^-$/s) via the zero-loss

peak intensity (in a hole) before and after each EDX acquisition and using the calibration to calculate the electron dose.

Before and after the EDX measurement, EELS-LL spectrum images over the same area as the EDX scanning window should be performed to monitor contamination.

#### 3.5.1.3.3 Intensity determination

X-ray intensity determination requires the removal of the bremsstrahlung background and the extraction of characteristic X-rays intensities. The most primitive method for background subtraction is the window method based on graphical considerations only. Two background windows and a signal window are defined in the EDX-spectrum. The background windows should be equally placed on either side of the signal window, while all three windows have the same size. The average of the two background windows gets then linearly subtracted from the signal. One can easily see that this method will fail on the low energy side of the spectrum due to the curvature of the bremsstrahlung background or where overlapping lines have to be considered. Most commercially available EDX software packages use more sophisticated routines for background removal that rely either on the Kramers' model or on the top-hat approach.

#### 3.5.1.3.4 Kramers' model background subtraction

The Kramers' (1923) model as implemented in DM is a reliable tool for background subtraction at higher X-ray energies but it does not account for the absorption of Bremsstrahlung, which is important especially in the low energy regime.

Fig. 39(a) shows that in the low energy range (~0.2 keV) the background model (red) is too high.

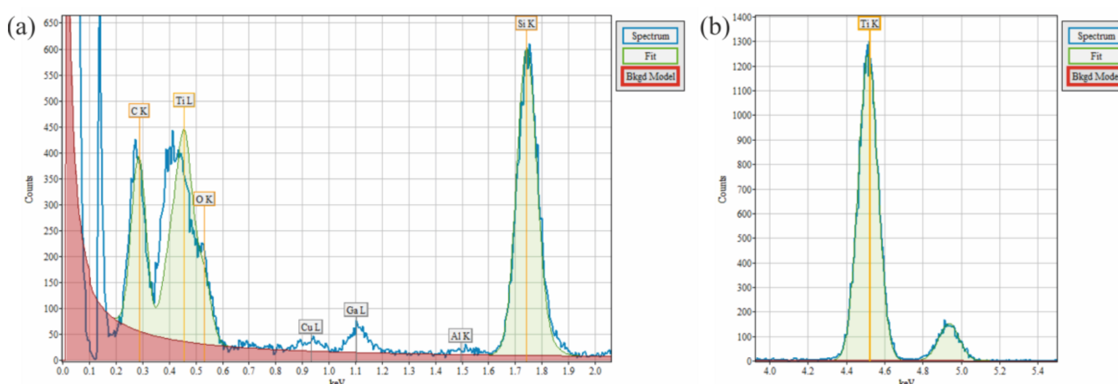


**Fig. 39** Background- and signal fit using the Kramers' model in the range of 0 keV-2 keV (a) and at the Ti-K peak (b). The experimental spectrum is shown in blue, the background fit in red and the fitted signal in green.

The advantage of this model within DM is that the user can easily see how well the signal fit (shown in green) corresponds to the experimental spectrum (shown in blue). The Gaussian shape of the Ti-L fit does not match the experimental spectrum well because the O-K edge right above is not fitted as a single gaussian peak. Adequate results are obtained if no background removal is needed in the low energy regime and the peaks have Gaussian shape.

#### 3.5.1.3.5 Top-hat filter background subtraction

The top-hat filter approach is useful for multi-element samples especially in energy regions below ~1.5 keV where the Kramers' model mostly fails. Further, the user's influence on the extracted characteristic intensity is eliminated as this approach relys on pure mathematics as explained in section 3.5.1. A constant offset and a steady slope is removed from the spectrum by convoluting the spectrum with a 'top-hat' filter function. The method implemented within DM fits the second derivative of Gaussian peaks to the filtered spectrum and uses the fitting parameters to calculate the area of the Gaussians (Equation (28)) as shown in Fig. 40. The disadvantage of the method as implemented in DM is, that the residual signal is not visible. Thus, it is hard to see how well the fit corresponds to the experiment.

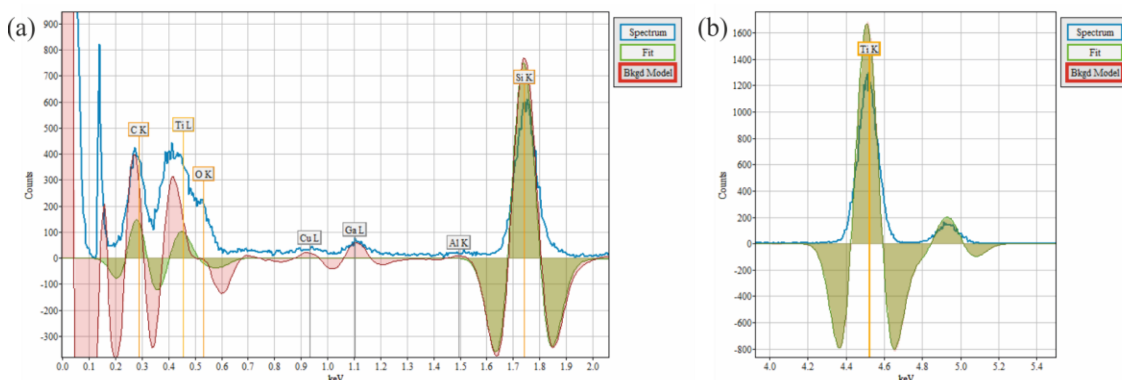


**Fig. 40** Top-hat filter correction: the experimental spectrum is given in blue, the background fit in red and the signal fit in green.

#### 3.5.1.3.6 Which method to choose?

Besides the top-hat filter method all methods rely on the experience of the user thus different users can get different results. Within our working group we addressed the question of the users influence on intensity extraction and on the credibility of the results. The results were already published by Kraxner (2018), however, for a clearer understanding on the topic, they are summed up here. Starting from three (Si, $Al_2O_3$,

$TiO_2$) simulated (DTSA II - Halley 2014-08-01 revision) spectra to cancel out artefacts six employees in the group were asked to evaluate the peak intensities using five different approaches. Simulating conditions are given by (Kraxner, 2018).

The approaches are as followed:

1) Kramers model as implemented in DM (v.2.3), parameters like Background windows, peak fitting settings etc. were adjusted by the user.
2) Top-hat model as implemented in DM (v.2.3).
3) Esprit 2.0 by Bruker.
4) Window method using a batch script as a free software implementation GNU awk (Aho et al., 1988) written by Masashi Watanabe. To compare the window method with the other approaches a correction of the recommended window width (1.2*FWHM corresponding to 85% of the whole peak's area) was applied. These corrected intensities are referred here as "Gawk 100".
5) Individual "Fit" approach of each user where mainly Gaussian peaks were fitted after a (mostly via a linear) background subtraction or simply a summing up of channel widths for signal and background determination.

Fig. 41 shows the results of the experiment. Plotted are the relative intensities of the EDX signal in %. The "true" intensity value (average value of the five different methods) is zero. The deviation of each participant of that value is plotted (P1 to P6). The grey bars represent the average value of each method to clearly see the differences arising by the chosen approach.

The results of this experiment indicate that if subjective parameters, a function of the user's experience (all users a similar experience with DM but not with Esprit), are kept to a minimum, all participants receive similar results, as seen e.g. for the top-hat method. The deviations seen in the gawk method and partly also in the "Fit" method are the result of integrating over an area in the spectrum, thus are limited to the channel width. Small differences in the width of the summed region can make a big difference on the extracted intensity. Therefore, if manual fitting is performed it is recommended to fit a Gaussian function to the peak and calculating the area underneath to be independent of the channel width.

Apparently, one cannot favor a certain method and the user has to decide for individual problems. Although the top-hat approach obviously provides reproducible values, they have to be treated with caution in the low energy region and when analyzing overlapping

peaks. The advantage of the modelling methods (Kramers method in DM or method implemented in Esprit) is, that the user can visually check if the peakfitting and background removal performs well. Regarding well separated peaks, the user's influence is generally low. Overlapping peaks require the right choice of program and its settings.

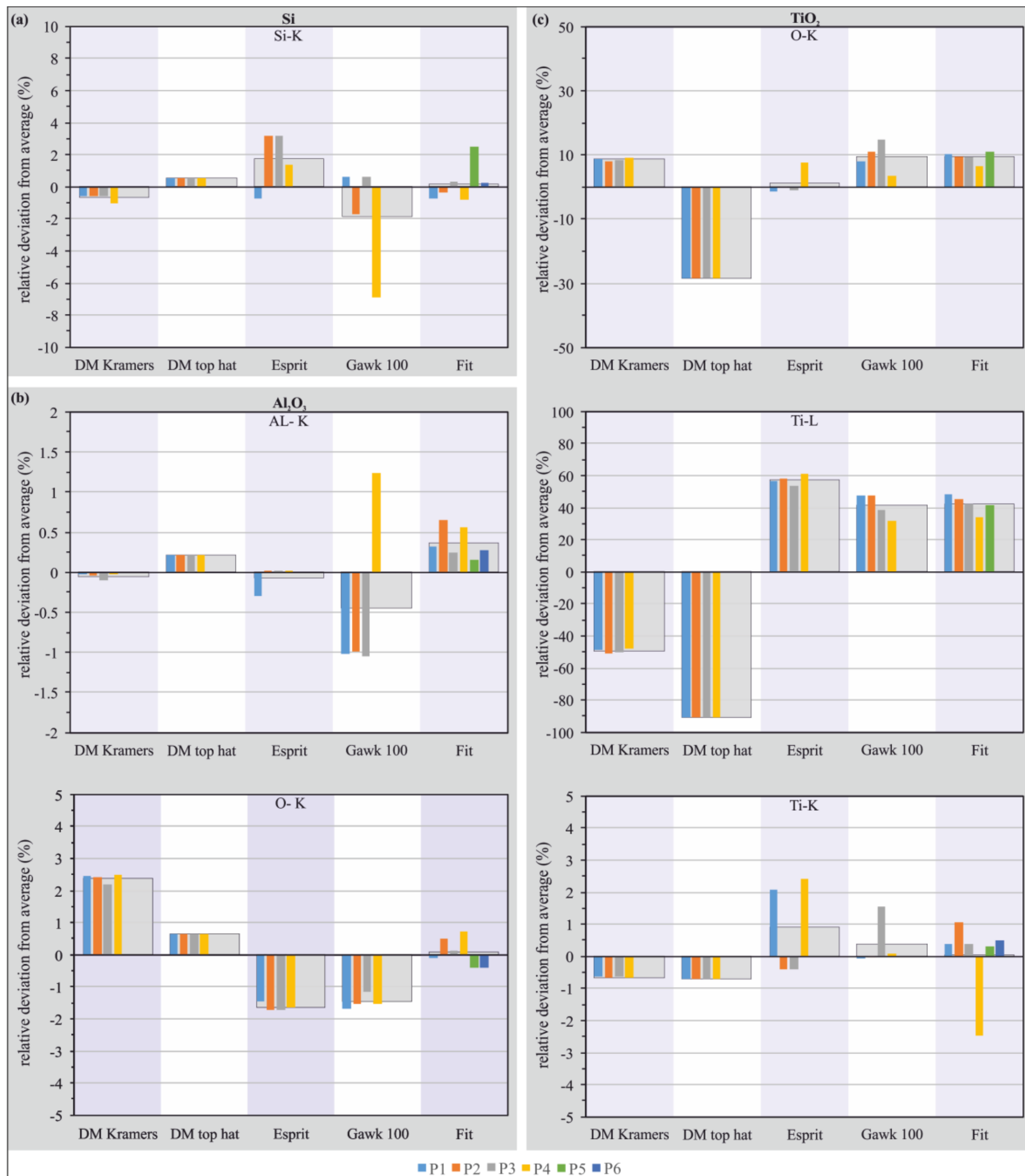


**Fig. 41** Relative deviation from the average peak intensities for (a) Si, (b) $Al_2O_3$ and (c) $TiO_2$ evaluated by six different users (P1 to P6) using five approaches: DM Kramers, DM Top-hat, Esprit, Gawk 100 and Fit.

# 4 Results on simulations and analysis

Within this section the findings from simulations and analysis will be presented and discussed. The first part is devoted on the one hand on cross section simulation via the FEFF code, on the other hand on improvements of the hydrogenic approach for cross section calculation (chapter 4.1). The second part deals with the analyzed materials showing the synergy between the outcome of structural determination along with quantitative results on the accurate treatment of reference materials (chapter 4.2).

## 4.1 Comparison of FEFF cross sections with the hydrogenic approximation

As outlined before, putting quantitative numbers to elemental concentrations require the knowledge of sensitivity factors. To convert experimental core-loss intensities to elemental ratios cross sections are needed that depend on the measurement conditions like the incident electron energy, collection angle and range of energy-loss (Williams and Carter, 2009)

As cross sections calculated via the hydrogenic approximation carried out with SIGMAK3 lack of fine structure details, quantification starting from the threshold energy of a specific element are fraught with uncertainty. FEFF simulations however, also representing fine structure details display a more realistic picture.

The question on the accuracy of hydrogenic calculations also relies on screening factors that have been adjusted over the past decades and it shall be reviewed here if a meaningful adaption can lead to better quantificational results. Slater (1930) has shown that a value of 0.3 resulted in a good agreement with measured energy levels and atomic radii for a wide range of atoms. Zener (1930) obtained a similar value of 0.3125 from helium atom wave functions. A single screening constant of 0.3 was long in use in commercial available programs. Egerton (1996) suggests two different screening constants that should be used instead of a single one, depending on Z. Comparing his results to the Hartree-Slater model as well as to experimental data he suggests to use screening constants of 0.6 and 0.5 for light ($Z \leq 10$) and heavy ($Z > 10$) elements respectively. SIGMAK3 still uses a preset value of 0.5 for the whole range of K-shell excitations.

Hydrogenic cross sections calculated with different screening constants will be compared to FEFF simulations. These differently obtained cross sections will be subsequently used for the analysis of EELS experiments of well-defined samples.

The amplitude factor, highlighted in grey in Equation (20) scales the cross sections according to the collection semi-angle $\beta$. Depicted in Fig. 42 are differential cross sections of K-edges from elements Be to Si as a function of energy in a certain collection angle $\beta$ simulated with FEFF9 and SIGMAK3. The simulation conditions are parallel illumination with collection angles ($\beta$) between 6 and 20 mrad. Thus an augmentation of the cross sections according to an increase in $\beta$ can be seen. This, on the one hand, can be interpreted as a benefit as the total cross section (area under the edge) increases. On the other hand, further away from the edge onset, the increase leads to a reduced signal to background ratio for example the N-K edge at 401 eV is superimposed on the tail of the C-K edge. For the FEFF9 simulations the following structural data files have been used and are given here with the inorganic crystal structure database (Hellenbrandt, 2004) number in parenthesis:

Be: metal (ICSD1425); B: BN (ISCD240999); C: $Ti_3SiC_2$ (ISCD180421); N: BN (ISCD240999); O: $Al_2O_3$ (ISCD51687); F: LiF (ISCD 44272); Na: NaCl (ISCD165592); Mg: MgO (ISCD158103); Al: $Al_2O_3$ (ISCD51687); Si: $Ti_3SiC_2$ (ISCD180421)

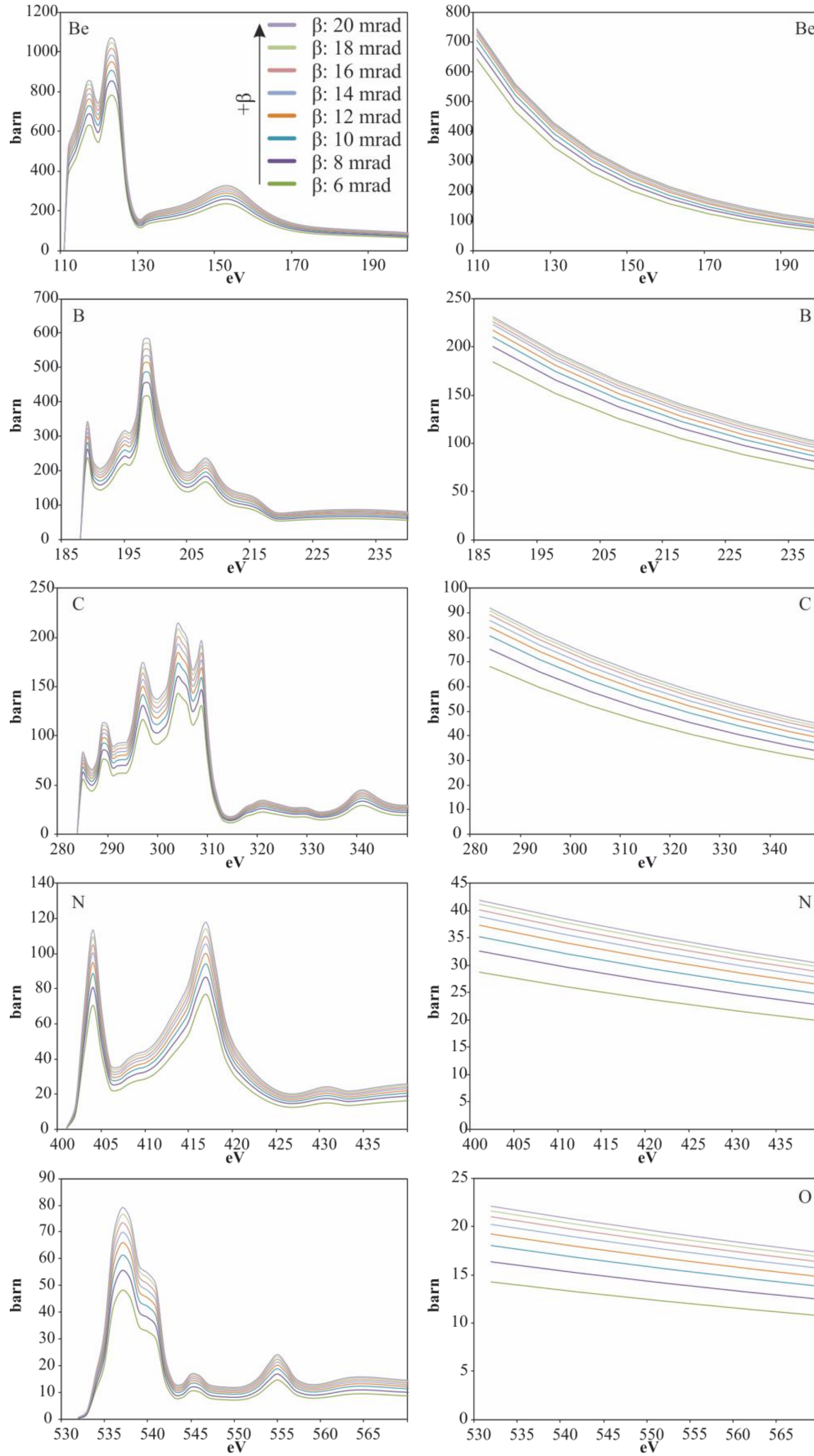


continued on next page

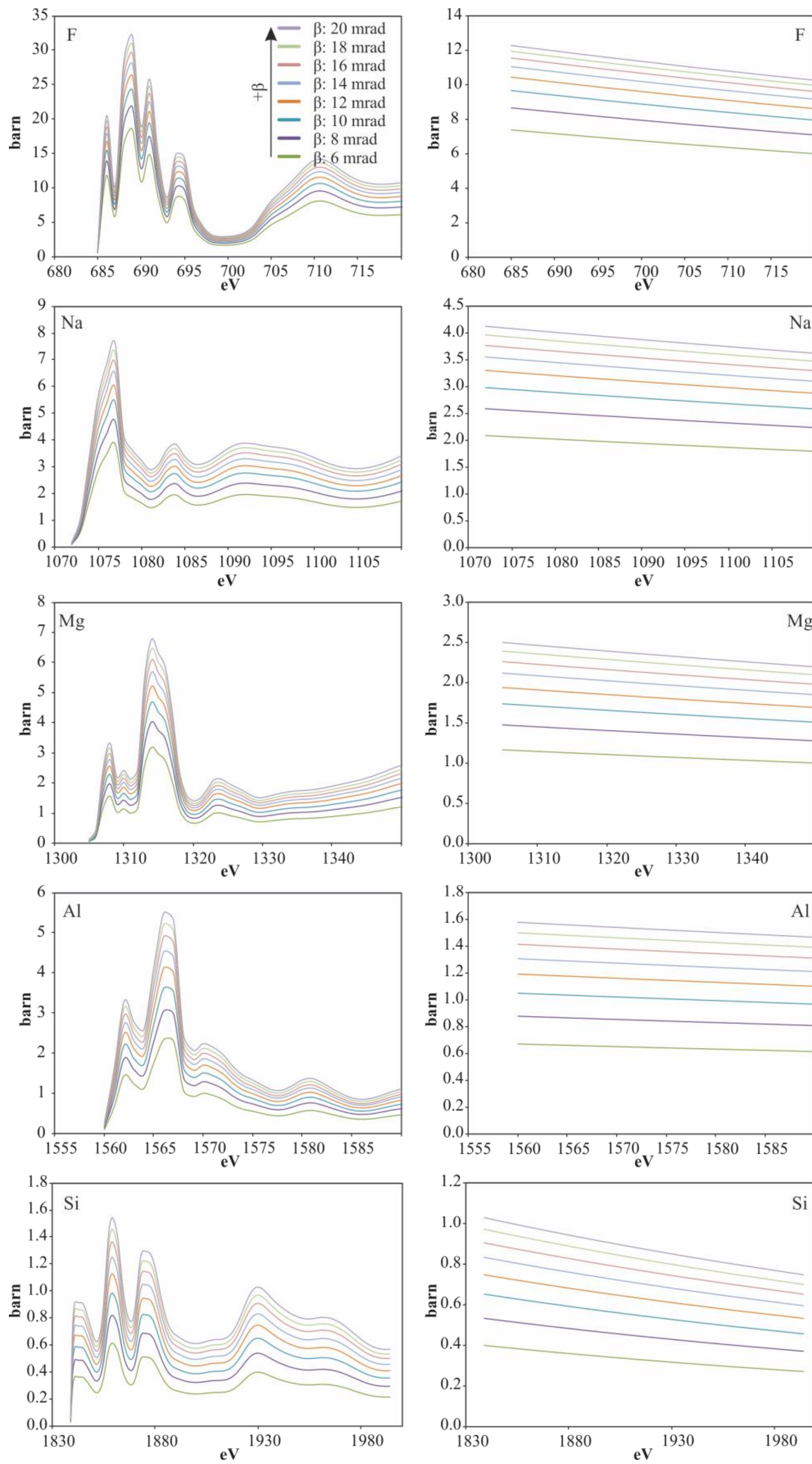


**Fig. 42** FEFF simulations (left column) and SIGMAK calculations (right column) for elements Z 3-14 and collection angles $\beta$ 6-20 mrad.

By plotting the cross section integral using an energy window of 100 eV starting at the edge threshold and dividing it by the abovementioned amplitude factor one can clearly see a raise in intensity along with a raise of β that follows a power law function (Fig. 43).

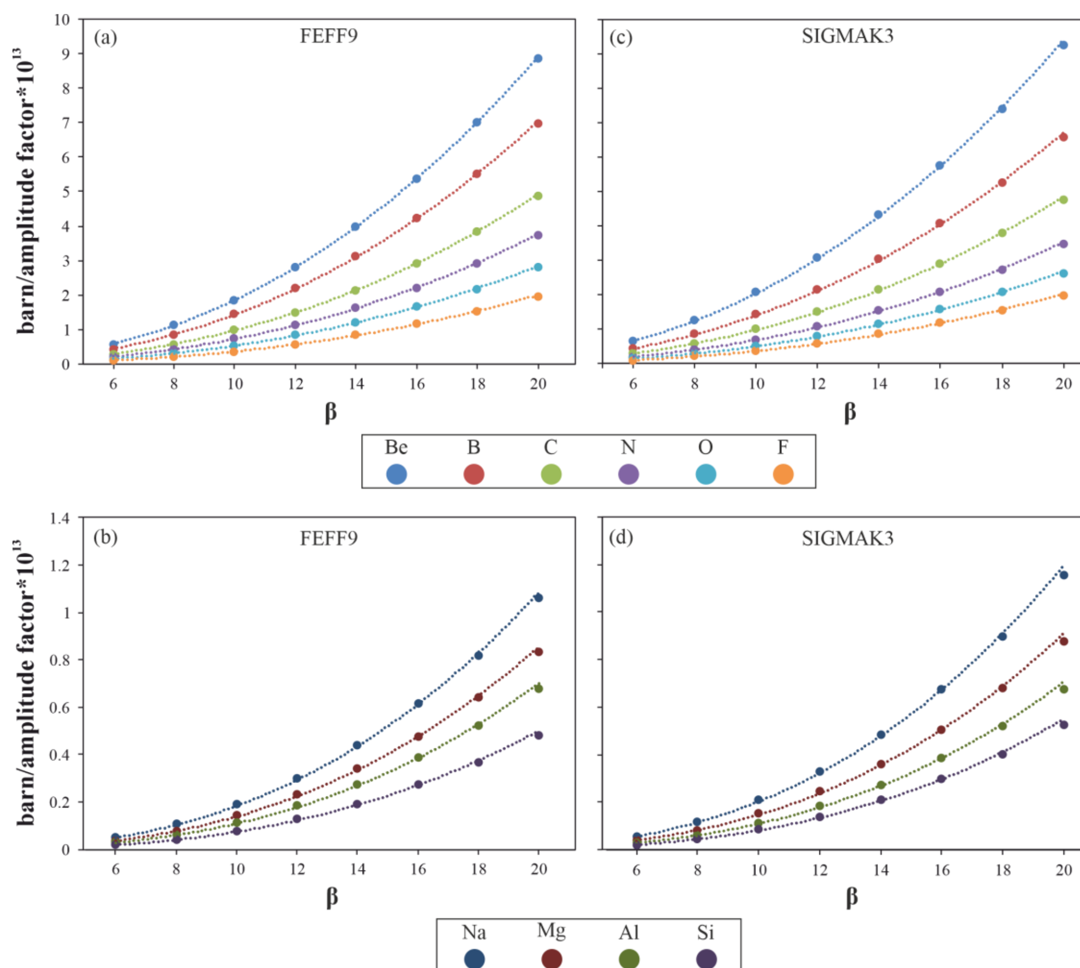


**Fig. 43** Cross-sections from K-edges divided by the amplitude factor given for elements Z 3-14 and collection angles $\beta$ 6-20 mrad. (a, b) shows results for FEFF simulations, (c, d) shows SIGMAK calculations.

The deviations between SIGMAK3 and FEFF9 simulated cross sections normalized by the amplitude factor are shown in % in Table 3. The right column gives the average deviation of each row.

**Table 3** Deviation (%) of SIGMAK3 from FEFF9 cross sections normalized by the amplitude factor.

| | β [mrad] | 6 | 8 | 10 | 12 | 14 | 16 | 18 | 20 | average |
|---|---|---|---|---|---|---|---|---|---|---|
| Elements | Be | 12.7 | 12.0 | 11.1 | 9.9 | 8.6 | 7.2 | 5.7 | 4.2 | 8.9 |
| | B | -0.1 | -0.3 | -0.8 | -1.6 | -2.5 | -3.5 | -4.6 | -5.8 | -2.4 |
| | C | 2.1 | 2.2 | 1.9 | 1.3 | 0.5 | -0.4 | -1.3 | -2.4 | 0.5 |
| | N | -4.2 | -3.9 | -4.0 | -4.3 | -4.9 | -5.5 | -6.3 | -7.2 | -5.0 |
| | O | -3.9 | -3.4 | -3.4 | -3.7 | -4.1 | -4.7 | -5.4 | -6.2 | -4.4 |
| | F | 2.5 | 3.3 | 3.5 | 3.4 | 3.0 | 2.5 | 1.9 | 1.2 | 2.7 |
| | Na | 4.8 | 6.1 | 6.8 | 7.0 | 7.0 | 6.8 | 6.5 | 6.0 | 6.4 |
| | Mg | 0.0 | 1.5 | 2.4 | 2.8 | 3.0 | 3.0 | 2.8 | 2.5 | 2.3 |
| | Al | -6.6 | -5.1 | -4.1 | -3.5 | -3.2 | -3.0 | -3.1 | -3.2 | -4.0 |
| | Si | 1.8 | 3.3 | 4.5 | 5.2 | 5.7 | 6.0 | 6.0 | 6.0 | 4.8 |

### 4.1.1 Appropriate screening factors for the hydrogenic approximation

A direct comparison of FEFF simulations and the hydrogenic approximations is shown in Fig. 44. This gives an intuitive picture that on average for elements ranging from Be to Si, the hydrogenic curves calculated with a screening factor of 0.8 fit better than those calculated with the preset value within SIGMAK3 of 0.5.

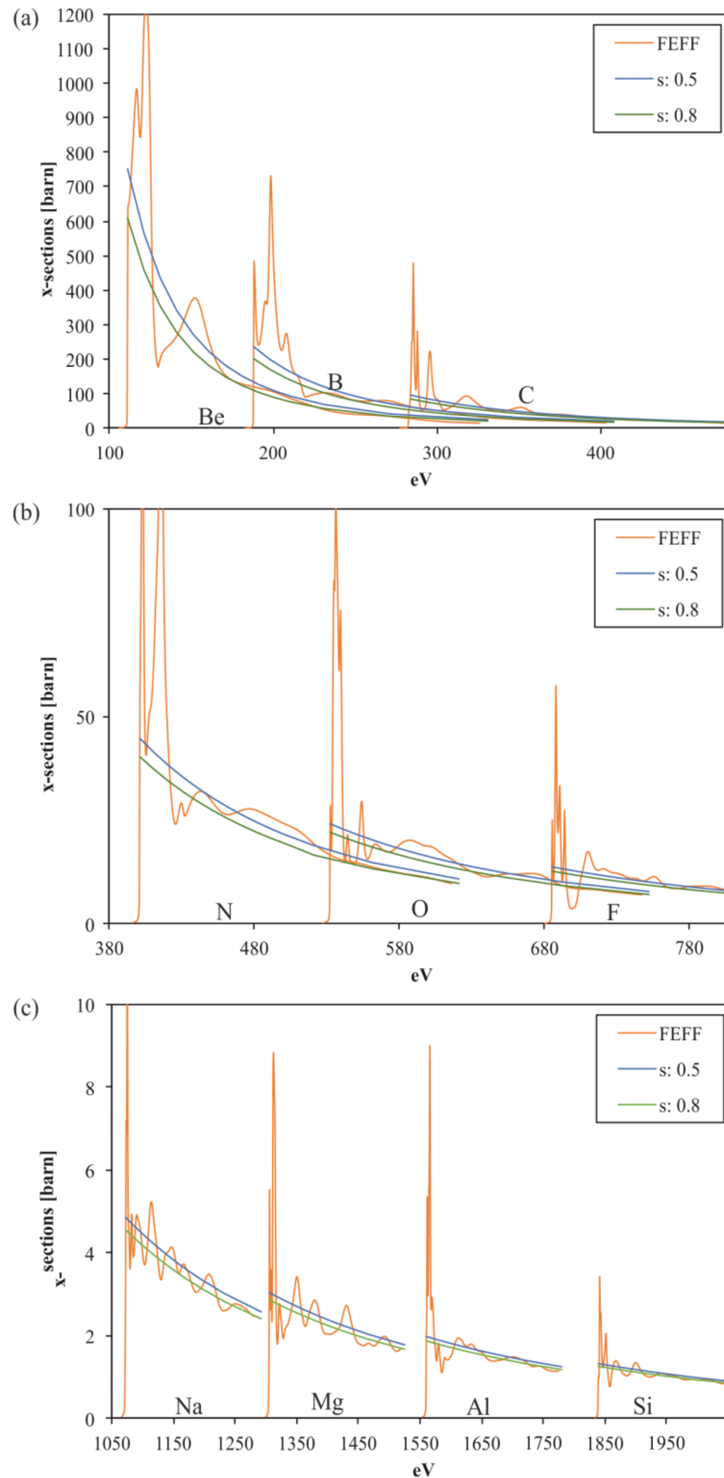


**Fig. 44** (a-c) FEFF vs. hydrogenic ratios for different integration width Δ and offsets.

The situation is more sophisticated as one plots the relative deviations as a FEFF signal to hydrogenic signal ratio and looks at the mean least deviations (Fig. 45). The values given here shall be correct for elements ranging from C to Si. The ELNES for very light elements (Be, B) is underestimated by the hydrogenic approximation as visualized in Fig. 44(a). Starting at the edge threshold, spanning a 50 eV wide integration window ((Fig. 45(a)), suggests a better accordance when using a screening factor of 0.4 for the light elements (Z 6-9), whereas a screening factor of 0.7 would provide the best match for the heavier elements (Z 11-14), however cross section fluctuations related to bonding effects exist. Utilizing a 100 eV integration window starting 100 eV above the threshold energy in the EXELFS region (Fig. 45(b)), a shift of the screening factors towards higher values of s: 0.7 and s: 0.9 for the light and heavy elements, respectively, can be observed.

This findings do not change significantly when moving from a low collection angle to a $C_s$-probe corrected collection geometry ((Fig. 45(c)) setting $\alpha$ to 19.6 mrad and $\beta$ to 40 mrad (resulting in an effective $\beta$ of 38 mrad when convergence correction is applied (referring to Equation 11). Employing screening factors s: 0.7 and s: 0.8 for light and heavy elements, respectively, leads to a less subjective and more reliable analysis, hence avoiding large systematic quantification errors.

The above is supported by the fact that the intensities of the ELNES are stronger modified by larger collection angles than the EXELFS region, thus the screening factors derived from the ELNES region are more sensitive to changes in the experiment.

The deviations of SIGMAK3 from FEFF in dependence of the different screening constants is tabulated in Table 4.

**Table 4** Deviation of SIGMAK3 from FEFF cross sections in % calculated with the preset screening constant of 0.5 and the modified values using the mentioned parameters

| Element | Δ 50 eV @ TE<br>α= 6 mrad; β= 6.5 mrad | | | Δ 100 eV @ 100 eV offset<br>α= 6 mrad; β= 6.5 mrad | | | Δ 100 eV @ 100 eV offset<br>α= 19.6 mrad; β= 40 mrad | | |
|---|---|---|---|---|---|---|---|---|---|
| | preset | | modified | preset | | modified | preset | | modified |
| C | -3.72 | s= 0.4 | 1.66 | 11.23 | s= 0.7 | -1.05 | 10.74 | s= 0.7 | 2.45 |
| N | -8.34 | | -4.00 | 7.63 | | -2.67 | 3.27 | | -3.61 |
| O | -5.37 | | -1.50 | 12.80 | | 3.47 | 5.70 | | -0.49 |
| F | 2.73 | | 7.84 | 7.37 | | -0.40 | 1.92 | | -3.36 |
| Na | 9.53 | s= 0.7 | 3.26 | 13.87 | s= 0.9 | 0.79 | 5.38 | s= 0.8 | -1.37 |
| Mg | 3.40 | | -2.01 | 13.02 | | 1.16 | 3.67 | | -2.48 |
| Al | -0.71 | | -5.51 | 14.82 | | 3.73 | 5.71 | | -0.13 |
| Si | 7.47 | | 2.66 | 12.74 | | 2.66 | 4.21 | | -1.19 |

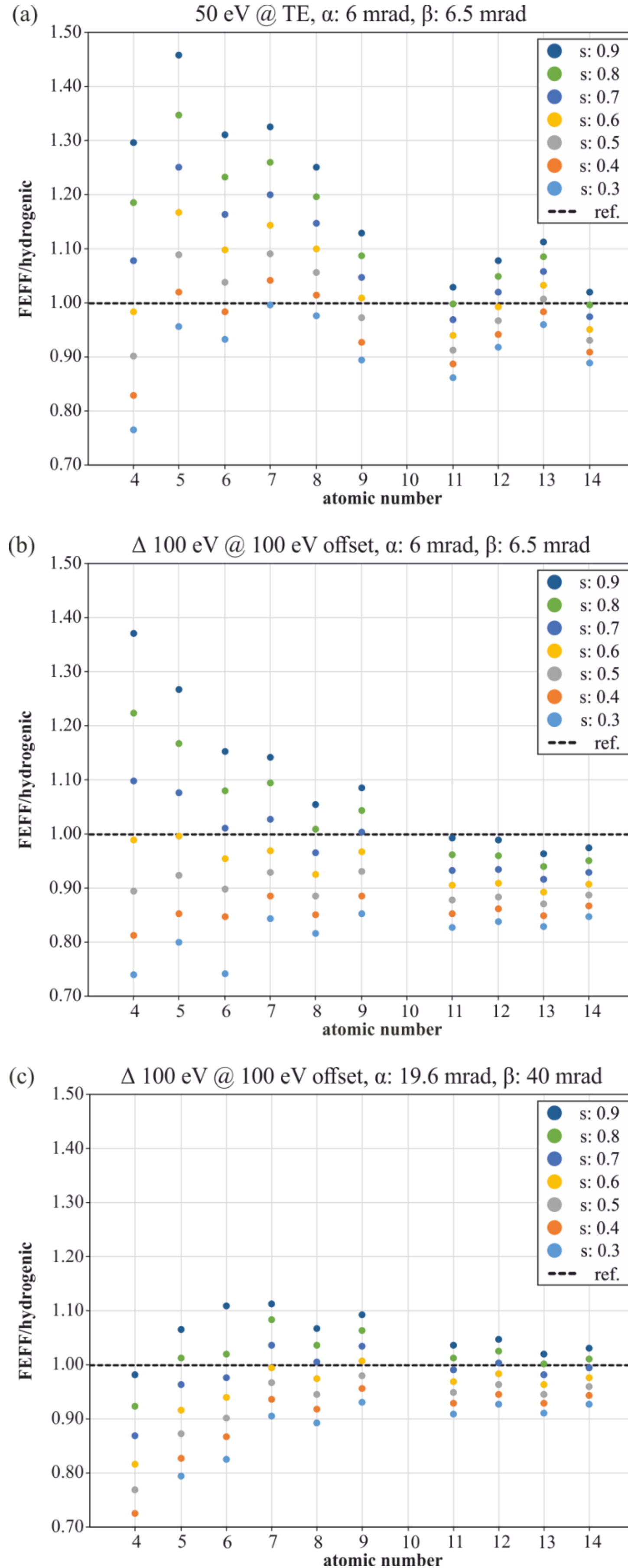


**Fig. 45** (a-c) FEFF vs. hydrogenic ratios for different integration width Δ and offsets.

## 4.2 Data analysis

This chapter is designed in such a way that proceeding from a well-defined characterization path, the treatment of individual samples is described such that it leads to a meaningful quantification comparing the outcome of FEFF cross sections with hydrogenic ones. The outcome in combining experimental and simulation techniques to obtain structural information on the materials under investigation, as well as analytical factors needed to turn spectroscopic intensities into concentrations is shown in (Fig. 46). The term multimodal analytical electron microscopy (AEM) in Fig. 46 should emphasize the possibility of complementing EELS information with EDX data to provide a concept for integrative analysis.

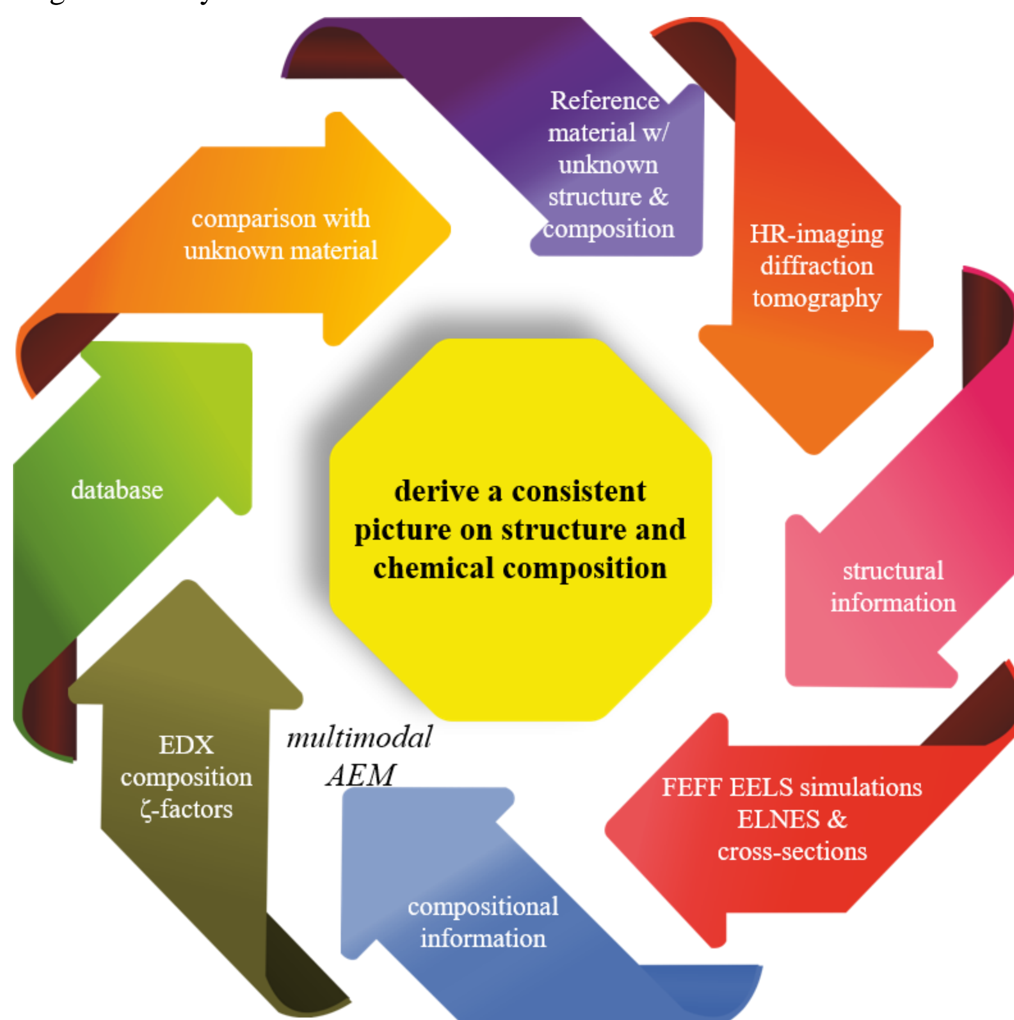


**Fig. 46** Characterization path envisioning the combination of structural as well as analytical TEM methods to gain a consistent picture on the crystallographic structure and chemical composition of materials.

Starting out with the tungsten carbide system, the connection between crystallographic data obtained by ADT (chapter 4.2.1) with simulated electron energy-loss fine-structures

(chapter 4.2.2) is shown. SAED and HR-imaging methods are used for the structural characterization of a $Ti_3SiC_2$ MAX phase (chapter 4.2.3) and the effect of EELS cross sections as well as the role of intrinsic parameters as screening factors will be discussed. Further, a comparison of the EELS compositional analysis results with EDX measurements will be made. In a last step, an unknown titanium carbonitride coating (chapter 4.2.4) on a WC substrate is studied, showing that EELS quantification can be successful even if structural characterization is failing.

### 4.2.1 ADT experiments on tungsten carbide

ADT experiments were performed on a WC with a Co binder cutting insert, prepared by the PIPS routine as described in chapter 3.1.1, at the Johannes Gutenberg University in Mainz using a TECNAI F30 S-TWIN microscope with a field emission gun operated at 300 kV, using spot sizes of around 75 nm and with a camera length of 380 mm. The microscope is equipped with a $C_2$ aperture of 10 µm and a Nanomegas DigiStar precession unit.

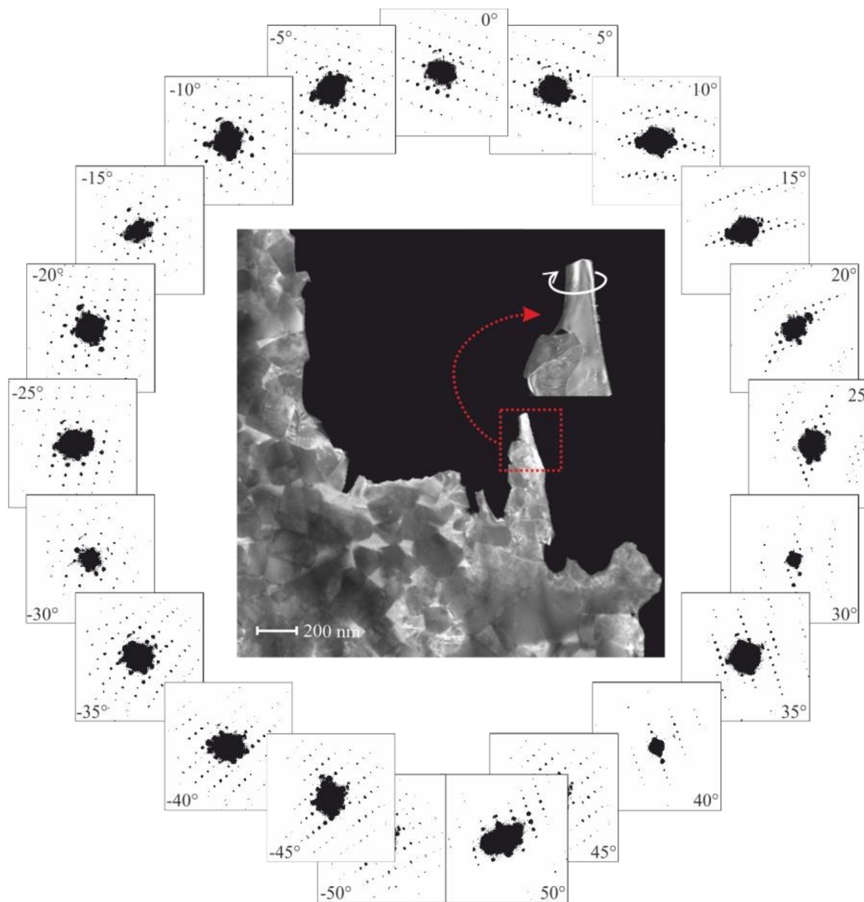


**Fig. 47** Bulk sample of tungsten carbide hard metal insert. Tilting of the WC grain is indicated in the insert. The outer circle symbolizes the sequential acquisition of a 2D diffraction pattern image stack.

A Fischione dual-axis tomography holder (Model 2040) was used to acquire a tilt series where diffraction patterns were recorded using a 4k x 4k Gatan US4000 CCD camera (Gatan, Inc., Pleasanton, USA) via the Gatan DM software suite.

ADT along with PED enables an almost quasi-kinematic collection of the electron diffraction intensities derived from a single nanocrystal (Fig. 47, insert). Both methods are further applied for the structure determination of the carbide phase. The selected crystal for ADT data acquisition was tilted from -50° to +50° with 1° steps while the precession angle was 1° with a beam diameter of ~75 nm (Fig. 47, outer circle).

By reconstructing the 3D volume of the $W_{0.5}C_{0.5}$ (δ WC) in reciprocal space, a hexagonal structure with a P-6m2 space group was confirmed for our starting material (Fig. 48(a-c)). The unit cell is characterized by the constants *a*=0.2952, *b*=0.3018, *c*=0.2831 nm which agree well with the literature: *a*=0.2906, *c*=0.2837 nm (e.g. Kurlov and Gusev, 2013).

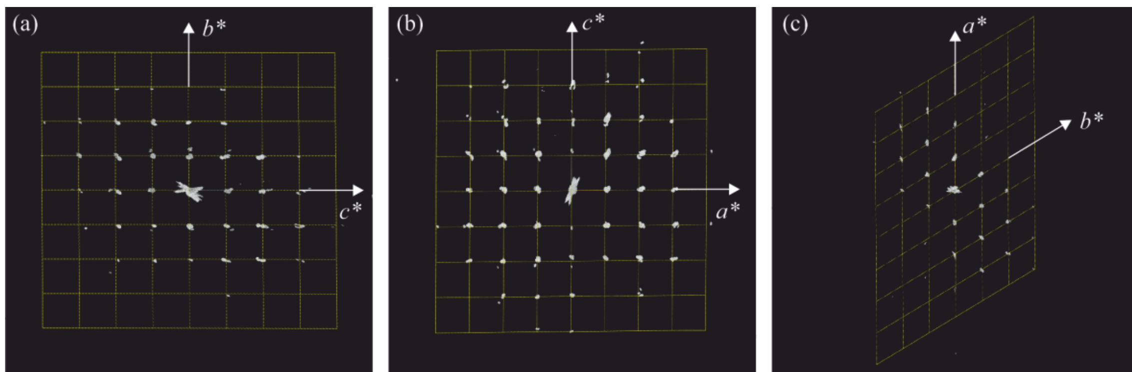


**Fig. 48** Reconstructed 3D reciprocal space of WC viewed along the main directions (a) [100], (b) [010] and (c) [001].

The extracted intensities were used for the *ab initio* structural solution which was performed by the SIR2014 (Burla et al., 2015) software. In this regard tungsten and carbon are in good agreement with the electron potential (Fig. 49).

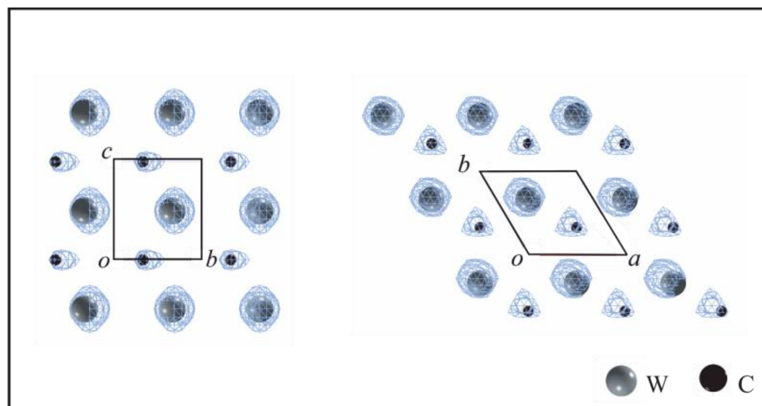


**Fig. 49** Electron potential map of WC derived from structure solution overlaid with the atomic model

The *ab initio* structure solution converged with a final residual R of 2.88% with a resolution of 0.08 nm.

SIR2014 allows the user not only to adjust the electron potential for the atomic positions available in the crystal unit cell, but also allows the output of a structure file (CIF).

### 4.2.2 FEFF simulation on WC

According to the prescribed characterization path in Fig. 46, structural information reconstructed from the ADT, now available as a CIF file, serves as an input file for EELS fine-structure simulations with FEFF9. The simulations are performed at conditions reflecting the experiment with a collection angle of 6.5 and a convergence angle of 19.6 mrad conducted at 300 keV.

A comparison is made between the experimental carbon K-edge and the FEFF9 simulation together with the calculated hydrogenic approximation where the SIGMAK3 default value of 0.5 was taken as the screening factor (Fig. 50).

The simulation reproduces the overall shape of the experimental spectrum in the range of about 100 eV starting at the threshold quite well.

While almost all near threshold features in the range of 284 and 300 eV are found, a slight difference, however, can be observed in the split intensity ratio of the of the initial peak and at around 290 eV in the triple peak structure, where only a doublet peak is found in the simulation.

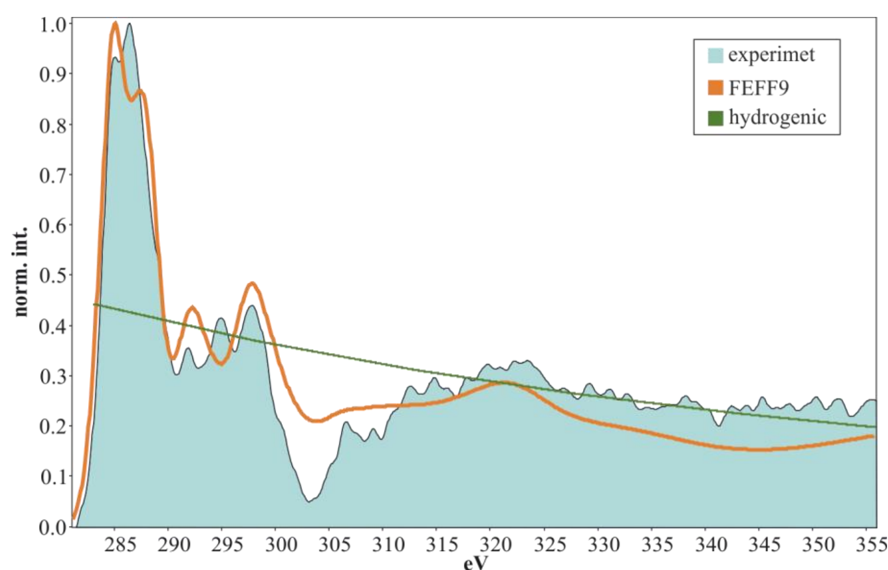


**Fig. 50** Measured EELS carbon K-edge of A WC grain (Fig. 47) in comparison with a FEFF9 simulation and the hydrogenic approximation calculated with SIGMAK3.

Also, EXELF-structures are largely comparable. However, when compared to the experimental spectrum they appear to be expanded on the energy scale.

Generating energy-differential partial cross sections can be seen as a huge benefit of multiple scattering simulations. What can be illustrated, although the scale is normalized in Fig. 50, is that when performing compositional analyses on EELS ELNES features using a small integration width, results shall be more reliable using FEFF than hydrogenic approximated cross sections, that ignore bonding effects.

### 4.2.3 Titanium silicon carbide

The present phase is a PVD coating on a corundum substrate. As mentioned in section 2.3.1, TiSiC exist mainly in three modifications. As they can be distinguished by the extension of the c-axis due to the number of Ti layers in between the Si layers, HR-imaging along with SAED techniques should shed light on their structure. However, EELS experiments should also reflect the stoichiometry of the compound. Furthermore, a structurally well-known sample can be used to verify different cross section models as described in section 4.1, supplemented with cross sections gained by the conversation from EDX ζ-factors.

#### 4.2.3.1 SAED investigation

SAED investigations have been carried out on the TF 20 microscope using the smallest SA (10 μm) aperture. Diffraction patterns have been acquired on both, the corundum substrate and the PVD coating. Thus revealing the TiSiC layer $[10\bar{1}0]$ is epitaxially grown on the $[2\bar{1}\bar{1}0]$ corundum substrate Fig. 51(a,c,d).

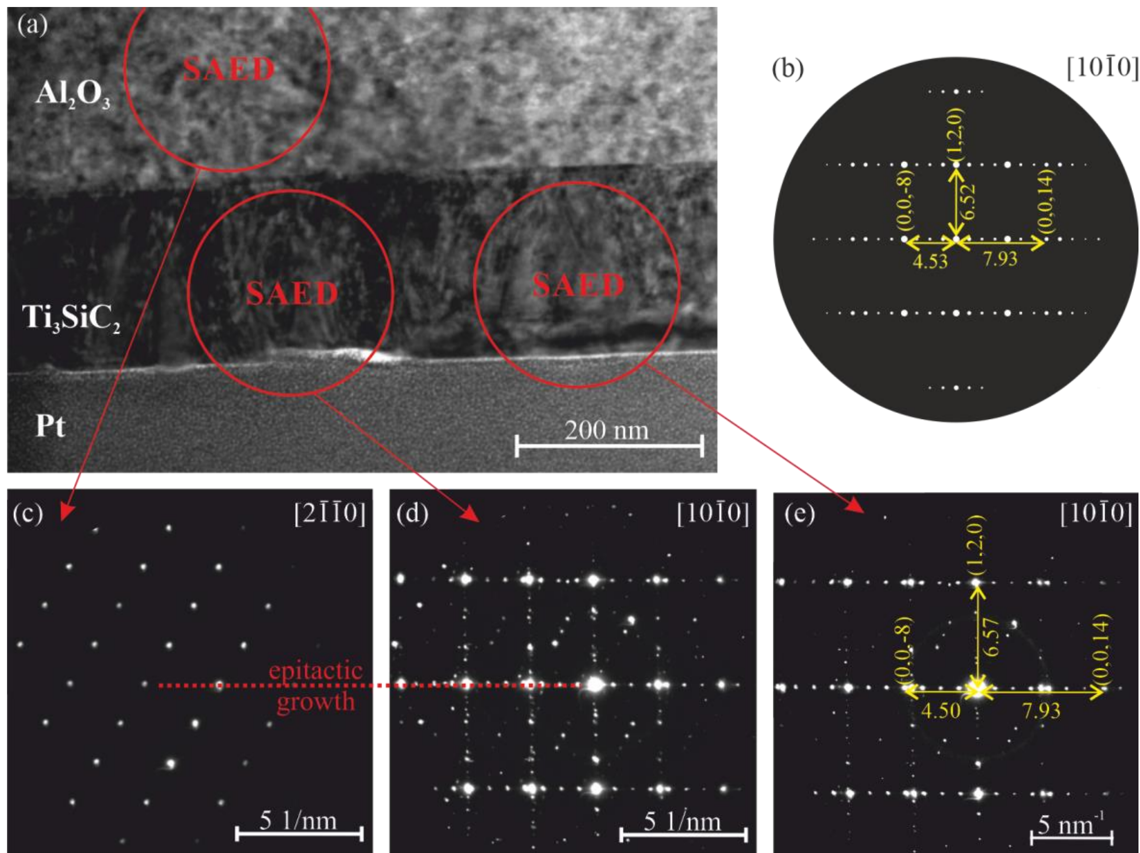


**Fig. 51** (a) BF image of a $Ti_xSiC_{x-1}$ coating in between the $Al_2O_3$ substrate and the Pt protection layer. The areas where the SAED pattern were taken are indicated. (b) Diffraction simulation (JEMS) of $Ti_3SiC_2$. Distances of discrete reflections are shown and measured in $nm^{-1}$. (c) Diffraction pattern of the $Al_2O_3$ substrate. (d, e) diffraction pattern of the thin film coating.

When the diffraction patterns were compared to JEMS simulations, carried out using a $Ti_3SiC_2$ structural data file (ISCD180421) (Fig. 51 (b)), the 312 stoichiometry could be proven by identifying the same diffraction spots in $[10\bar{1}0]$ direction (Fig. 51 (e)).

### 4.2.3.2 HR-imaging

HR HAADF images were acquired with the TITAN³ microscope on a sufficiently thin sample. HR-imaging makes the nanolaminated crystal structure of the MAX phase visible, by displaying the stacking sequence of $Ti_3SiC_2$ layers (Fig. 52). Due to the Z contrast, the $Ti_3C_2$ layers appear brighter than the Si layers on a HAADF image. Fig. 52(b) shows a schematic section of the crystal structure, where the dimension of the unit cell is indicated by a black square. HAADF-STEM images have been simulated with the multi-slice program QSTEM and compared to the experimental images (Fig. 52 (a,c)). The supercell structure model consists of (40x22x3) unit cells (*a*=122.616, *b*=67.4387, *c*=52.905 Å) and was used for the simulations. The probe array was 400x400 pixels with 0.29 Å resolution. The slice thickness was 2.4935 Å. The image simulations covered an area of 140x140 pixels.

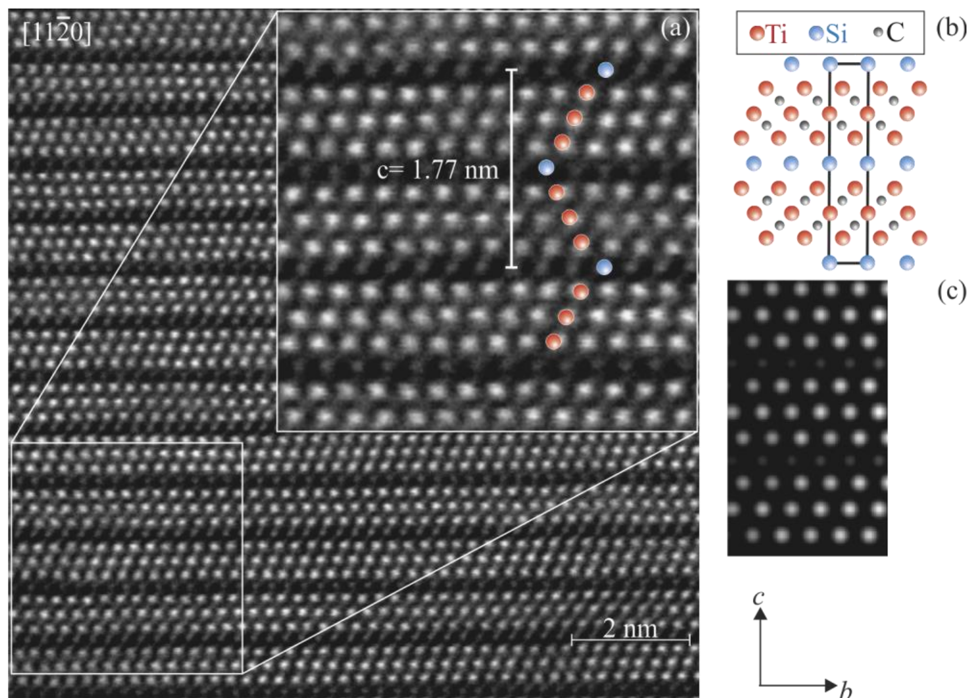


**Fig. 52** (a) HR-HAADF-STEM image of $Ti_3SiC_2$, (b) diagrammed lattice with the unit cell's extension in c direction and (c) HAADF simulation performed with QSTEM.

The microscope parameters for QSTEM were as follows: 300 kV high voltage; -1.7 nm defocus; 1000 µm spherical aberration; 19.6 mrad convergence angle; 5x108 brightness ($A/cm^2sr^{-1}$); TDS (thermal diffuse scattering) on; 0.6 eV dE; 1µs dwell time; 300 K

temperature; no beam tilt. The values for the detector geometry, specimen thickness and source size were 24 to 85.7 mrad, 19 nm and 0.07 nm, respectively.

#### 4.2.3.3 Quantification

Using the well characterized titanium silicon carbide sample different cross section models should be applied and tested on the selected stoichiometry.
To quantify the $Ti_3SiC_2$ reference material, cross section values were taken from the hydrogenic model, as well as from the FEFF code. Values from the hydrogenic model include the use of the preset and the optimized screening constants.
Therefore the deviation of the nominal Si/C ratio of 0.5 has been compared using the cross sections and net intensities of the evaluated Si-K and C-K edges acquired with an incident beam energy of 300 keV, a convergence angle of 6 mrad and a collection angle of 6.5 mrad which would lead to an effective collection angle of 4.9 and 6 mrad for the C-K and Si-K edge, respectively.
Quantification was performed by the integration of cross sections and net intensities over an energy window of 100 eV starting at the threshold energy (TE).
Furthermore the continuum region, above the spectrum's fine structure oscillations, of the EEL spectrum was selected for quantification: the energy window was spanned for 95 eV starting at 334 eV for the C-K edge and for 153 eV starting at 1918 eV for the Si-K edge. In the continuum range hydrogenic cross sections with the preset screening values lead to an accordance of 3.5% with regard to the nominal elemental ratio; for the FEFF and hydrogenic cross sections with optimized screening constants, as described in section 4.1.1, accordance accounts below 1%. Using an integration window that starts at the threshold energy, the accordance with the nominal values is between 33% and 35%, when calculated with hydrogenic cross sections and 29%, when applying the FEFF cross section.

**Table 5** Deviation from nominal Si/C ratio in %

| energy window | hydrogenic preset | hydrogenic opt | FEFF | scaled cross section |
|---|---|---|---|---|
| in the continuum | -3.543 | 0.002 | 0.154 | - |
| starting @TE for 100 eV | -35.387 | -32.949 | -28.768 | 0.154 |

The definition of „continuum“ and the energy window size as described in the text above.

In addition to these results experimental cross sections have been synthesized. Therefore, the net experimental spectrum was scaled with the FEFF cross section, determined in the

continuum (Table 5). This results in a perfect cross section that also accounts for the fine structure.

Further, cross sections have been calculated using the EDX ζ-factor conversion. Considering that EELS and EDXS analysis are primarily used for the quantification of light and heavy elements, respectively, Kothleitner et al. (2014) has demonstrated an approach to combine EDX ζ factors with EELS cross sections. The cross section is linked to the ζ-factor via the mass thickness. Merging Equations 31 and 26 leads to the product of the ζ-factor and the EELS cross section σ:

$$\boldsymbol{\sigma_A} = \left(\frac{\boldsymbol{I_A^E * C_A}}{\boldsymbol{I_{0,A}^E * I_A^X * A_A}} * \frac{\boldsymbol{AW}}{\boldsymbol{N_{AV}}} * \boldsymbol{D_e}\right) / \boldsymbol{\zeta_A} \tag{34}$$

To obtain the ζ-factors for Ti, Si. C, EELS and EDX intensities have been acquired consecutively of the same spots. EDX Intensities have been measured by fast scanning over a 40x40 nm sized sample region to reduce beam damage. Actually, the acquisition of spectrum images (SI) would have been favorable along with simultaneous EELS acquisition. Unfortunately, the used version of DM provided wrong values of the EDX SI acquisition times. Therefore the “scanning window” approach was used. Utilizing the 4 detectors Super-X system allowing to acquire the 4 spectra simultaneously and summing up their intensities. According to Kraxner et al. (2017) tilting should be applied on the sample by the means of +15° for quadrant 1 and 2, and -15° for quadrant 3 and 4, respectively to avoid absorption within the sample holder.

Within this thesis, the measurements were acquired for each detector separately, which makes sense bearing in mind that the detectors (Q2, Q3, Q4) sometimes stop counting if the count rate drops below a threshold value. This value is different for each detector and highest for detector 3.

Off-axis, non-channeling conditions have also been ensured. The subsequent extraction of X-ray intensities was performed by using the top-hat filter routine in DM. The relative thickness t/λ (according to Equation 3) has been measured before and after each EDX analysis.

The electron dose has been measured with a counts-to-electron-conversion-calibrated CCD before and after each measurement. Three ζ-factor measurements have been averaged to get a statistic ζ-factor for each quadrant.

Prior to ζ factor calculation the density and the thickness of the sample had to be determined.

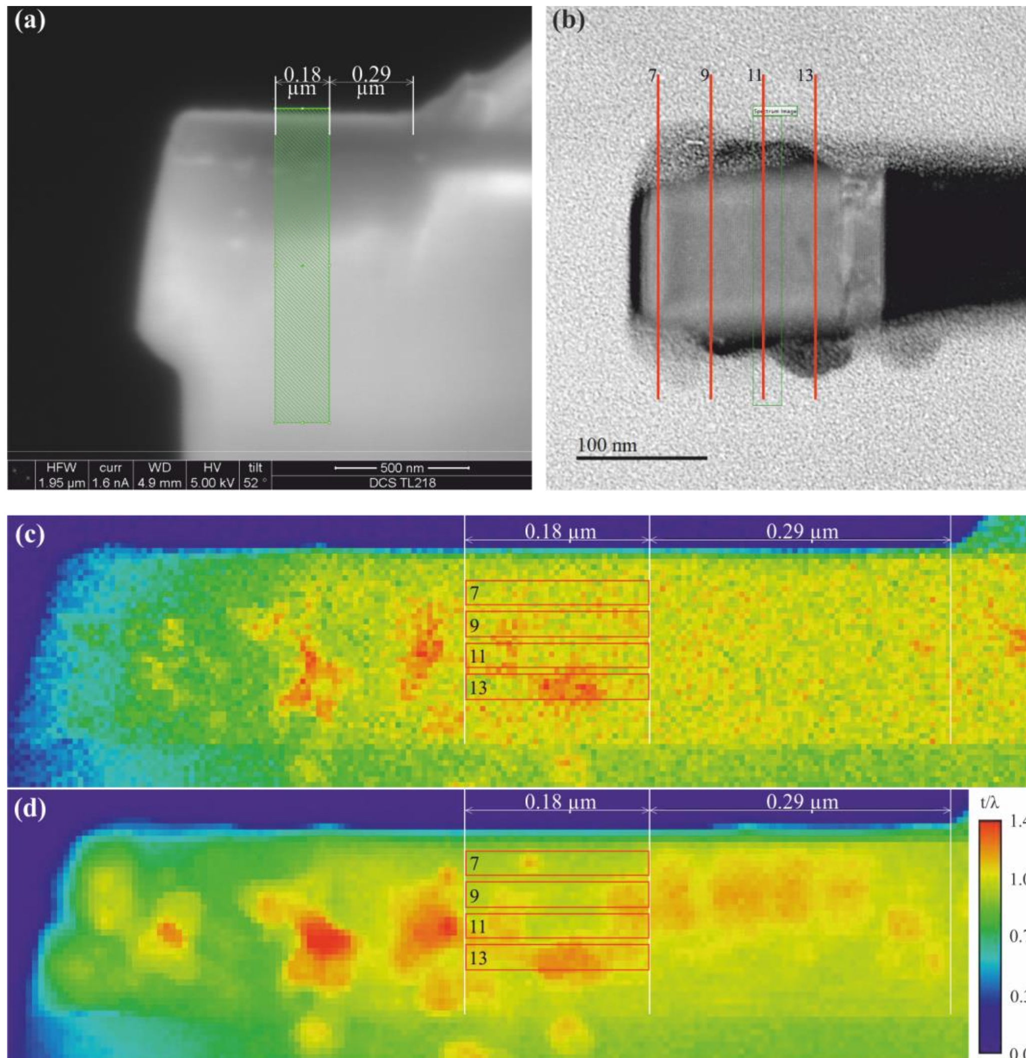


**Fig. 53** Determination of the specimen's thickness. (a) re-embedded FIB-cross-section overview image. (b) cross-section with indication of the measured areas. (c) initial t/λ map. (d) final t/λ map.

The density of 4.5 g/cm³ was taken from the literature (Barsoum, 2000). The inelastic mean free path of the investigated area was determined by relating t/λ maps, acquired before (Fig. 53(c)) and after (Fig. 53(d)) all the ζ-factor experiments of the whole specimen, to its absolute cross sectional thickness.

For thickness measurement the FIB lamella that was used for the ζ-factor measurements was re-embedded (Fig. 53(a)) and a FIB cross section cut (Fig. 53(b)) has been prepared. The width of this cross section can be directly measured. Fig. 53(b) clearly shows the carbon contamination and can be related to the t/λ map after all the measurements.

The thickness line profiles, shown in (Fig. 53(b)) are identical with the t/λ slices (Fig. 53(c,d)). A set of 4 λ values has been calculated for the initial and contaminated thickness respectively. When averaged, a λ of 155 nm accounts for the MAX phase specimen. Subsequently ζ-factors from EDX measurements (Fig. 54(d)) were converted into EELS cross sections (Fig. 54(a-c)). Fig. 54(d) shows that the EDX spectra indicate peak overlaps for light elements at E< 1 keV.

The absorption corrected ζ-factors of all 4 detectors have been averaged and converted into EELS cross section as described by Kothleitner et al. (2014) using Equation 34.

The cross sections obtained in this way where compared to FEFF and conventional hydrogenic cross sections of the EXELFS region using integration windows of about 100 eV. Table 3 reveals that, cross sections per element deviated less relative to FEFF than to SIGMAK, L3 hydrogenic values calculated with the preset screening factor.

A good measure for the quality of the calculated ζ-factor is the "reversed density". After re-arranging Equation 31 for the density, the input of the calculated ζ-factor should give density values close to the bulk density (ρ) of the MAX phase of 4.5 g/cm³, when the absolute thickness is known from EELS t/λ maps with experimental determined λ. The deviation from the nominal for all three elements was below 5%, as shown in Table 6.

**Table 6** Absorption corrected ζ-factors ($\zeta_{ABS}$) for the elements C, Ti and Si were converted into EELS cross sections (σ) and compared with FEFF/SIGMAK,L3 values. Calculated bulk densities, are also given.

| Edge | $\zeta_{ABS}$ average (g/barn) | $\sigma_{\zeta}$ average (barn) | $\sigma_{\zeta}$ deviation (%) FEFF | SIGMAK,L3 preset | $\rho_{average}$ (g/cm³) |
|---|---|---|---|---|---|
| C-K | 1.26E-22 | 2816.3 | 6.4 | -3.7 | 4.7 |
| $Ti-L_{2,3}$ | 1.35E-22 | 4505 | 2 | -10.9 | 4.7 |
| Si-K | 8.21E-23 | 79.7 | -8.5 | -19.2 | 4.7 |

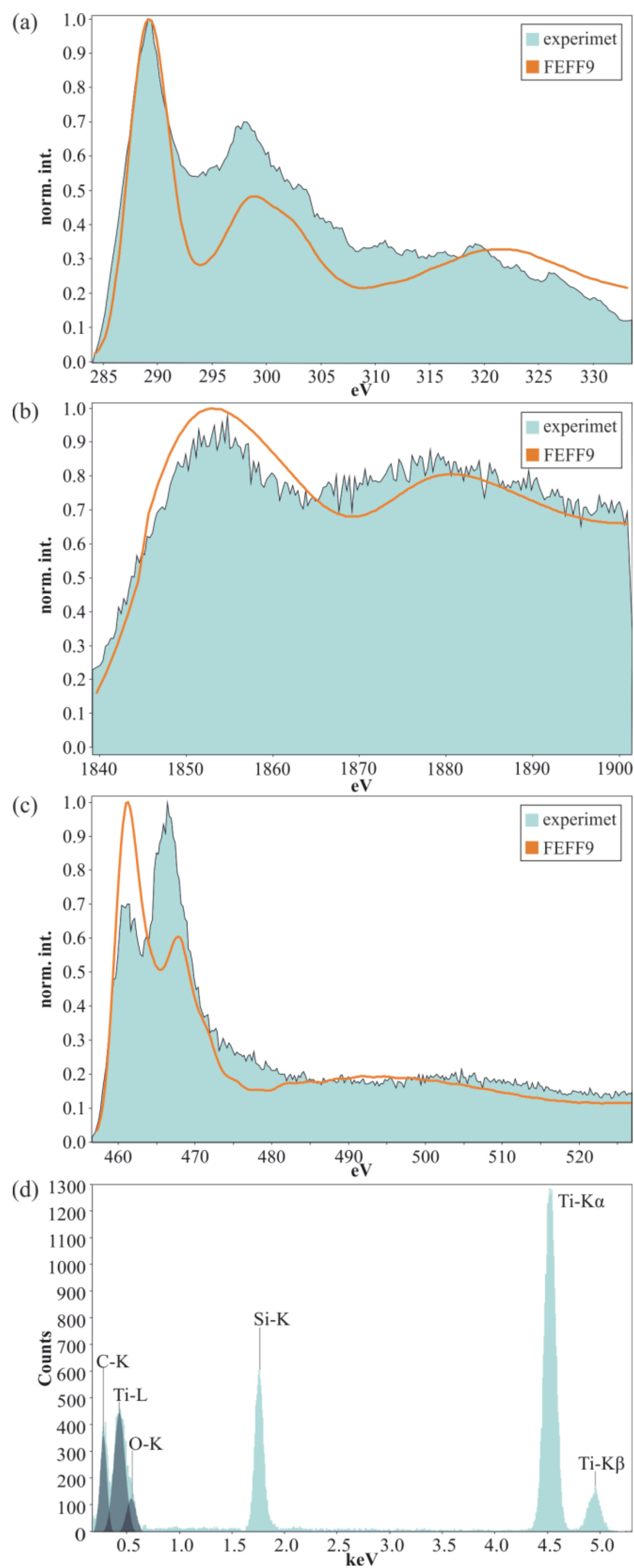


**Fig. 54** Experimental EELS edges of $Ti_3SiC_2$ in comparison with a FEFF code simulation (a) C-K, (b) Si-K and (c) Ti-$L_{2,3}$. (d) EDS spectrum.

### 4.2.4 Titanium carbonitride

The situation is more complex when light elements (e.g. carbon and nitrogen) can be located at the positions of the unitcell, as for the systems explained previously.

The sample consists of a $TiC_{1-x}N_x$ coating on a cemented tungsten carbide insert. The coating is about 5µm thick and the target of investigation. Single grains are elongated and about 0.5 x 1 µm.

Previous to the TEM investigations XRD measurements have been carried out, whose outcome will be portrayed before discussing the results from the diffraction and EELS experiments.

#### 4.2.4.1 XRD on Ti(C,N)

For phase identification XRD measurement is a common tool to use. Attempts have been made to identify the stoichiometry of the coating by comparing the diffractogram with patterns obtained from the international centre for diffraction data (ICDD) via powder diffraction files (PDF2002).

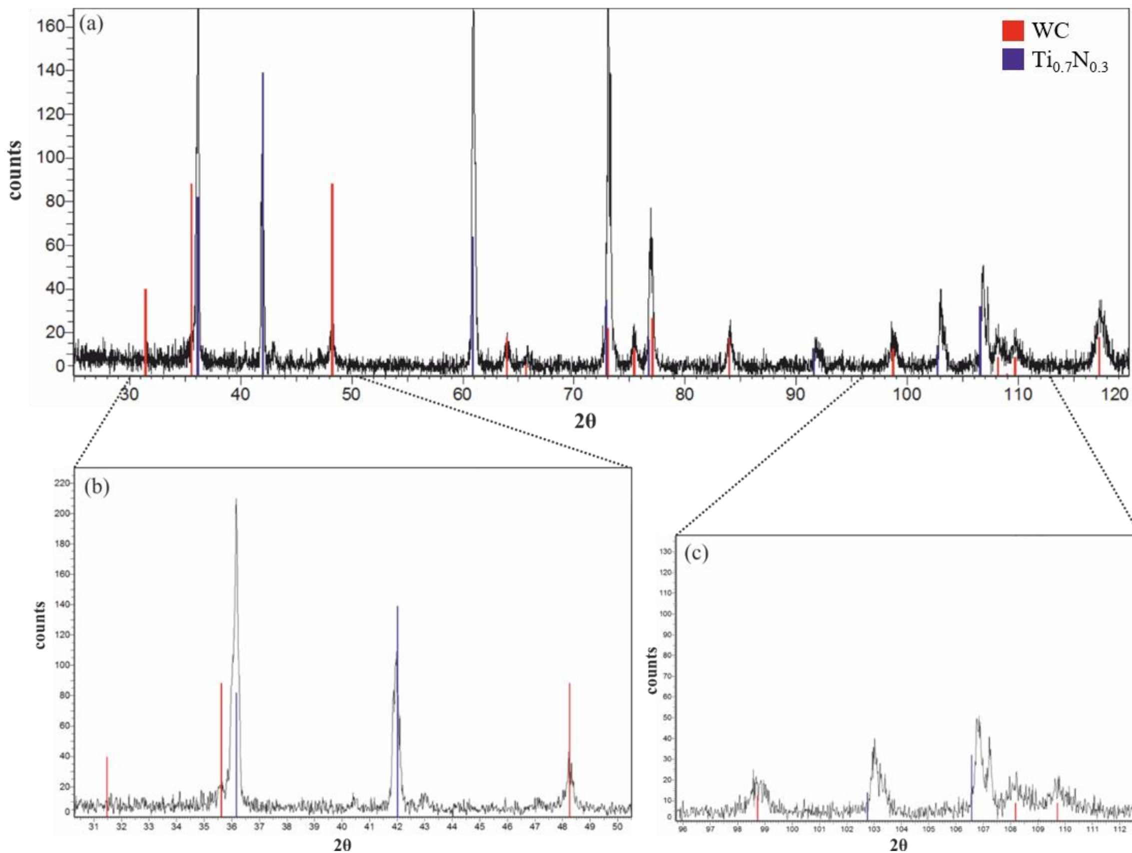


**Fig. 55** (a) X-ray diffraction pattern of WC and $TiC_{0.7}N_{0.3}$ overlaid by high quality data sets in red and blue for the before mentioned phases respectively. Magnifications are shown for (b) $2\theta$ 31-51° and (c) $2\theta$ 95-113°.

Interpretable data from XRD is usually gained from a homogeneous powder. As the coating is very thin, crushing and powdering the bulk sample with the coating on top, only the bulk material will be displayed in the diffractogam or, more precisely, overly the coating reflexions. Furthermore, the cemented carbide bulk material is difficult to be powdered in an agate mortar. Compromising this, a ca. 1 mm thick slice of the bulk with the coating on top was cut off using a diamond wire saw, thus obtaining a plate that can be put on the sample carrier for performing the experiment.

Subsequent the pattern was compared to PDF2002 datasets, as elucidated in Fig. 55. For the WC, pattern number PDF 25-1047 was used as a reference (red), while for the $TiC_{1-x}N_x$, pattern number PDF 42-1489 (blue) was used. Unfortunately, the only stoichiometry available in the PDF2002 dataset was $TiC_{0.7}N_{0.3}$. At a first glance, the fit for the two datasets looks pretty well (Fig. 55(a)), but upon closer inspection a TiCN peak shift (~0.3°), especially in the high $2\theta$ regime (small d-spacing) can be witnessed (Fig. 55(b,c)). One possible explanations could be that if all the peaks are systematically too low in $2\theta$ the sample is below the focus of the diffractometer (Allmann, 2003). As the shift is associated with one phase only, evidence of a different stoichiometry, other than the PDF data file used when compared to the experiment, is more feasible.

In the following chapters, TEM techniques as outlined in Fig. 46 are employed to determine the structure and composition of the $TiC_{1-x}N_x$.

#### 4.2.4.2 TEM imaging on Ti(C,N)

To obtain an overview of the sample HR-images have been acquired in the TF 20 microscope (Fig. 56). The insert shows a FFT that suggests a cubic lattice. Twinning is

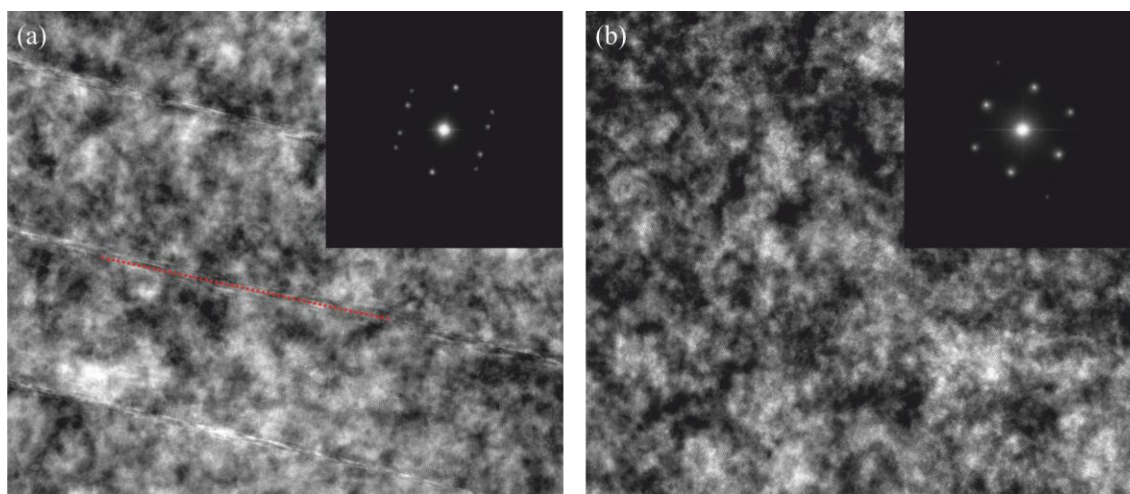


**Fig. 56** HRTEM images of TiCN showing different parts of a crystal: (a) the twinning zone (red mark) (b) further away from twinning zone. Inserts shows the corresponding FFT of the images.

also observed, indicated by the red line in Fig. 56(a). What comes to mind is the speckled contrast in the images, originating from a lattice distortion.

Darkfield (DF) imaging might bring useful information about defects and faults. Therefore a random grain (Fig. 57(a)) has been selected and different hkl reflections were used for DF imaging (Fig. 57(b-d)). The information gained is sparse, however revealed fine scale, modulated contrast with dark and bright blobs arising from different reflections, yet without any preferential elongation direction of these “speckling blobs”.

A possible cause could be variations in the lattice parameters originating from compositional variations related to displacement of atoms. The origin of this effect, however, remains unclear. It possibly could arise from the CVD manufacturing process itself or from particle impingement during preparation or measurement.

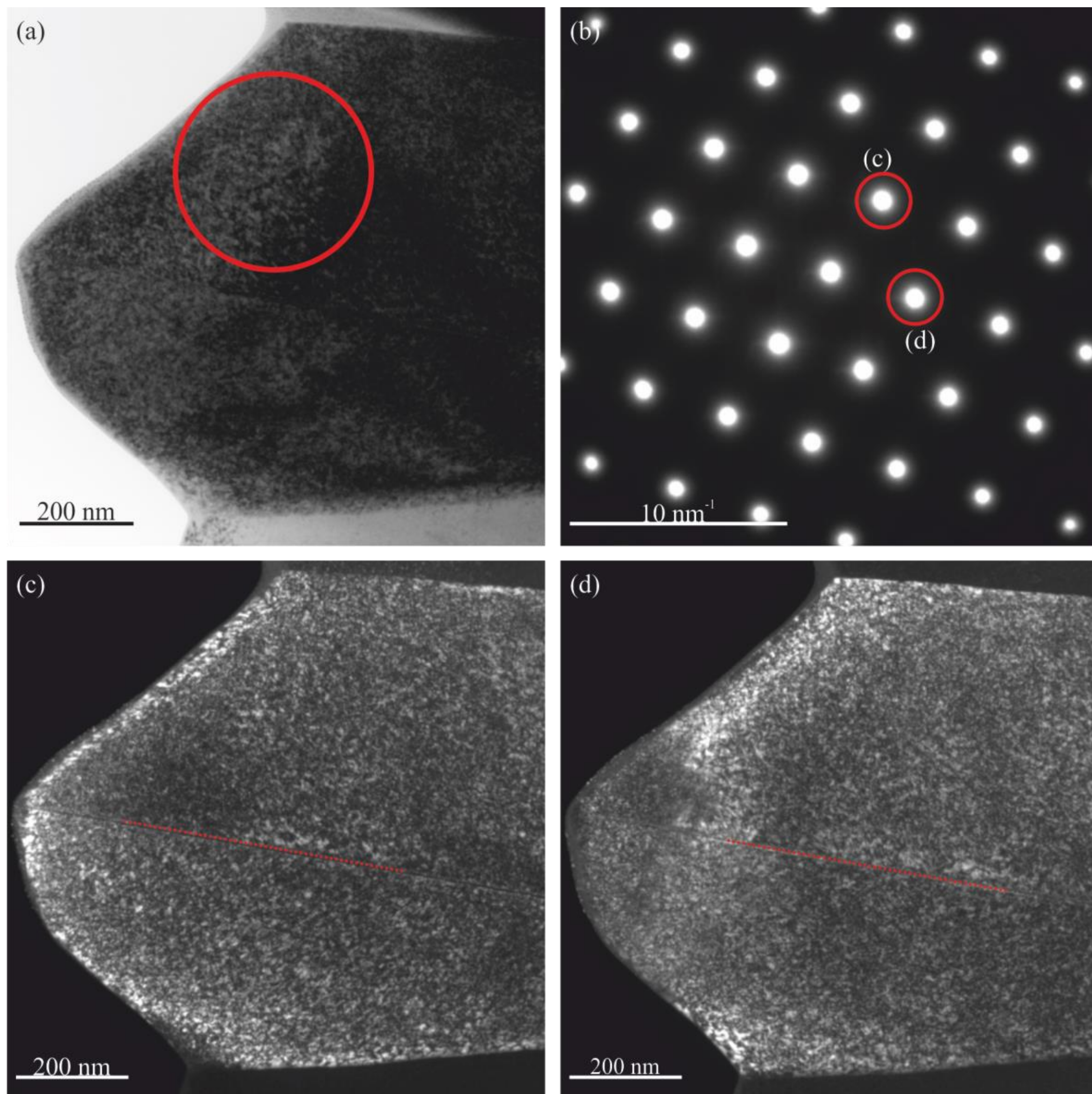


**Fig. 57** (a) BF image of a TiCN grain in ZA that shows speckled contrast, the circle marks the investigated area for (b) SAED where c and d denotes hkl reflections for DF images (c,d).

### 4.2.4.3 SAED and CBED investigations on Ti(C,N)

Not only the Bragg diffraction spots expected from the perfect crystal structure can be seen in an ED patterns but also additional spots and streaks can occur (Reimer, 1984). SAED patterns have been acquired using the TF 20 microscope. The extent of the investigated area depends on the size of the SA aperture. The smallest aperture has a diameter of 10 µm leading to an area on the sample itself of about 350 nm. Twinning can be again envisioned on the SAED patterns (Fig. 58(a)) resulting from a mirror reflection of the crystal structure about special lattice planes as well as creating diffuse streaks in the diffraction pattern extending from one Bragg spot to another are observed (Fig. 58 (b)). The appearance of streaks indicates the presence of crystal defects that could be different types of precipitates, dislocations as well as twins and staking faults (Asadabad and Eskandari, 2016; Reimer, 1984).

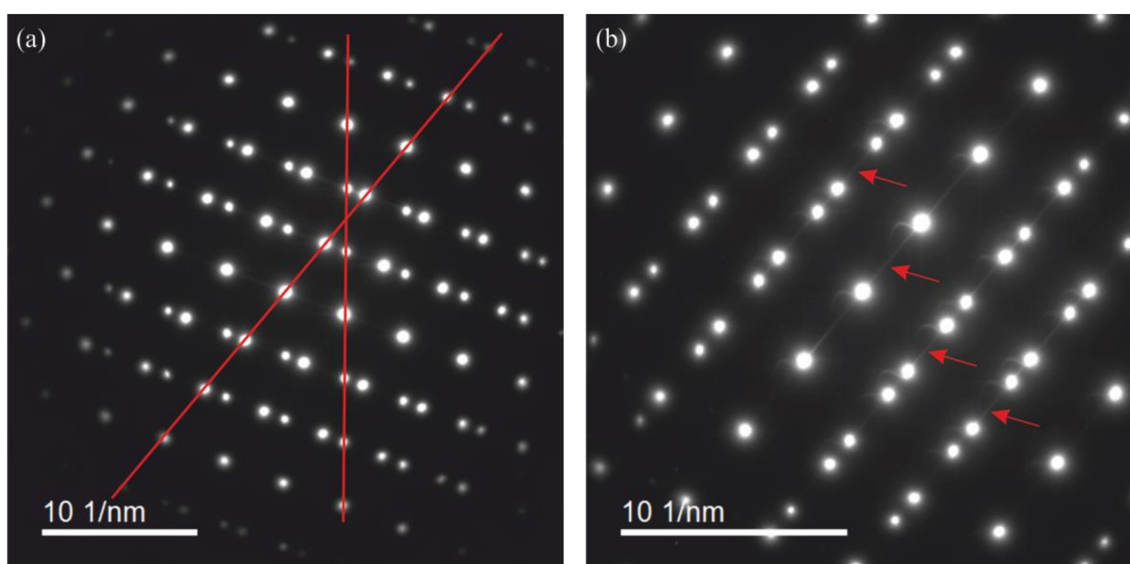


**Fig. 58** (a) SAED pattern showing twinning and (b) streaks indicated by red arrows.

A smaller volume on the sample can be observed by CBED that uses a convergent beam, which is much smaller than the smallest area selected using SAED. In the case of the TF 20 microscope the area observed with CBED using "spotsize" 3 and a $C_2$ aperture of 50 µm is about 4 nm. As mentioned before HOLZ lines within the CBED pattern can be indicative for different stoichiometries. Using the JEMS program HOLZ line patterns were generated using ICSD structural datasets No. 181784, 181785 and 181786 for $TiC_{0.25}N_{0.75}$, $TiC_{0.5}N_{0.5}$ and $TiC_{0.75}N_{0.25}$ respectively. As one can see in Fig. 59, they obviously show distinct patterns.

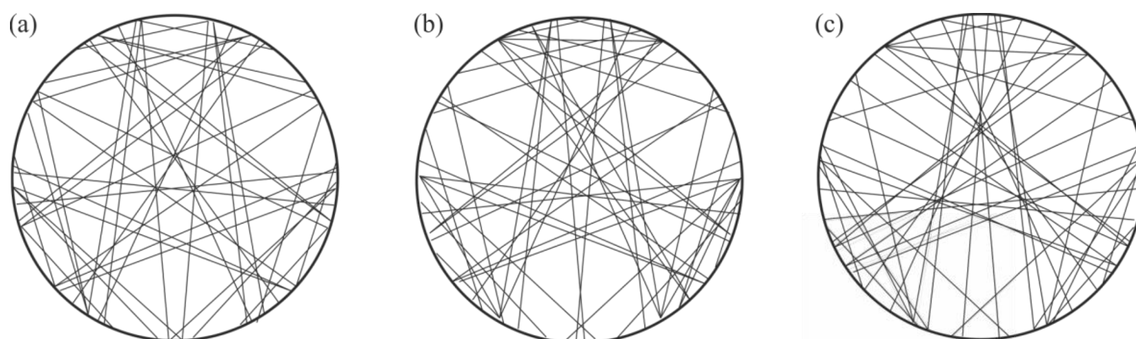


**Fig. 59** Simulation of HOLZ lines with JEMS for (a) $TiC_{0.25}N_{0.75}$, (b) $TiC_{0.5}N_{0.5}$ (c) $TiC_{0.75}N_{0.25}$ [111].

However, even if the simulations predict to distinguish different chemistries with this method, HOLZ lines are not visible, possibly because of the "speckled texture" or due to the beam sensitivity of the sample as the features within the CBED disks fade out within seconds of observation (Fig. 60).

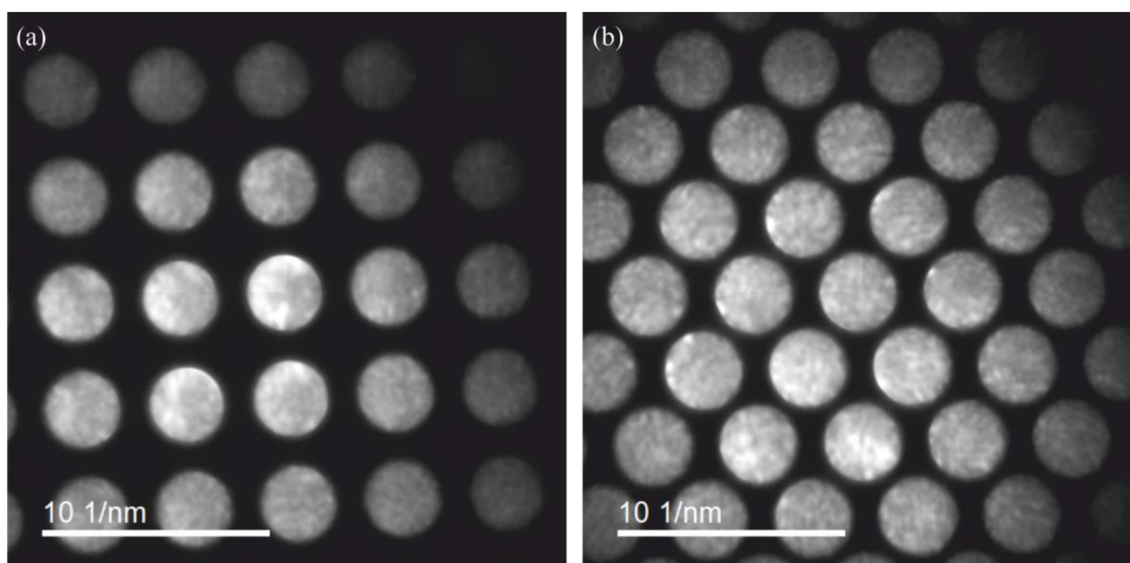


**Fig. 60** Blurred and faint HOLZ line feature

#### 4.2.4.4 ADT experiment on Ti(C,N)

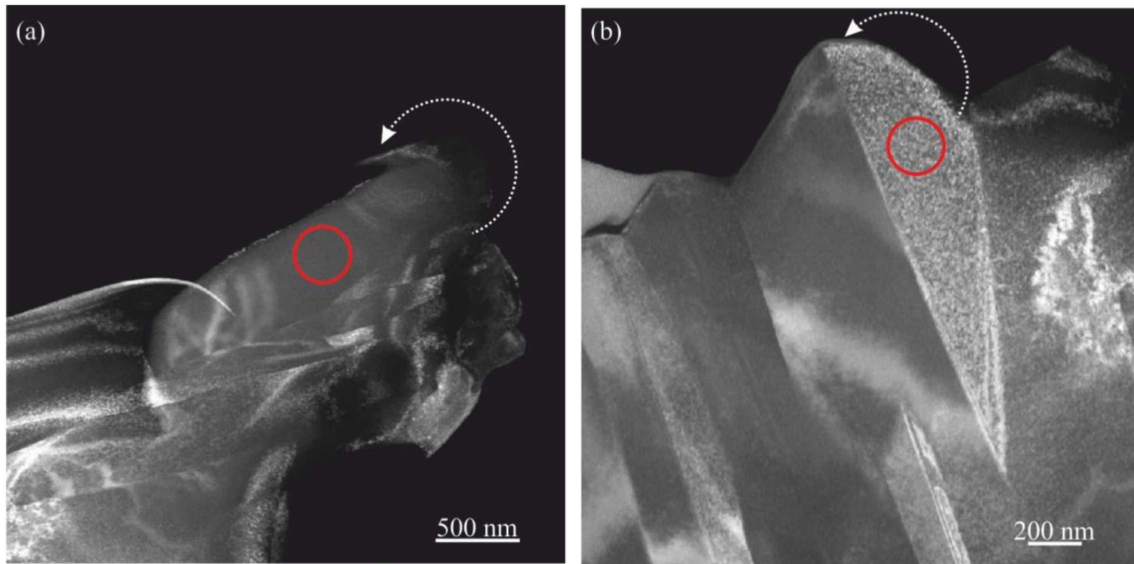


**Fig. 61** HAADF images of (TiC,N) crystals (a) undistorted appearance (2) specled appearance. The probed volume represents about half of the indicated red circle.

Two crystals were subject to ADT experiments. The first one looks undistorted (Fig. 61(a)) whereas the second one (Fig. 61(b)) shows "speckling blobs". The crystal was tilted from -39°-60° with a tilting step of 1°. Precession was turned on with a precession angle of 1°. The beam diameter was 75 nm using "spotsize" 6 and a 10 µm $C_2$ aperture. The determination of cell parameters leads to $a$=0.422, $b$=0.422, $c$=0.427 nm and $\alpha$=90.0°, $\beta$=89.2°, $\gamma$=89.7° after reconstructing the 3D volume in reciprocal space (Fig. 62). This is in good accordance with data from the literature ($TiC_{0.3}N_{0.7}$: $a$=0.426441; $TiC_{0.7}N_{0.3}$: $a$=0.429709) (Guilemany et al., 1992).

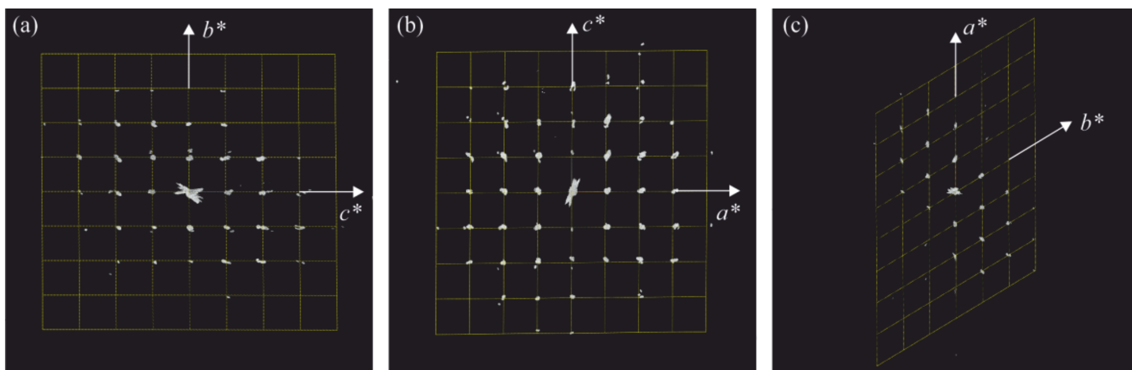


**Fig. 62** Reconstructed 3D reciprocal space of Ti(C,N) viewed along the main directions (a) [100], (b) [010] and (c) [001].

Using SIR2014, the potential representation of the cell in Fig. 63(a), shows that the positions of the light elements were identified, however allocation and sensitivity concerning the occupancies and fractional amounts of carbon and nitrogen could not be given, which indicates the limitation of the technique.

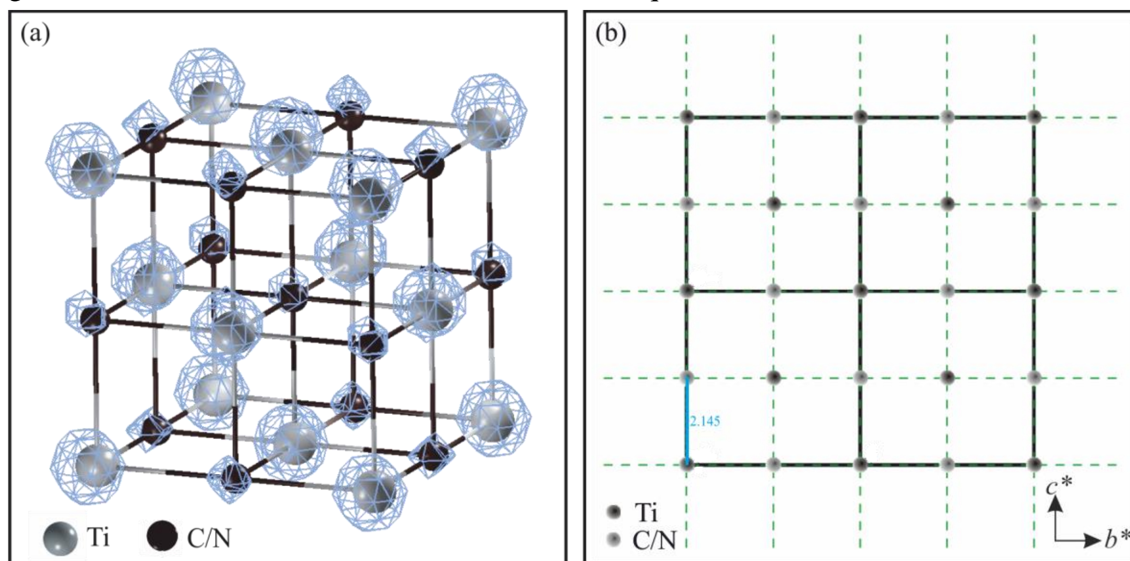


**Fig. 63** SIR2014 assignment of the atom positions: (a) electron potential map, (b) crystal structure along [100].

An ADT tilt series was also acquired from a second crystal (Fig. 61 (b)) from -50°-60° using the same microscope settings as before. As mentioned before all indications are that the crystal structure is distorted, thus an interpretable structure solution cannot be given.

#### 4.2.4.5 ELNES measurements on Ti(C,N)

ELNES measurements have been carried out on the TF 20 microscope at 200 keV, a beam convergence of 12.4 mrad and a collection angle of 16.5 mrad (giving an effective collection angle of 13.9 mrad.). Spectra were obtained using a non-monocrochromatic probe. The spectral resolution can be given by the FWHM of the zero-loss peak to be 1.5 eV. Measured spectra were compared to ELNES simulations carried out with FEFF9 using the experimental parameters (Fig. 64).

Simulations have been performed using data from cubic TiC (ICSD code: 159871) for the C-K and Ti $L_{2,3}$ edge and cubic TiN (ICSD code: 644778) for the N-K edge.

Instrumental broadening was added to the simulations according to the FWHM of the zero-loss using the vicorr module within FEFF 9. In Fig. 64 the unbroadened spectra are displayed as inserts to elucidate the effect of instrumental broadening. Simulations, for comparison, have been performed excluding and including a core hole. The core hole was calculated according to the “final state rule”. This means that an excited atom is placed

in a host lattice of atoms in their ground state, its electronic structure gets calculated within an independent particle framework, and then the EEL spectrum gets calculated (Jorissen, 2007). Following Jorissen (2007), owing to the slow core hole decay process, the lifetime of the resultant excited state is typically $10^{-14}$ to $10^{-15}$ s. Outer electronic states get bounded more strongly due to the attractive core hole potential thus making them contract spatially and lowering their binding energy.

What can be seen throughout Fig. 64 is, that in simulations including a core hole, the transition probability tends to shift down towards the edge threshold, at least for K-edge transitions. Experimental C-K and N-K EELS fine-structure details match the FEFF simulated data quite well. Some offset, however, is shown concerning the magnitude of some intensities as well as the exact energetic alignment (Fig 64(a,b)). The two dominant peaks show a separation by about 10 eV, confirming the structure as cubic, also known from different EELS measurements on carbides and nitrides of transition metals (Hofer et al., 2001).

Certain many-body effects cannot be described by independent particle calculations (final state rule core hole), such as deviations in the intensity ratio of the $L_2$:$L_3$ white lines ($L_{2,3}$ branching ratio) (Nesvizhskii and Rehr, 1999). No solution has yet been found to address this issue (Jorissen, 2007).

Although the exact branching ratio is obscured, this should not matter much to the overall integrated intensities. Further it can be stated that referring to L-edges, the no core hole simulations display the experiment better as can be seen in Fig. 64(c).

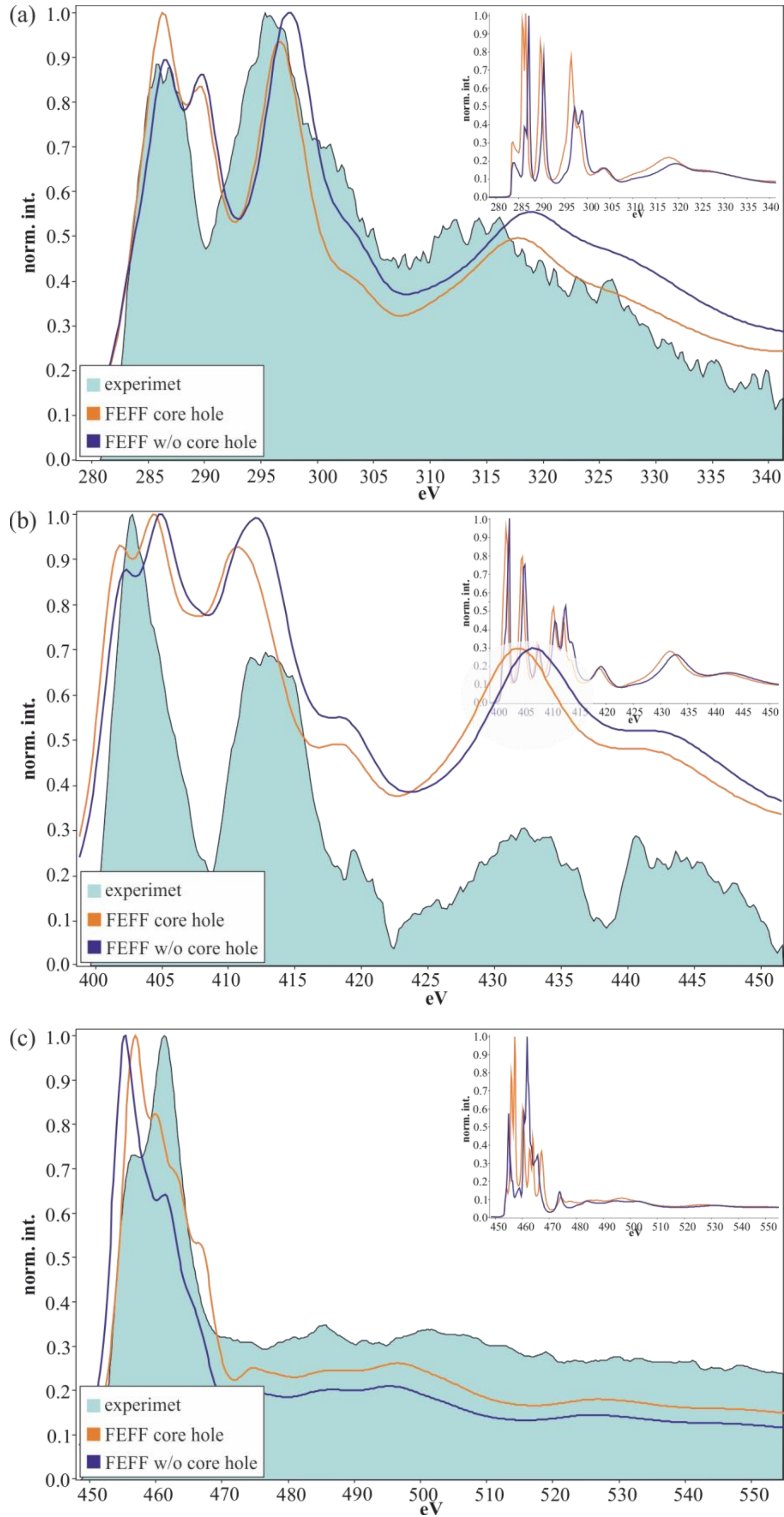


**Fig. 64** Experimental EEL spectra compared to FEFF9 simulations for (a) C-K, (b) N-K and (c) Ti-$L_{2,3}$ edges. The insert shows the unbroadened simulations.

### 4.2.4.6 EELS quantification on Ti(C,N)

As electron diffraction data did not yield any results on the stoichiometry of the titanium carbide compound, yet, EELS elemental analysis should give an insight to reveal the relative concentration of the anions.

EELS quantification requires the edges' spectral intensity ratios to be linked via the reciprocal integrated cross sections to obtain elemental atomic ratios.

Using the model based fitting approach implemented into GATAN's DM 3.23 (Thomas and Twesten, 2012) spectral intensities for C-K, N-K and Ti-$L_{2,3}$ have been extracted.

As shown in Fig. 65 the fit region (green window) was chosen to range from 260 to 615 eV. Thickness related effects due to multiple scattering were removed from the EEL spectrum via the deconvolution with the low-loss spectrum that was acquired simultaneously, shown as an insert in Fig. 65(a).

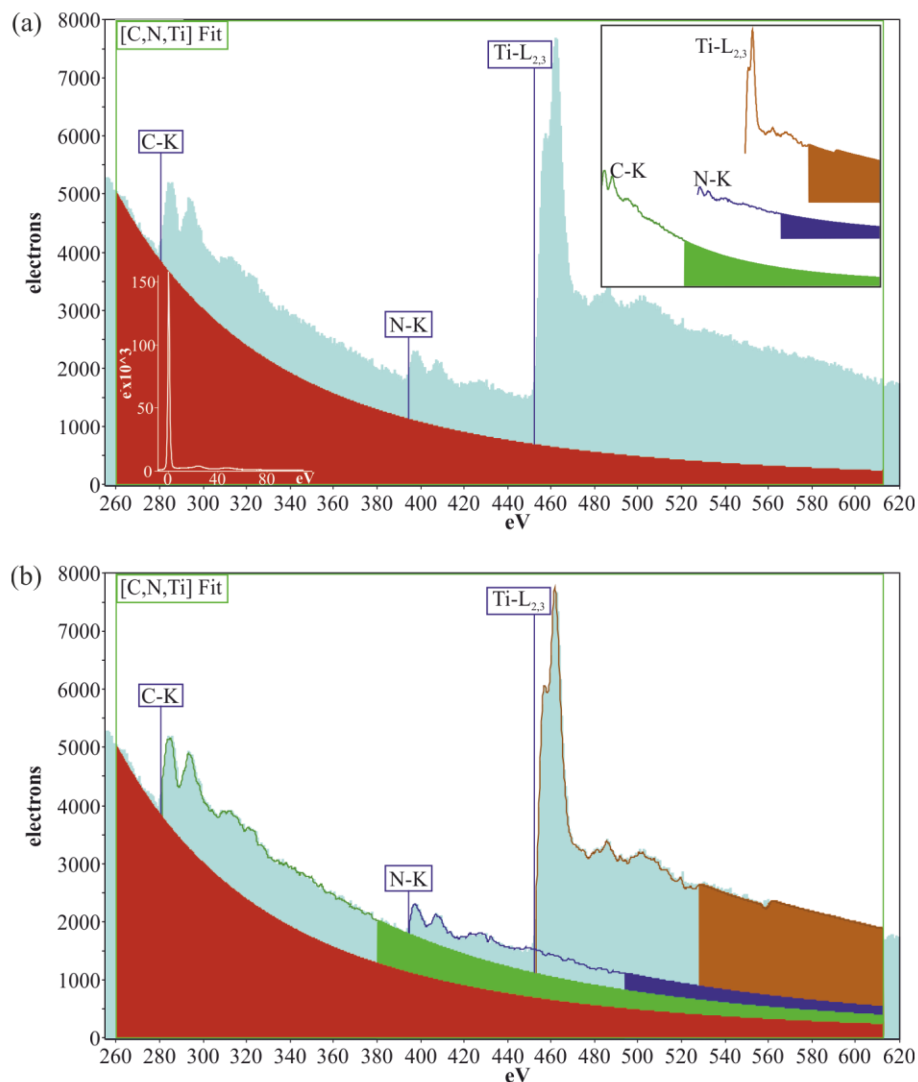


**Fig. 65** Depiction of the model based fitting approach (Thomas and Twesten, 2012) (a) shows the Ti(C,N) spectrum with the fitted background and the low loss signal. The insert shows the signal extraction. (b) Modelled spectrum with overlapping edge intensities.

Further the spectrum gets decomposed into the three present edges combining hydrogenic cross sections models with the experimental ELNES (insert in Fig. 65(a)). As is shown in Fig. 65(b), even the intensities for overlapping edges can be extracted. The dark colors mark the portion of the net intensities for the case of excluded ELNES.

The quantification has been carried out for two types of signal integration windows commonly used in EELS quantification. The first integration window was set over a range of 50 eV, from the edge threshold energy onward, while the second was set over a range of 100 eV offset by 100 eV from the edge threshold. Thus, deviations upon the concentration results are predictable as they are dependent on the used integration conditions (Table 7). Moreover, even within a particular setup depending on the utilized screening factor or when using FEFF cross sections, the cross-sectional values varied by 20% and 30% for carbon and nitrogen.

Hydrogenic cross sections were obtained with screening factors for 0.3 in reference to original approximations by (Zener, 1930) and the optimized value of 0.8, as described in section 4.1.1. The outcome of the results is summarized in Table .

Nonetheless, depending on the utilized cross section model, the atomic ratio of C/N amounted to ~1.9 and ~1.1 for 50 and 100 eV wide windows, respectively.

This, however, suggests two compounds of the type $TiC_{\sim 0.7}N_{\sim 0.3}$ and $TiC_{\sim 0.5}N_{\sim 0.5}$.

The open question, however, concerning the carbon - nitrogen ratio within the $TiC_{1-x}N_x$ solid solution could be assigned based on the considerations discussed in section 4.1.1, setting x to 0.47 with a screening factor of s:0.8.

**Table 7** EELS concentrations for carbon and nitrogen as a function of cross sections (SIGMAK3 / FEFF9), hydrogenic model screening factors and edge integrals / integration offsets.

| hydrogenic screeinig factor | Δ 50 eV from threshold | | | Δ 100 eV, 100 eV offset | | |
|---|---|---|---|---|---|---|
| | C/N atomic ratio integral | C stoich. coeff. | N stoich. coeff. | C/N atomic ratio integral | C stoich. coeff. | N stoich. coeff. |
| 0.3 | 1.85 | 0.65 | 0.35 | 1.06 | 0.51 | 0.49 |
| 0.8 | 1.92 | 0.66 | 0.34 | 1.11 | 0.53 | 0.47 |
| FEFF | 1.83 | 0.65 | 0.35 | 1.08 | 0.53 | 0.48 |

## 4.3 Reference Spectra

As it could be shown that multiple scattering simulations can help for EELS compositional analysis, we have built up a database for common K and L edges. Therefore, simulations have been performed with the help of FEFF 9 for a set of different operating conditions to be compared with experimental data. Further $L_{2,3}$ edges have been simulated with and without corehole. The files can be opened using the FELMI/Zfe Spectra Viewer (http://felmi-inet/specview/), accessible for internal use (Fig. 66).

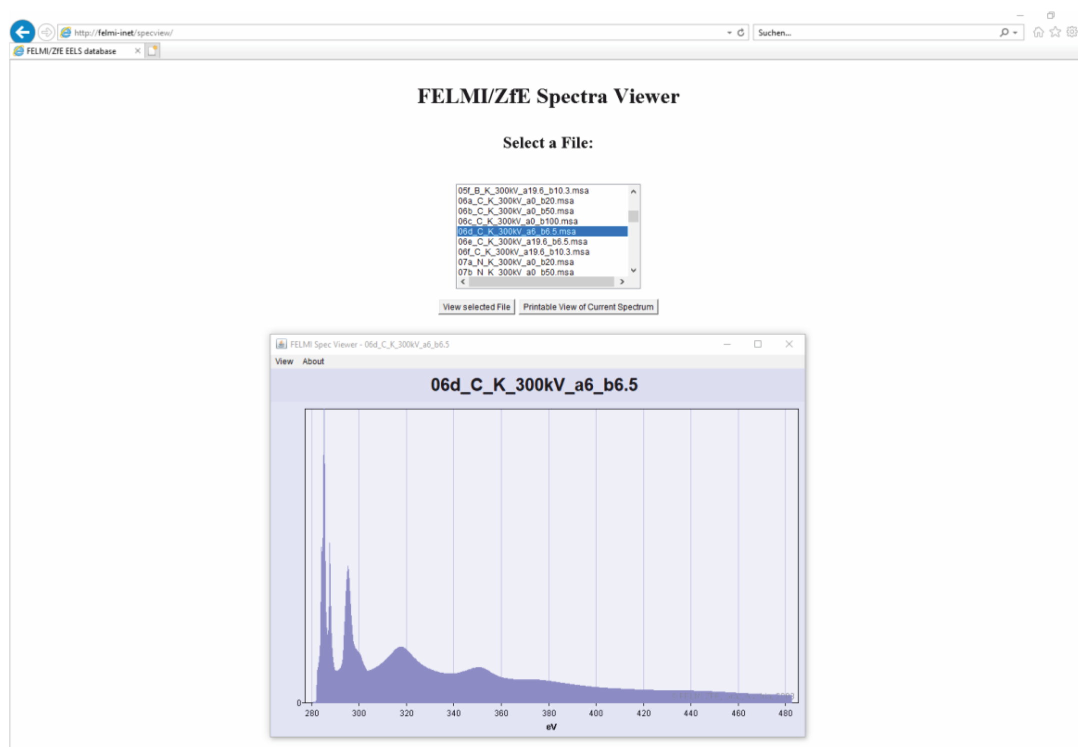


**Fig. 66** Snapshot of the online view of the Java-Applet „Spectra Viewer“

# 5 Conclusions

This work shows that combining precession electron diffraction tomography along with analytical techniques, including EELS and EDX and respective simulations, can provide a more complete picture on the characterization of materials in particular also useful for those used in the hard metal manufacturing industry. The workflow (see chapter 4.2, Fig. 46) is designed in such a way that all steps can be performed on a (S)TEM instrument. This on the one hand minimizes the time-to-result, on the other hand adds consistency to electron microscopic characterizations.

With the help of the WC sample it could be demonstrated that NEDT experiments are not only a highly potential tool for structure determination, but can be also seen as the basis for *ab initio* ELNES simulations. This is done by converting hkl crystallographic data into an input file for FEFF simulations, thus linking structural and analytical data.

Multiple scattering calculations were used to confirm the studied phases and their crystallographic structure by comparing the EELS ELNES region. Furthermore the issue was raised upon the accuracy of hydrogenic cross section parameters used by performing SIGMAK3 calculations. By comparing FEFF9 simulations to hydrogenic cross sections it is obvious that modification of the hydrogenic screening parameters is required. Instead of using the single default screening parameter of 0.5 in SIGMAK3 the parameters should be adjusted in consideration of light and heavy elements and the integration area.

The structure of the MAX phase could be confirmed as $Ti_3SiC_2$ using HR-HAADF images as well as SAED pattern, both combined with simulation techniques. Thus, considering $Ti_3SiC_2$ as a well-defined reference material, upon quantification, a screening parameter of 0.8 for integration windows in the EXELFS region yielded better matching concentrations across atomic numbers $6<Z<14$. This analysis also holds against EDX spectra from the same spots and determined ζ-factors, subsequently converted into EELS cross sections.

The $TiC_{1-x}N_x$ sample, was more difficult with respect to the carbon/ nitrogen ratio. Yet, with bearing in mind to adjust the screening parameter to 0.8, the phase can be addressed to as $TiC_{0.53}N_{0.47}$.

FEFF fine structure simulations of K-edges are in good accordance with experimental spectra. $L_{2,3}$ edges can be used for providing meaningful integrated cross sections, however, when it comes to the $L_2$/ $L_3$ branching ratios multiple scattering simulations fail.

Opposite to K-edge simulations, where a core-hole should be considered without doubt, $L_{2,3}$-edge simulations show a better match with experimental data when treated without a core-hole. Furthermore, an adjustment of the screening parameters within the hydrogenic model is not feasible for L-shell excitations.

The use of electron diffraction data for structure determination combined with simulated core-loss edges and adjusted hydrogenic screening constants paves the way for a more consistent analysis of chemically complex phases.

# Bibliography

Agricola, G., Bandy, M.C. (translator), Bandy, J.A. (translator), 2004. De natura fossilium (Textbook of mineralogy), Bandy, Mar. ed. Dover Publications, Mineola, N.Y.

Ahn, C.C., Rez, P., 1985. Inner shell edge profiles in electron energy-loss spectroscopy. Ultramicroscopy 17, 105–115. https://doi.org/10.1016/0304-3991(85)90003-8

Aho, A.V., Kernighan, B.W., Weinberger, P.J., 1988. The AWK programming language. Addison-Wesley, Reading, Masscachusetts.

Allmann, R., 2003. Rontgenpulverdiffraktometrie. Springer-Verlag, Berlin Heidelberg.

Amelinckx, S., 1964. Direct observation of dislocations. Academic Press, London.

Angelini, P., Sevely, J.C., Hssein, K., Zanchi, G., 1987. Evaluation of amorphous and crystalline silicon carbide by Extended Energy Loss Fine Structure (EXELFS) Analysis. In: Proc. 46th Ann. Meeting of Electron Microsc. Soe. of Am. San Francisco Press, San Francisco, 466-467.

Angseryd, J., Albu, M., Andrén, H.O., Kothleitner, G., 2011. A quantitative analysis of a multi-phase polycrystalline cubic boron nitride tool material using DualEELS. Micron 42, 608–615. https://doi.org/10.1016/j.micron.2011.02.006

Ankudinov, A., Ravel, B., 1998. Real-space multiple-scattering calculation and interpretation of x-ray-absorption near-edge structure. Phys. Rev. B - Condens. Matter Mater. Phys. 58, 7565–7576. https://doi.org/10.1103/PhysRevB.58.7565

Asadabad, M.A., Eskandari, M.J., 2016. Electron Diffraction. In: Modern Electron Microscopy in Physical and Life Sciences. InTech. https://doi.org/10.5772/61781

Bach, D., Schneider, R., Gerthsen, D., 2009. EELS of Niobium and Stoichiometric Niobium-Oxide Phases—Part II: Quantification. Microsc. Microanal. 15, 524–538. https://doi.org/10.1017/S1431927609991061

Barsoum, M.W., 2000. The MN+1AXN Phases: A New Class of Solids. Prog. Solid St. Chem 28, 201–281.

Barsoum, M. W., 2000. The MN+1AXN phases: A new class of solids: Thermodynamically stable nanolaminatesle. Prog. Solid State Chem. 28, 201–281. https://doi.org/https://doi.org/10.1016/S0079-6786(00)00006-6

Barsoum, M.W., El-Raghy, T., 1996. Synthesis and Characterization of a Remarkable Ceramic: Ti3SiC2. J. Am. Ceram. Soc. 79, 1953–1956.

https://doi.org/10.1111/j.1151-2916.1996.tb08018.x

Barsoum, M.W., Farber, L., Levin, I., Procopio, A., El-Raghy, T., Berner, A., 1999. High-Resolution Transmission Electron Microscopy of Ti 4 AlN 3 , or Ti 3 Al 2 N 2 Revisited. J. Am. Ceram. Soc. 82, 2545–2547. https://doi.org/10.1111/j.1151-2916.1999.tb02117.x

Berg, G., Friedrich, C., Broszeit, E., Berger, C., 2000. Data Collection of Properties of Hard Materials, in: Riedl, R. (Ed.), Handbook of Ceramic Hard Materials. Wiley, Weinheim.

Best, M.G., 2003. Igneous and Metamorphic Petrology, 2nd ed. Blackwell Publishers.

Blaha, P., Schwarz, K., Sorantin, P., 1990. Full-Potential, linearized augmented plane wave programs for crystalline systems. Comput. Phys. Commun. 59, 399–415.

Bragg, W.H., Bragg, W.L., 1913. The Reflection of X-rays by Crystals. Proc. R. Soc. A Math. Phys. Eng. Sci. 88, 428–438. https://doi.org/10.1098/rspa.1913.0040

Braue, W., 1990. Konvergente Elektronenbeugung in der analytischen Elektronenmikroskopie keramischer Werkstoffe - eine Anleitung für die Praxis. Materwiss. Werksttech. 21, 72–84. https://doi.org/10.1002/mawe.19900210208

Brown, I.D., McMahon, B., 2002. CIF: the computer language of crystallography. Acta Crystallogr. Sect. B Struct. Sci. 58, 317–324. https://doi.org/10.1107/S0108768102003464

Brydson, R., 2001. Electron Energy-loss Spectroscopy. Taylor & Francis, New York.

Burla, M.C., Caliandro, R., Carrozzini, B., Cascarano, G.L., Cuocci, C., Giacovazzo, C., Mallamo, M., Mazzone, A., Polidori, G., 2015. Crystal structure determination and refinement via SIR2014. J. Appl. Crystallogr. 48, 306–309. https://doi.org/10.1107/S1600576715001132

Castaing, R. 1951. Application of Electron Probes to Local Chemical and Crystallographic Analysis (Application des Sondes Electroniques a Une Methode d'Analyse Poncteculle Chimique et Cristallographique. PhD Thesis, Paris.

Champness, P.E., 1987. Convergent beam electron diffraction. Mineral. Mag. 51, 33–48. https://doi.org/10.1180/minmag.1987.051.359.04

Chatterjee, S., Chandrashekhar, S., 1996. Deposition Methods, Properties and Metal Cutting Applications of Ceramic Films. Key Eng. Mater. 114, 67–104. https://doi.org/10.4028/www.scientific.net/KEM.114.67

Cliff, G., Lorimer, G.W., 1975. The quantitative analysis of thin specimens. J. Microsc. 103, 203–207. https://doi.org/10.1111/j.1365-2818.1975.tb03895.x

Coolidge, W.D., 1913. Tungsten and method of making the same for use as filaments of incandescent electric lamps and for other purposes. Patent 1,082,933.

Cowley, J.M., 1999. Electron nanodiffraction. Microsc. Res. Tech. 46, 75–97. https://doi.org/10.1002/(SICI)1097-0029(19990715)46:2<75::AID-JEMT2>3.0.CO;2-S

Cowley, J. M., Janney, D. E., Gerkin, R., Buseck, P. R., 2000. The structure of ferritin cores determined by electron nanodiffraction. Journal of Structural Biology, 131(3), 210-216. https://doi.org/10.1006/jsbi.2000.4292

Craven, A.J., Bobynko, J., Sala, B., MacLaren, I., 2016. Accurate measurement of absolute experimental inelastic mean free paths and EELS differential cross sections. Ultramicroscopy 170, 113–127. https://doi.org/10.1016/j.ultramic.2016.08.012

Crewe, A. V., Wall, J., Langmore, J., 1970. Visibility of Single Atoms. Science (80-. ). 168, 1338–1340. https://doi.org/10.1126/science.168.3937.1338

Crozier, P. a., 1990. Measurement of inelastic electron scattering cross sections by electron energy-loss spectroscopy. Philos. Mag. B Phys. Condens. Matter; Stat. Mech. Electron. Opt. Magn. Prop. 61, 311–336. https://doi.org/10.1080/13642819008208637

Crozier, P.A., Chapman, J.N., Craven, A.J., Titchmarsh, J.M., 1987. On the determination of inner-shell cross section ratios from NiO using EELS. J. Microsc. 148, 279–284. https://doi.org/10.1111/j.1365-2818.1987.tb02873.x

Davisson, C., Germer, L.H., 1927. Diffraction of Electrons by a Crystal of Nickel. Phys. Rev. 30, 705–740. https://doi.org/10.1103/PhysRev.30.705

Donald, A.M., Craven, A.J., 1979. A study of grain boundary segregation in Cu-Bi alloys using STEM. Philos. Mag. A 39, 1–11. https://doi.org/10.1080/01418617908239271

Egerton, R.F., 2011. Electron Energy-Loss Spectroscopy in the Electron Microscope. Springer US.

Egerton, R.F., 2005. Physical principles of electron microscopy. Springer US. https://doi.org/10.1016/S1369-7021(05)71232-3

Egerton, R.F., 1996. Ul T Ramicroscopy. Micron 63, 13–15.

Egerton, R.F., Williams, B.G., Sparrow, T.G., 1985. Fourier Deconvolution of Electron Energy-Loss Spectra. Proc. R. Soc. A Math. Phys. Eng. Sci. 398, 395–404. https://doi.org/10.1098/rspa.1985.0041

Egerton, R.F., 1982. A revised expression for signal/noise ratio in EELS. Ultramicroscopy 9, 387–390. https://doi.org/10.1016/0304-3991(82)90101-2

Egerton, R.F., 1979. K-Shell ionization cross sections for use in microanalysis. Ultramicroscopy 4, 169–179.

Egerton, R.F., 1978. Formulae for light-element micro analysis by electron energy-loss spectrometry. Ultramicroscopy 3, 243–251. https://doi.org/10.1016/S0304-3991(78)80031-X

Egoavil R., Gauquelin N., Martinez G.T., Van Aert S., Van Tendeloo G., Verbeeck J., 2014. Atomic resolution mapping of phonon excitations in STEM-EELS experiments. Ultramicroscopy 147, 1-7. https://doi.org/10.1016/j.ultramic.2014.04.011

Eklund, P., Beckers, M., Jansson, U., Högberg, H., Hultman, L., 2010. The Mn + 1AXn phases: Materials science and thin-film processing. Thin Solid Films 518, 1851–1878. https://doi.org/10.1016/j.tsf.2009.07.184

Emmerlich, J., Högberg, H., Sasvári, S., Persson, P.O.Å., Hultman, L., Palmquist, J.P., Jansson, U., Molina-Aldareguia, J.M., Czigány, Z., 2004. Growth of Ti3SiC2 thin films by elemental target magnetron sputtering. J. Appl. Phys. 96, 4817–4826. https://doi.org/10.1063/1.1790571

Ettmayer, P., Kolaska, H., Ortner, H.M., 2014. History of Hardmetals, in: Sarin, V.K., Mari, D., LLanes, L., Nebel, C.E. (Eds.), Comprehensive Hard Materials. Elsevier, Oxford, pp. 3–27.

Exner, H.E., 1979. Physical and chemical nature of cemented carbides. Int. Met. Rev. 4, 149–173.

Fang, Z.Z., Koopman, M.C., Wang, H., 2014. Cemented Tungsten Carbide HardmetaldAn Introduction, in: Sarin, V.K., Mari, D., LLanes, L., Nebel, C.E. (Eds.), Comprehensive Hard Materials. Elsevier, Oxford, pp. 123–137.

Fladischer S., Grogger W., 2014. Quantitative EDXS analysis of organic materials using the ζ-factor method, Ultramicroscopy 136, 26-30, https://doi.org/10.1016/j.ultramic.2013.07.015.

Garrett-Reed, A., Bell, D.C., 2002. Energy Dispersive X-ray Analysis in the Electron Microscope. BIOS Scientific Publishers.

Gatan Electron Microscopy School-EELS Imaging and Analysis, 2013.

Gauvin, R., 2012. What Remains to Be Done to Allow Quantitative X-Ray Microanalysis Performed with EDS to Become a True Characterization Technique? Microsc. Microanal. 18, 915–940. https://doi.org/10.1017/S1431927612001468

Gmelins Handbuch der Anorganischen Chemie, 8. Auflage. ed, 1933. . Verlag Chemie,

Berlin.

Goldschmidt, H.J., Brand, J.A., 1963. The tungsten-rich region of the system tungsten–carbon. J Less-Common Met.5. (2). https://doi.org/10.1016/0022-5088(63)90012-2

Gorelik, T., Schlitt, S., Kolb, U., 2010. Introduction to ADT/ADT3D, in: Kolb, U., Shankland, K., Meshi, L., Avilov, A., David, W. (Eds.), Uniting Electron Crystallography and Powder Diffraction. Springer ScienceCBusiness Media, Dordrecht, pp. 337–347.

Grande, M., Ahn, C.C., 1983. Deconvolution and quantification of energy-loss transition metal oxide spectra., in: P., D. (Ed.), Inst. Phys. Conf. Ser. No. 68. pp. 123–126.

Gubbens, A., Barfels, M., Trevor, C., Twesten, R., Mooney, P., Thomas, P., Menon, N., Kraus, B., Mao, C., McGinn, B., 2010. The GIF Quantum, a next generation post-column imaging energy filter. Ultramicroscopy 110, 962–970. https://doi.org/10.1016/j.ultramic.2010.01.009

Guilemany, J.M., Sanchiz, I., Alcobé, X., 1992. X-Ray Diffraction Analysis of Titanium Carbonitride 30/70 and 70/30 Solid Solutions. Powder Diffr. 7, 34–35. https://doi.org/10.1017/S0885715600016043

Gusev, A.I., Rempel, A.A., Magerl, A.J., 2001. Disorder and order in strongly nonstoichiometric compounds. Springer, Berlin.

Haider, M., Braunshausen, G., Schwan, E., 1995. Correction of the spherical aberration of a 200 kV TEM by means of a hexapole-corrector. Optik (Stuttg). 99, 167–169.

Haider, M., Uhlemann, S., Zach, J., 2000. Upper limits for the residual aberrations of a high-resolution aberration-corrected STEM. Ultramicroscopy 81, 163–175. https://doi.org/10.1016/S0304-3991(99)00194-1

Hall, S.R., Allen, F.H., Brown, I.D., 1991. The crystallographic information file (CIF): a new standard archive file for crystallography. Acta Crystallogr. Sect. A Found. Crystallogr. 47, 655–685. https://doi.org/10.1107/S010876739101067X

Harkins, P., MacKenzie, M., Craven, A.J., McComb, D.W., 2008. Quantitative electron energy-loss spectroscopy (EELS) analyses of lead zirconate titanate. Micron 39, 709–716. https://doi.org/10.1016/j.micron.2007.10.016

Hébert, C., 2007. Practical aspects of running the WIEN2k code for electron spectroscopy. Micron 38, 12–28. https://doi.org/10.1016/j.micron.2006.03.010

Hellenbrandt, M., 2004. The Inorganic Crystal Structure Database (ICSD)—Present and Future. Crystallogr. Rev. 10, 17–22. https://doi.org/10.1080/08893110410001664882

Hillier, J., Baker, R.F., 1944. Microanalysis by Means of Electrons. J. Appl. Phys. 15, 663–675. https://doi.org/10.1063/1.1707491

Hofer, F; Kothleitner, G., 1993. Quantitative microanalysis using electron energy-loss spectroscopy. I. Li and Be in oxides. Microsc. Microanal. Microstruct.

Hofer, F., 1991. Determination of inner-shell cross sections for EELS-quantification. Microsc. Microanal. Microstruct. 2, 215–230. https://doi.org/10.1051/mmm:0199100202-3021500

Hofer, F., 1989. EELS quantification of the elements Ba to Tm by means of N45 edges. J. Microsc. 156, 279–283. https://doi.org/10.1111/j.1365-2818.1989.tb02929.x

Hofer, F., 1987. EELS quantification of M edges by using oxidic standards. Ultramicroscopy 21, 63–68. https://doi.org/10.1016/0304-3991(87)90007-6

Hofer, F, 1987. A method for preparation of thin corrosion layers of brass for TEM investigations. J. Mcroscopy.

Hofer, F., Golob, P., 1988. Quantification of electron energy-loss spectra with K and L shell ionization cross sections. Micron Microsc. Acta 19, 73–86. https://doi.org/10.1016/0739-6260(88)90002-0

Hofer, F., Golob, P., Brunegger, A., 1988. EELS quantification of the elements Sr to W by means of M45 edges. Ultramicroscopy 25, 81–84. https://doi.org/10.1016/0304-3991(88)90409-3

Hofer, F., Kothleitner, G., 1996. Quantitative Microanalysis Using Electron Energy-Loss Spectrometry: II. Compounds with Heavier Elements. Microsc. Microanal. Microstruct. 7, 265–277. https://doi.org/10.1051/mmm:1996121

Hofer, F., Warbichler, P., Scott, A., Brydson, R., Galesic, I., Kolbesen, B., 2001. Electron energy-loss near edge structure on the nitrogen K-edge in vanadium nitrides. J. Microsc. 204, 166–171. https://doi.org/10.1046/j.1365-2818.2001.00946.x

Holleck, H., 1986. Material selection for hard coatings. J. Vac. Sci. Technol. A Vacuum, Surfaces, Film. 4, 2661–2669. https://doi.org/10.1116/1.573700

Iakoubovskii, K., Mitsuishi, K., Nakayama, Y., Furuya, K., 2008. Thickness measurements with electron energy-loss spectroscopy. Microsc. Res. Tech. 71, 626–631. https://doi.org/10.1002/jemt.20597

Jeitschko, W., Nowotny, H., 1967. Die Kristallstruktur von Ti3SiC2-ein neuer Komplexcarbid-Typ. Monatshefte f?r Chemie - Chem. Mon. 98, 329–337. https://doi.org/10.1007/BF00899949

Jorissen, K., 2007. The ab initio calculation of relativistic electron energy-loss spectra.

PhD-Thesis, Universiteit Antwerpen.

Joy, D.C., Egerton, R.F., Maher, D.M., 1979. Progress in the quantification of electron energy-loss spectra, in: Johari, O. (Ed.), Scanning Electron Microscopy. SEM Inc., AMF O'Hare, Illinois, pp. 817–826.

Karlsson, L., Hultman, L., Johansson, M.P., Sundgren, J.-E., Ljungcrantz, H., 2000. Growth, microstructure, and mechanical properties of arc evaporated TiCxN1−x (0≤x≤1) films. Surf. Coatings Technol. 126, 1–14. https://doi.org/10.1016/S0257-8972(00)00518-1

Kelly, P.M., Jostsons, A., Blake, R.G., Napier, J.G., 1975. The determination of foil thickness by scanning transmission electron microscopy. Phys. Status Solidi 31, 771–780. https://doi.org/10.1002/pssa.2210310251

Kieffer, R., Schwarzkopf, P., Benesovsky, F., Leszynsky, W., 1953. Hartstoffe und Hartmetalle. Springer, Wien.

Kirkland, Earl, J., 2006. Image Simulation in Transmission Electron Microscopy. Ithaca.

Kirkland, Earl, J., 2010. Multislice Applications and Examples. In: Advanced Computing in Electron Microscopy. Springer, Boston, MA. https://doi.org/10.1007/978-1-4419-6533-2_7

Knoll, M., Ruska, E., 1932. Das Elektronenmikroskop. Zeitschrift für Phys. 78, 318–339. https://doi.org/doi.org/10.1007/BF01342199

Kohn, W., Sham, L.J., 1965. Self-Consistent Equations Including Exchange and Correlation Effects. Phys. Rev. 140, A1133–A1138. https://doi.org/10.1103/PhysRev.140.A1133

Kolb, U., Gorelik, T., 2006. Electron Crystallography on Polymorphs, in: Electron Crystallography. Springer-Verlag, Berlin/Heidelberg, pp. 409–420. https://doi.org/10.1007/1-4020-3920-4_25

Kolb, U., Gorelik, T., Kübel, C., Otten, M.T., Hubert, D., 2007. Towards automated diffraction tomography: Part I-Data acquisition. Ultramicroscopy 107, 507–513. https://doi.org/10.1016/j.ultramic.2006.10.007

Kolb, U., Gorelik, T., Mugnaioli, E., 2009. Automated diffraction tomography combined with electron precession: a new tool for ab initio nanostructure analysis. MRS Proc. 1184, 1184-GG01-05. https://doi.org/10.1557/PROC-1184-GG01-05

Kolb, U., Gorelik, T., Otten, M.T., 2008. Towards automated diffraction tomography. Part II-Cell parameter determination. Ultramicroscopy 108, 763–772. https://doi.org/10.1016/j.ultramic.2007.12.002

Kolb, U., Matveeva, G.N., 2003. Electron crystallography on polymorphic organics. Zeitschrift für Krist. - Cryst. Mater. 218. https://doi.org/10.1524/zkri.218.4.259.20741

Kothleitner, G., Grogger, W., Dienstleder, M., Hofer, F., 2014. Linking TEM Analytical Spectroscopies for an Assumptionless Compositional Analysis. Microsc. Microanal. 20, 678–86. https://doi.org/10.1017/S1431927614000130

Kothleitner, G., Hofer, F., 1998. Optimization of the Signal to Noise Ratio in EFTEM Elemental Maps with Regard to Different Ionization Edge Types. Micron 29, 349–357. https://doi.org/10.1016/S0968-4328(98)00014-6

Kramers, H.A., 1923. XCIII. On the theory of X-ray absorption and of the continuous X-ray spectrum. London, Edinburgh, Dublin Philos. Mag. J. Sci. 46, 836–871. https://doi.org/10.1080/14786442308565244

Kraxner, J., 2018. Analytical TEM of organic electronics with a special focus on EDXS and geometry aspects. PhD-Thesis, TU Graz.

Kraxner, J., Schäfer, M., Röschel, O., Kothleitner, G., Haberfehlner, G., Paller, M., Grogger, W., 2017. Quantitative EDXS: Influence of geometry on a four detector system. Ultramicroscopy 172, 30–39. https://doi.org/10.1016/j.ultramic.2016.10.005

Krivanek, O.L., Dellby, N., Spence, A.J., Camps, R.A., Brown, L.M., 1997. Aberration correction in the STEM, in: Rodenburg, J.M. (Ed.), Institute of Physics Conference Series. IOP Publishing Ltd, pp. 35–40.

Krivanek, O.L., Dellby, N., Lovejoy, T.C., Bacon, N.J., Corbin, G.J., Hrncirik, P., Szilagyi, Z.S., Aoki, T., Carpenter, R.W., Crozier, P.A., Zhu, J., Rez, P., Egerton, R.F., Batson, P.E., 2014. Exploring Phonon Signals by High Energy / High Spatial Resolution EELS. Microsc. Microanal. 20, 66–67. https://doi.org/10.1017/S1431927614002050

Krivanek, O.L., Dellby, N., Lupini, A.R., 1999. Towards sub-Å electron beams. Ultramicroscopy 78, 1–11. https://doi.org/10.1016/S0304-3991(99)00013-3

Krivanek, O.L., Lovejoy, T.C., Dellby, N., Carpenter, R.W., 2013. Monochromated STEM with a 30 meV-wide, atom-sized electron probe. Microscopy 62, 3–21. https://doi.org/10.1093/jmicro/dfs089

Krivanek, O.L., Nellist, P.D., Dellby, N., Murfitt, M.F., Szilagyi, Z., 2003. Towards sub-0.5Å electron beams. Ultramicroscopy 96, 229–237. https://doi.org/10.1016/S0304-3991(03)00090-1

Kuimalee, S., Chairuangsri, T., Pearce, J.T.H., Edmonds, D. V., Brown, A.P., Brydson, R.M.D., 2010. Quantitative analysis of a complex metal carbide formed during furnace cooling of cast duplex stainless steel using EELS and EDS in the TEM. Micron 41, 423–429. https://doi.org/10.1016/j.micron.2010.02.009

Kurlov, A.S., Gusev, A.I., 2013. Tungsten Carbides. Springer.

Kurlov, A.S., Gusev, A.I., 2006. Tungsten carbides and W-C phase diagram. Inorg. Mater. 42, 121–127. https://doi.org/10.1134/S0020168506020051

Lassner, E., Schubert, W.-D., 1999. Tungsten, Tungsten. Properties, Chemistry, Technology of the Element, Alloys, and Chemical Compounds. Springer US, Boston, MA. https://doi.org/10.1007/978-1-4615-4907-9

Lassner, E., Schubert, W.-D., Lüderitz, E., Wolf, H., 2005. Tungsten, Tungsten Alloys, and Tungsten Compounds, in: Ullmann's Encyclopedia of Industrial Chemistry. pp. 229–265.

Leapman, R., Rez, P., Mayers, D., 1980. K, L, and M shell generalized oscillator strengths and ionization cross sections for fast electron collisions. J. Chem. Phys. 72, 1232. https://doi.org/10.1063/1.439184

Lengauer, W., 2000. Transition Metal Carbides, Nitrides, and Carbonitrides, in: Riedl, R. (Ed.), Handbook of Ceramic Hard Materials. Wiley, Weinheim.

LePoole, J., B., 1947. Ein neues Elektronenmikroskop mit stetig regelbarer Vergrößerung. Philips Techn Rundschau 9.

Levi, G., Kaplan, W.D., Bamberger, M., 1998. Structure refinement of titanium carbonitride (TiCN). Mater. Lett. 35, 344–350. https://doi.org/10.1016/S0167-577X(97)00276-0

Lopatin, S., Cheng, B., Liu, W.-T., Tsai, M.-L., He, J.-H., Chuvilin, A., 2018. Optimization of monochromated TEM for ultimate resolution imaging and ultrahigh resolution electron energy-loss spectroscopy. Ultramicroscopy 184, 109–115. https://doi.org/10.1016/j.ultramic.2017.08.016

Malis, T., Cheng, S.C., Egerton, R.F., 1988. EELS Log-Ratio Technique for Specimen-Thickness Measurement in the TEM. J. Electron Microsc. Tech. 8, 193–200.

Malis, T.F., Titchmarsh, J.M., 1985. K-factor approach to EELS, in: Tatlock, G.J. (Ed.), Inst. Phys. Conf. Ser. No 78. pp. 181–184.

Manoubi, T., Colliex, C., Rez, P., 1990. Quantitative electron energy-loss spectroscopy on M45 edges in rare earth oxides. J. Electron Spectros. Relat. Phenomena 50, 1–18. https://doi.org/10.1016/0368-2048(90)80001-Q

Manoubi, Tahar, Tencé, M., Walls, M.G., Colliex, C., 1990. Curve fitting methods for quantitative analysis in electron energy-loss spectroscopy. Microsc. Microanal. Microstruct. 1, 23–39. https://doi.org/10.1051/mmm:019900010102300

Moreno, M.S., Jorissen, K., Rehr, J.J., 2007. Practical aspects of electron energy-loss spectroscopy (EELS) calculations using FEFF8. Micron 38, 1–11. https://doi.org/10.1016/j.micron.2006.03.011

Morniroli, J.P., 2002. Large-angle convergent-beam electron diffraction applications to crystal defects. Société Française des Microscopies.

Mugnaioli, E., Gorelik, T., 2012. ADT-3D User manual. Karlsruhe.

Nesvizhskii, A.I., Rehr, J.J., 1999. L -edge XANES of 3 d -transition metals. J. Synchrotron Radiat. 6, 315–316. https://doi.org/10.1107/S0909049599001697

Nowotny, H., 1971. Strukturchemie einiger Verbindungen der Übergangsmetalle mit den elementen C, Si, Ge, Sn. Prog. Solid State Chem. 5, 27–70. https://doi.org/https://doi.org/10.1016/0079-6786(71)90016-1

Own, C.S., Subramanian, A.K., Marks, L.D., 2004. Quantitative Analyses of Precession Diffraction Data for a Large Cell Oxide. Microsc. Microanal. 10, 96–104. https://doi.org/10.1017/S1431927604040322

Pennycook, S.J., 2017. The impact of STEM aberration correction on materials science. Ultramicroscopy 180, 22–33. https://doi.org/10.1016/j.ultramic.2017.03.020

Philibert, J., 1963. A method for calculating the absorption correction in electron-probe microanalysis, Proceedings of the 3rd International Congress on X-Ray Optics and Microanalysis. Academic Press, New York.

Pitfield, P., Brown, T., Gunn, G., Rayner, D., 2011. Tungsten Commodity Profile. Nottingham.

Prakash, L., 2014. Fundamentals and General Applications of Hardmetals, in: Sarin, V.K., Mari, D., LLanes, L., Nebel, C.E. (Eds.), Comprehensive Hard Materials. Elsevier, Oxford, pp. 29–90.

Pun, T., Ellis, J.R., Eden, M., 1985. Weighted least squares estimation of background in EELS imaging. J. Microsc. 137, 93–100. https://doi.org/10.1111/j.1365-2818.1985.tb02565.x

Randhawa, H., 1987. Cathodic arc plasma deposition of TiC and TiCxN1−x films. Thin Solid Films 153, 209–218. https://doi.org/10.1016/0040-6090(87)90183-0

Ravel, B., 2001. ATOMS: crystallography for the X-ray absorption spectroscopist. J. Synchrotron Rad. 8, 314–316.

Rehr, J.J., Kas, J.J., Vila, F.D., Prange, M.P., Jorissen, K., 2010. Parameter-free calculations of X-ray spectra with FEFF9. Phys. Chem. Chem. Phys. 12, 5503. https://doi.org/10.1039/b926434e

Reimer, L., 1984. Transmission Electron Microscopy. Springer-Verlag, Berlin, Heidelberg.

Rempel, A.A., 1996. Atomic and vacancy ordering in nonstoichiometric carbides. Physics-Uspekhi 39, 31–56. https://doi.org/10.1070/PU1996v039n01ABEH000126

Rez, P., 1982. Cross sections for energy-loss spectrometry. Ultramicroscopy 9, 283–287. https://doi.org/10.1016/0304-3991(82)90213-3

Rose, H.H., 2009. Historical aspects of aberration correction. J. Electron Microsc. (Tokyo). 58, 77–85. https://doi.org/10.1093/jmicro/dfp012

Ruthemann, G., 1941. Diskrete Energieverluste schneller Elektronen in Festkörperntle. Naturwissenschaften 29, 648.

Sarikaya, M., Qian, M., Stern, E.A., 1996. EXELFS revisited. Micron 27, 449–466. https://doi.org/10.1016/S0968-4328(96)00044-3

Schedler, W., 1988. Hartmetall für den Praktiker. VDI-Verlag, Düsseldorf.

Scheinfein, M., Isaacson, M., 1984. Design and performance of second order aberration corrected spectrometers for use with the scannering transmission electron microscope., in: Johari, O. (Ed.), Scanning Electron Microscopy. SEM Inc., A. M. F. O'Hare, Illinois, pp. 1681–1696.

Scherzer, O., 1949. The Theoretical Resolution Limit of the Electron Microscope. J. Appl. Phys. 20, 20–29. https://doi.org/10.1063/1.1698233

Schleinkofer, U., Czettl, C., Claude, M., 2014. Coating Applications for Cutting Tools, in: Sarin, V.K., Mari, D., LLanes, L., Nebel, C.E. (Eds.), Comprehensive Hard Metals. Elsevier, Oxford, pp. 453–469.

Seifert, T., 2008. Metallogeny and Petrogenesis of Lamprophyres in the Mid-European Variscides. IOS Press BV, Amsterdam.

Sherman, D., Brandon, D., 2000. Mechanical Properties and their Relation to Microstructure, in: Riedel, R. (Ed.), Handbook of Ceramic Hard Materials. Wiley, Weinheim.

Slater, J.C., 1930. Atomic shielding constants. Phys. Rev. 36, 57–64. https://doi.org/10.1103/PhysRev.36.57

Stadelmann, P. A. , 2004. JEMS - EMS java version, https://www.jems-swiss.ch/

Sun, Z.M., 2011. Progress in research and development on MAX phases: a family of

layered ternary compounds. Int. Mater. Rev. 56, 143–166. https://doi.org/10.1179/1743280410Y.0000000001

Thomas, P.J., Twesten, R.D., 2012. A Simple, Model Based Approach for Robust Quantification of EELS Spectra and Spectrum-Images. Microsc. Microanal. 18, 968–969. https://doi.org/10.1017/S1431927612006691

Tiemeijer, P., 1999. Operation modes of a TEM monochromator, in: Inst. Phys. Conf. Ser. No 161: Section 5. IOP Publishing Ltd, EMAG99, Sheffield.

Verbeeck, J., 2002. Electron energy-loss spectroscopy of nanoscalematerials. PhD-Thesis, Universiteit Antwerpen.

Verbeeck, J., Van Aert, S., 2004. Model based quantification of EELS spectra. Ultramicroscopy 101, 207–224. https://doi.org/10.1016/j.ultramic.2004.06.004

Verbeeck, J., Van Aert, S., Bertoni, G., 2006. Model-based quantification of EELS spectra: Including the fine structure. Ultramicroscopy\rProceedings Int. Work. Enhanc. Data Gener. by Electrons 106, 976–980. https://doi.org/10.1016/j.ultramic.2006.05.006

Vincent, R., Midgley, P.A., 1994. Double conical beam-rocking system for measurement of integrated electron diffraction intensities. Ultramicroscopy 53, 271–282. https://doi.org/10.1016/0304-3991(94)90039-6

von Ardenne, M., 1938. Das Elektronen-Rastermikroskop. Zeitschrift für Phys. 109, 553–572.

Wang D., 2006. Characterisation of Catalysts by Transmission Electron Microscopy. In: Weirich T.E., Lábár J.L., Zou X. (eds) Electron Crystallography. NATO Science Series II: Mathematics, Physics and Chemistry, vol 211. Springer, Dordrecht. https://doi.org/10.1007/1-4020-3920-4_30

Watanabe, M., Williams, D.B., 2006. The quantitative analysis of thin specimens: A review of progress from the Cliff-Lorimer to the new ζ-factor methods. J. Microsc. 221, 89–109. https://doi.org/10.1111/j.1365-2818.2006.01549.x

Williams, B., 2012. Powder metallurgy: A global market review. Int. Powder Metall. (15th ed.) UK innovar Commun. Ltd.

Williams, D.B., Carter, C.B., 2009. Transmission Electron Microscopy: A Textbook for Materials Science. Springer US, New York.

Zaluzec, N.J., 1989. Processing and quantification of X-ray Energy-Dispersive Spectra in the Analytical Electron Microscope. Ultramicroscopy 28, 226-235. https://doi.org/10.1016/0304-3991(89)90300-8

Zener, C., 1930. Analytic atomic wave functions. Phys. Rev. 36.

Zhang, S., 1993. Titanium carbonitride-based cermets: processes and properties. Mater. Sci. Eng. A 163, 141–148. https://doi.org/10.1016/0921-5093(93)90588-6

Zulliger, H. R., Aitken, D. W., 1970. Fano Factor Fact and Fallacy. In IEEE Transactions on Nuclear Science, vol. 17, no. 3, 187-195. doi: 10.1109/TNS.1970.4325691